SEAWATER CARBON DIOXIDE DYNAMICS IN STRATIFIED SHALLOW COASTAL WATERS: FIELD MEASUREMENT AND NUMERICAL MODELING IN THE YATSUSHIRO SEA, JAPAN

熊, 柄

SEAWATER CARBON DIOXIDE DYNAMICS IN STRATIFIED SHALLOW COASTAL WATERS: FIELD MEASUREMENT AND NUMERICAL MODELING IN THE YATSUSHIRO SEA, JAPAN

Bing Xiong

Abstract

In recent decades, climate change has affected natural and human systems on all continents and oceans. The global climate change observed since the beginning of the 20th century has been mainly driven by human activities, especially the burning of fossil fuels, which increase the greenhouse gases in the Earth's atmosphere. Carbon dioxide (CO_2) emissions, which account for more than 70% of greenhouse gas emissions, are considered one of the most important contributors to global warming and climate change. From the Mauna Loa Observatory in Hawaii, atmospheric CO_2 concentrations have jumped from 315 ppm in 1958 to 411 ppm in 2019 over the past 60 years. Therefore, controlling the increase of CO_2 in the atmosphere has become an urgent issue that the world needs to face together.

The ocean, which stores and sequesters large amounts of CO_2 in the form of dissolved inorganic carbon (DIC), can buffer the increase in atmospheric CO_2 concentration. A lot of studies have indicated that the global ocean hosts a substantial reservoir of CO_2 that is 50 times greater than that in the atmosphere and is considered an extremely significant net sink of atmospheric CO_2.

Meanwhile, several studies have demonstrated that shallow coastal waters with vegetation such as seagrass, mangroves, and salt marshes contribute more than half of the total oceanic carbon storage despite making up only 0.5% of the ocean area, owing to them having the highest carbon burial rates in the ocean. Therefore, the shallow coastal waters are also considered to be potentially the most efficient carbon sink on the Earth. In order to assess the contribution of these waters to the reduction of atmospheric CO_2, CO_2 fluxes (F_{CO2}) are being estimated globally in various regions. However, due to the complexity of the biogeochemical processes in these waters, the distribution and dynamics of CO_2 in seawater have uncertainty.

Stratification, which often occurs in shallow coastal waters, is considered to be one of the important factors affecting the biochemical dynamics in seawater. In order to better understand the carbon cycle in shallow coastal waters and improve the accuracy of F_{CO2} estimation, it is necessary to grasp and analyze the carbon dioxide dynamics in seawater by considering the effects of stratification.

In this research, we selected the Yatsushiro Sea as the target area, which is highly enclosed and susceptible to stratification in summer. Through a combination of field measurements and 3D numerical simulations, we aim to address the following scientific questions: Does stratification affect seawater CO_2 dynamics of the Yatsushiro Sea, and how does it do so? What are the other influencing factors? What are the characteristics of CO_2 distribution in the bay throughout the year, and what are the factors that affect it? Is the bay a source or sink of atmospheric CO_2 throughout the year? How strong is its intensity?

For answering these questions, the study was divided in some chapter in this thesis, and described as follows:

Chapter 1 explains about research background, research status and issues, research objectives, and also the overview of the thesis as an introduction.

Chapter 2 shows several previous researches related to our study. Also, a definition of blue carbon in shallow coastal waters is indicated. Methods and shortcomings of the current stage of calculating seawater F_{CO2}, the main factors influencing the seawater partial pressure CO_2 (pCO_2) and potential relationship between stratification and seawater pCO_2 in shallow coastal waters are described.

Chapter 3 indicates pCO_2 in the Yatsushiro Sea under density stratification conditions from three field measurements. Moreover, by calculating two indicators of biological processes (ΔDIC and ΔTA (total alkalinity)), we revealed the possibility that the CO_2 dynamics at the measurement points are simultaneously influenced by biological processes and other hydrodynamic effects.

Chapter 4 evaluates the effects of seawater inflow from the Ariake Sea and the amount of freshwater inflow from rivers other than the Kuma River through simulations with 3D numerical hydrodynamic and particle tracking models. The

results show that the inflow impacts of both components are small enough to be negligible. This result supports our focus on studying the influence of biological processes on seawater CO_2 dynamics only in the Yatsushiro Sea.

In Chapter 5, a 3D numerical hydrodynamic-ecological coupled model of the CO_2 dynamics in the Yatsushiro Sea based on the results of field measurement was developed. The developed model reproduced well the distribution of pCO_2, salinity, density, and temperature under different stratification conditions. Furthermore, we confirmed that the CO_2 sequestration around the estuary fluctuates greatly in space and time with the flooding event from the hindcast calculation through the numerical model.

In Chapter 6, we further improved the performance of the numerical model to simulate the CO_2 dynamics over the full range of the Yatsushiro Sea. From the simulation results, we can see that stratification has even opposite effects on surface pCO_2, depending on the duration and intensity of the freshwater inflow impact. Moreover, we used the model to estimate the annual pattern of CO_2 flux in the bay in 2018. The results show that the Yatsushiro Sea becomes a source of atmospheric CO_2 in June and July when the freshwater inflow is high and a sink of atmospheric CO_2 at all other times.

Chapter 7 concludes all chapters in this thesis and also proposes some recommendation for future works.

Acknowledgment

First and foremost, I would like to express my deepest sincere gratitude to my supervisor, Prof. Shinichiro Yano of Department of Urban and Environmental Engineering, Kyushu University, for giving me the opportunity to do this research and helping me during my study in Kyushu University. His enthusiasm, foresight, sincerity and motivation have deeply inspired me. He taught me the methodology to carry out the field measurement and provided critical advice in my calculations and suggested many important additions and improvements. It was a great privilege and honor to work and study under his guidance.

In addition to my supervisor, I would like to express my sincere gratitude for the rest committee members, Prof. Takahiro Kuba and Prof. Masaru Yamashiro of Kyushu University, for their insightful comments and encouragement, as well as for the difficult questions that prompted me to expand my research to include a variety of perspectives. Also, I express my gratitude to Associate Prof. Akira Tai and Assistant Prof. Yasuyuki Maruya for their valuable advice and vital support in measurement and software during my research in Kyushu University.

I gratefully acknowledge the kindly support and constructive suggestions of Prof. Keisuke Nakayama of Kobe University, Prof. Hiroshi Yajima of Shimane University and Prof. Katsuaki Komai of Kitami Institute of Technology as collaborating researchers. Their profound research insights as well as their vast knowledge base have been crucial to the advancement of my research. Thanks also to Prof. Akihide Tada of Nagasaki University and Minamata Fishermen's Cooperative Association for providing vessels and assistance for the field measurements.

I would like to say thanks and appreciate greatly my financial support from the program “Support for Pioneering Research Initiated by the Next Generation

(SPRING),” of the Japan Science and Technology Agency (JST) and Grants-in-Aid for Scientific Research (KAKENHI) of the Japan Society for the Promotion of Science (JSPS) (JP18H01545) for sponsoring my doctoral research in Kyushu University. Thank you so much for your generosity and overwhelming support. It is an enormous pleasure to be one of your recipients.

My sincere gratitude to all members of Kyushu University's Environmental Fluid Dynamic Laboratory, Department of Civil Engineering, for assisting me in doing the research, and with whom I have shared a very memorable and interesting life at Kyushu University. I would especially like to thank “Blue Carbon” team members, Mr. Saito and Mr. Komori. It was because of your help that my life and study at Kyushu University were so full of fun. I firmly believe that our friendship just started at Kyushu University and will never end.

Last but not least, I would like to give my great appreciation to my family members, my parents, my grandparents, for their understanding, trust and support. Your endless love for me was what sustained me this far. I wish you all the best, and health and happiness will always be with you.

Bing Xiong

Fukuoka, January 2022

Contents

List of Figures

List of Tables

Chapter 1
Introduction

1.1 Research Background

Global warming is considered a great challenge to all humanity, leading to global redistribution of precipitation, melting glaciers and permafrost, rising sea levels, etc. It damages the balance of natural ecosystems, affects human health, and even threatens the survival of human beings. It is estimated that anthropogenic warming has reached about 1 °C since the pre-industrial period, increasing 0.2 °C per decade (Jarraud & Steiner, 2012).

Climate change has affected natural and human systems on all continents and oceans in recent decades. The global climate change observed since the beginning of the 20th century is mainly driven by human activities, especially the burning of fossil fuels, which increases greenhouse gases in the Earth's atmosphere. Carbon dioxide (CO_2) emissions, which account for more than 70% of greenhouse gas emissions, are considered one of the most important contributors to global warming and climate change. From the Mauna Loa Observatory in Hawaii (shown in Fig.1.1), the concentration of CO_2 in the atmosphere has jumped from 315 ppm in 1958 to 411 ppm in 2019 over the past 60 years. Therefore, controlling the increase of CO_2 in the atmosphere has become an urgent issue that the world needs to face together.

The conceptual diagram of the global CO_2 cycle is shown in Fig.1.2, where we can see that the CO_2 budget of terrestrial organisms is almost balanced through their respiration and photosynthesis. At the same time, the oceans, which cover 71% of the Earth's surface area, are an essential sink for anthropogenic CO_2 emissions (McLeod et al., 2011). The global oceans' net uptake of atmospheric CO_2 has been about 1.5-2.0 GtC yr^{-1} over the last few decades (Takahashi et al., 2009). Carbon in the oceans exists in inorganic carbon (IC) and organic carbon (OC). Among them, the carbon involved in the solubility pump, which is based on the dynamic equilibrium of the seawater carbonate system, exists in four chemical forms, HCO_3^-, CO_3^{2-}, CO_2, and H_2CO_3, called Dissolved Inorganic Carbon (DIC), and its content in the ocean is estimated to be more than 38,000 PgC (S. W. Nixon, 1995; Rabalais et al., 2009),

which is close to 98% of the global ocean carbon stock.

The ocean converts DIC in seawater into OC through physical dissolution, buffering by the seawater carbonate system, and photosynthesis by marine organisms oceanic thermohaline circulation and particulate sinking, thereby transporting carbon from the surface to the deep ocean and finally buried in the sediment.

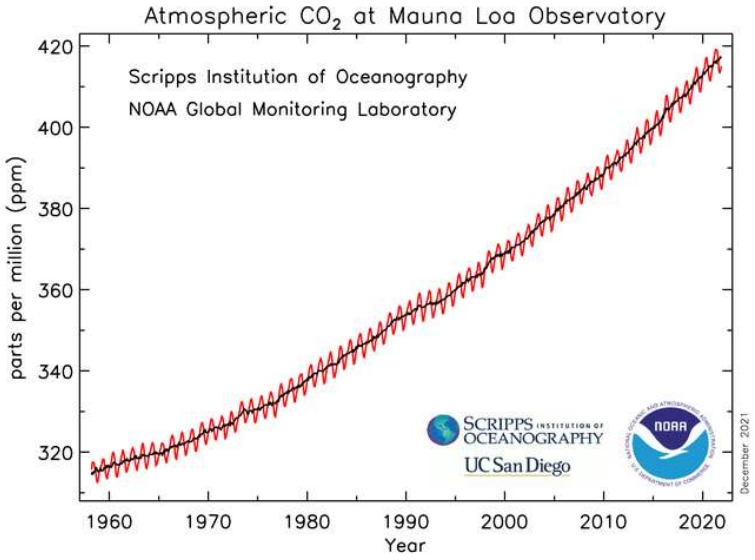

Figure 1.1 The monthly average atmospheric CO_2 concentration of 1958 to 2019, observed at Mauna Loa Observatory, Hawaii. (https://gml.noaa.gov/ccgg/trends/)

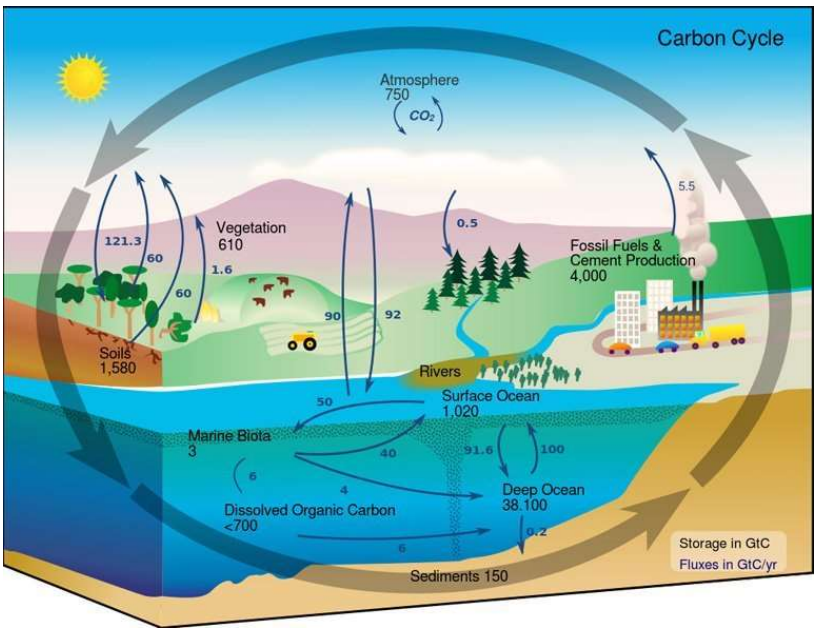

Figure 1.2 The concept diagram of the global CO_2 cycle (source: NASA Earth Observatory).

Meanwhile, shallow coastal waters comprised of estuaries, shallows, intertidal flats have recently attracted extensive scientific attention due to their valuable potential role in climate change mitigation and adaptation. Several studies demonstrated that shallow coastal waters with vegetation such as seagrass, mangroves, salt marshes contribute more than 50% of the total oceanic carbon storage, within only 0.5% coverage of the ocean area, owing to their highest carbon burial rates in the ocean (average: 138-226 gC m^{-2} yr^{-1}), about 3 to 4 orders of magnitude higher than in open ocean sediments (0.018 gC m^{-2} yr^{-1}), and carbon sequestrated and stored by these habitats is called "blue carbon" (Alongi et al., 2016; Chen et al., 2013; Donato et al., 2011; Duarte et al., 2005; Fourqurean et al., 2012; Kuwae et al., 2016; Murdiyarso et al., 2015).

Recent studies related to the role of shallow coastal waters in climate change mitigation and adaptation are beginning to estimate the amount of atmospheric CO_2 uptake through air-water CO_2 gas exchange (Bauer et al., 2013; Chen et al., 2013; Gustafsson et al., 2015; Maher & Eyre, 2012; Tokoro et al., 2014). However, different from terrestrial ecosystems, submerged carbon burial is not directly linked to removing atmospheric CO_2 due to the water column, which separates the atmosphere from benthic systems within complex carbon dynamics. Thus, although shallow coastal waters are considered a significant carbon reservoir, they could also become net emitters of atmospheric CO_2 through air-water CO_2 gas exchange (Bauer et al., 2013; Chen et al., 2013; Regnier et al., 2013). Since the level of the CO_2 partial pressure (pCO_2) in the atmosphere fluctuates slightly, air-water interface CO_2 flux is basically determined by the pCO_2 in surface water (Wanninkhof, 1992). However, the pCO_2 in surface water fluctuates significantly on a short-time scale due to the complex distribution and dynamics of DIC in the water column. In addition, some studies reported that pCO_2 in seawater would probably fluctuate with the development of stratification due to riverine freshwater inflow (Koné et al., 2009). Due to the complexity of CO_2 dynamics in the water column of shallow coastal waters, it is difficult to estimate the CO_2 flux of shallow coastal waters accurately. Therefore, profoundly studying CO_2 dynamics in shallow coastal waters is critical to the accuracy of the estimation of atmospheric CO_2 absorption of shallow coastal waters. It has become a hot spot and front problem that needs to be mainly solved in blue carbon research. In addition, it is of vital significance for the diagnosis of the

carbon cycle model in seawater and the analysis of marine biochemical processes.

Field measurements are often considered one of the most effective methods to determine the biogeochemical distribution and dynamics in seawater. Recent studies have conducted several field measurements to determine the dynamics of CO_2 in shallow coastal waters to estimate its contribution to atmospheric CO_2 removal (Chen et al., 2013; Koné et al., 2009; Kubo et al., 2017).

However, these field measurements have basically been conducted in surface seawater on a monthly or annual scale, but the complex vertical distribution and dynamics of CO_2 resulting from short-term temporal events (e.g., stratification) in the water column are still poorly understood. Therefore, field measurements under several different stratification conditions are needed to clarify the vertical distribution and dynamics of CO_2 in shallow coastal waters. Furthermore, 3-dimension (3D) numerical simulation is an effective measure that complements field measurements data and enables further analysis. Sohma et al., (2018) confirmed the application of a 3D numerical model on the reproducibility of CO_2 dynamics in the water column of shallow coastal waters, but the model they developed was based on measurement data from surface seawater (Kubo et al., 2017), and the effects of stratification were not considered. Therefore, a 3D numerical model that can accurately describe the CO_2 dynamics under stratification can effectively further understand the carbon cycle in shallow coastal waters and improve the accuracy of CO_2 flux estimation.

1.2 Research Status and Issues

Recent studies related to the role of shallow coastal waters in climate change mitigation and adaptation are beginning to estimate the amount of atmospheric CO_2 uptake through air-water CO_2 gas exchange (Bauer et al., 2013; Kubo et al., 2017). However, the relationship between air-water CO_2 gas exchange and carbon storage is not clarified because submerged carbon burial is not directly linked to removing atmospheric CO_2 due to the water column, which separates the atmosphere from benthic systems within complex carbon dynamics.

Field measurements were conducted worldwide to determine the CO_2 dynamics in the water column of shallow coastal waters for estimating their contribution to atmospheric CO_2 removal. However, these field measurements were basically conducted in surface seawater within a monthly or annual scale, but the complicated vertical dynamics of CO_2 caused by short-term temporal events (e.g., stratification) in the water column which could be mainly considered affect the entire carbon absorption and storage cycle, are still unknown.

3D numerical simulation is an effective measure that complements field measurements data and enables further analysis. Sohma et al. confirmed the application of a 3D numerical model on the reproducibility of blue carbon dynamics in the water column of shallow coastal waters, but due to the model they developed was based on measurement data from surface seawater and the effects of stratification were not considered in their model (Kubo et al., 2017; Sohma et al., 2018).

1.3 Research Objectives and Overview

The main purpose of this research is to develop a 3D hydrodynamics-ecological coupled numerical model that can well reproduce the full suite of CO_2 dynamics in shallow coastal waters, considering the effect of stratification. Also, the second purpose is to apply this model to clarify the effects of several factors (i.e., stratification, transport, and biological processes) that potentially affect the CO_2 flux in shallow coastal waters. The detailed purposes of this research are presented in the following points:

1. To conduct field measurements of CO_2 dynamics in seawater under different stratification states in the Yatsushiro Sea, which has no previous measurement examples, to understand in detail the effect of stratification conditions on CO_2 dynamics of shallow coastal waters.

2. To develop a 3D numerical hydrodynamic and particle tracking model to evaluate the hydrodynamic effects that may affect the CO_2 dynamics in the Yatsushiro Sea.

3. To develop a 3D numerical hydrodynamic-ecological coupled model to obtain basic knowledge on CO_2 dynamics in shallow coastal waters. Moreover, to use the developed model to characterize the Spatio-temporal variability of CO_2 dynamics after flooding in the north Yatsushiro Sea.

4. To improve the hydrodynamic-ecological coupled model to simulate CO_2 dynamics of the whole Yatsushiro Sea. Furthermore, to analyze the CO_2 dynamics and the corresponding influence mechanism of the bay and estimate 2018's CO_2 flux through the numerical simulation results.

This thesis comprises seven chapters. The structure of the thesis is shown in Fig.1.3.

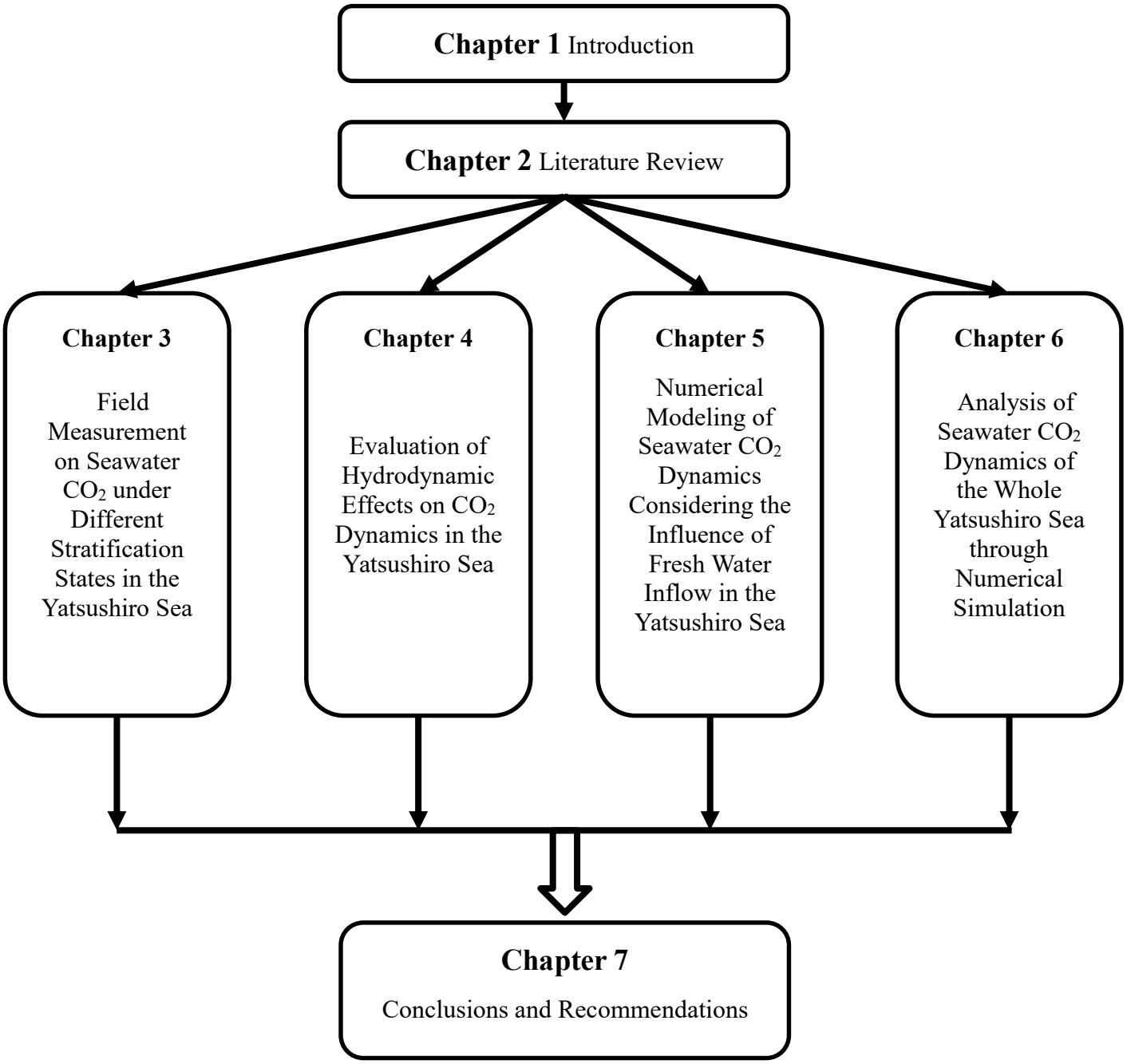

Figure 1.3 Thesis organization.

References

Alongi, D. M., Murdiyarso, D., Fourqurean, J. W., Kauffman, J. B., Hutahaean, A., Crooks, S., Lovelock, C. E., Howard, J., Herr, D., Fortes, M., Pidgeon, E., & Wagey, T. (2016). Indonesia's blue carbon: a globally significant and vulnerable sink for seagrass and mangrove carbon. *Wetlands Ecology and Management*, *24*(1), 3–13. https://doi.org/10.1007/s11273-015-9446-y

Bauer, J. E., Cai, W. J., Raymond, P. A., Bianchi, T. S., Hopkinson, C. S., & Regnier, P. A. G. (2013). The changing carbon cycle of the coastal ocean. *Nature*, *504*(7478), 61–70. https://doi.org/10.1038/nature12857

Chen, C. T. A., Huang, T.-H., Chen, Y. C., Bai, Y., He, X., & Kang, Y. (2013). Air–sea exchanges of CO2 in the world's coastal seas. *Biogeosciences*, *10*(10), 6509–6544. https://doi.org/10.5194/bg-10-6509-2013

Donato, D. C., Kauffman, J. B., Murdiyarso, D., Kurnianto, S., Stidham, M., & Kanninen, M. (2011). Mangroves among the most carbon-rich forests in the tropics. *Nature Geoscience*, *4*(5), 293–297. https://doi.org/10.1038/ngeo1123

Duarte, C. M., Middelburg, J. J., & Caraco, N. (2005). Major role of marine vegetation on the oceanic carbon cycle. *Biogeosciences*, *2*(1), 1–8. https://doi.org/10.5194/bg-2-1-2005

Fourqurean, J. W., Duarte, C. M., Kennedy, H., Marbà, N., Holmer, M., Mateo, M. A., Apostolaki, E. T., Kendrick, G. A., Krause-Jensen, D., McGlathery, K. J., & Serrano, O. (2012). Seagrass ecosystems as a globally significant carbon stock. *Nature Geoscience*, *5*(7), 505–509. https://doi.org/10.1038/ngeo1477

Gustafsson, E., Omstedt, A., & Gustafsson, B. G. (2015). The air-water CO2 exchange of a coastal sea—A sensitivity study on factors that influence the absorption and outgassing of CO2 in the B altic S ea. *Journal of Geophysical Research: Oceans*, *120*(8), 5342–5357.

Jarraud, M., & Steiner, A. (2012). Summary for policymakers. In *Managing the Risks of Extreme Events and Disasters to Advance Climate Change Adaptation: Special Report of the Intergovernmental Panel on Climate Change* (Vol. 9781107025). https://doi.org/10.1017/CBO9781139177245.003

Koné, Y. J. M., Abril, G., Kouadio, K. N., Delille, B., & Borges, A. V. (2009). Seasonal Variability of Carbon Dioxide in the Rivers and Lagoons of Ivory Coast (West Africa). *Estuaries and Coasts*, *32*(2), 246–260. https://doi.org/10.1007/s12237-008-9121-0

Kubo, A., Maeda, Y., & Kanda, J. (2017). A significant net sink for CO2 in Tokyo Bay. *Scientific Reports*, *7*(1), 44355. https://doi.org/10.1038/srep44355

Kuwae, T., Kanda, J., Kubo, A., Nakajima, F., Ogawa, H., Sohma, A., & Suzumura, M. (2016). Blue carbon in human-dominated estuarine and shallow coastal systems. *Ambio*, *45*(3), 290–301. https://doi.org/10.1007/s13280-015-0725-x

Maher, D. T., & Eyre, B. D. (2012). Carbon budgets for three autotrophic Australian estuaries: Implications for global estimates of the coastal air–water CO2 flux. *Global Biogeochemical Cycles*, *26*(1). https://doi.org/10.1029/2011GB004075

McLeod, E., Chmura, G. L., Bouillon, S., Salm, R., Björk, M., Duarte, C. M., Lovelock, C. E., Schlesinger, W. H., & Silliman, B. R. (2011). A blueprint for blue carbon: Toward an improved understanding of the role of vegetated coastal habitats in sequestering CO2. *Frontiers in Ecology and the Environment*, *9*(10), 552–560. https://doi.org/10.1890/110004

Murdiyarso, D., Purbopuspito, J., Kauffman, J. B., Warren, M. W., Sasmito, S. D., Donato, D. C., Manuri, S., Krisnawati, H., Taberima, S., & Kurnianto, S. (2015). The potential of Indonesian mangrove forests for global climate change mitigation. *Nature Climate Change*, *5*(12), 1089–1092. https://doi.org/10.1038/nclimate2734

Nixon, S. W. (1995). Coastal marine eutrophication: A definition, social causes, and future concerns. *Ophelia*, *41*(1), 199–219. https://doi.org/10.1080/00785236.1995.10422044

Rabalais, N. N., Turner, R. E., Díaz, R. J., & Justić, D. (2009). Global change and eutrophication of coastal waters. *ICES Journal of Marine Science*, *66*(7), 1528–1537. https://doi.org/10.1093/icesjms/fsp047

Regnier, P., Friedlingstein, P., Ciais, P., Mackenzie, F. T., Gruber, N., Janssens, I. A., Laruelle, G. G., Lauerwald, R., Luyssaert, S., Andersson, A. J., Arndt, S., Arnosti, C., Borges, A. V, Dale, A. W., Gallego-Sala, A., Goddéris, Y., Goossens, N., Hartmann, J., Heinze, C., … Thullner, M. (2013). Anthropogenic perturbation of the carbon fluxes from land to ocean. *Nature Geoscience*, *6*(8), 597–607. https://doi.org/10.1038/ngeo1830

Sohma, A., Shibuki, H., Nakajima, F., Kubo, A., & Kuwae, T. (2018). Modeling a coastal ecosystem to estimate climate change mitigation and a model demonstration in Tokyo Bay. *Ecological Modelling*, *384*(April), 261–289. https://doi.org/10.1016/j.ecolmodel.2018.04.019

Takahashi, T., Sutherland, S. C., Wanninkhof, R., Sweeney, C., Feely, R. A., Chipman, D. W., Hales, B., Friederich, G., Chavez, F., Sabine, C., Watson, A., Bakker, D. C. E., Schuster, U., Metzl, N., Yoshikawa-Inoue, H., Ishii, M., Midorikawa, T., Nojiri, Y.,

Körtzinger, A., … de Baar, H. J. W. (2009). Climatological mean and decadal change in surface ocean pCO2, and net sea–air CO2 flux over the global oceans. *Deep Sea Research Part II: Topical Studies in Oceanography*, *56*(8), 554–577. https://doi.org/10.1016/j.dsr2.2008.12.009

Tokoro, T., Hosokawa, S., Miyoshi, E., Tada, K., Watanabe, K., Montani, S., Kayanne, H., & Kuwae, T. (2014). Net uptake of atmospheric CO2 by coastal submerged aquatic vegetation. *Global Change Biology*, *20*(6), 1873–1884. https://doi.org/10.1111/gcb.12543

Wanninkhof, R. (1992). Relationship between wind speed and gas exchange over the ocean. *Journal of Geophysical Research: Oceans*, *97*(C5), 7373–7382. https://doi.org/10.1029/92JC00188

Chapter 2
Literature Review

2.1 Blue carbon in shallow coastal waters

In 2009, the United Nations Environment Programme (UNEP) and other organizations published a report entitled "Blue Carbon, A rapid response assessment" (Nellemann, 2009). This report revealed that about 55% of the carbon fixed by all living organisms on Earth is fixed by marine organisms. It was also proposed that the carbon fixed by marine organisms be called "blue carbon". The objects of carbon fixation in marine ecosystems include marine plants (mangroves, salt marshes, seagrasses, and marine phytoplankton) and marine shellfish.

The process of carbon fixation by marine organisms is as follows (Fig.2.1):

1. When the pCO_2 in the surface seawater is lower than the pCO_2 in the atmosphere, CO_2 will be absorbed from the atmosphere into seawater.

2. The CO_2 absorbed into seawater will be present in the water body as DIC through the solubility pump.

3. Marine organisms, such as phytoplankton and seagrasses, take DIC into their bodies through photosynthesis and other processes. This process of absorbing carbon into the organism is known as carbon "sequestration".

4. When DIC in surface seawater decreases, pCO_2 decreases, therefore, the process in 1. is accelerated.

5. Marine organisms die and sink to the bottom of the seawater and are eventually buried in the sediment. The carbon stored in the sediment can be stable for a long time. This process is known as carbon "storage".

The combination of sequestration and storage is known as carbon "fixation". It is indicated that organic matter stored in sediments will remain undecomposed (i.e., not released into the atmosphere) for decades to thousands of years (Chambers et al., 2001).

As a significant contributor to the global carbon cycle, the carbon cycle in intertidal wetlands (mangrove swamps, salt marshes, and seagrasses) and estuaries with higher vegetation cover is the focus of academic attention. About 45 to 71% of the carbon stored in the ocean is sequestered by shallow coastal water ecosystems (down to the photic layer at a depth of about 20 m) (Table 2.1). Shallow coastal water ecosystems account for only 0.05% of the total terrestrial vegetation on Earth; however, its annual carbon sequestration is comparable to that of all terrestrial vegetation. These results suggest that shallow coastal waters may be the most efficient carbon sink on Earth.

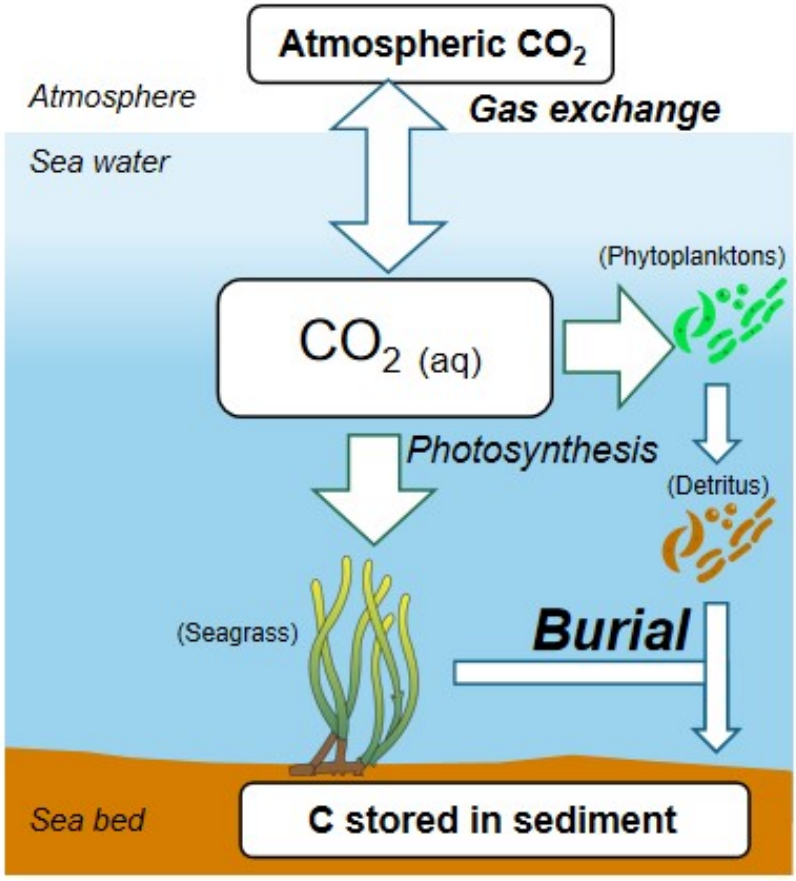

Figure 2.1 Conceptual diagram of carbon fixation by marine organisms in shallow coastal waters.

Table 2.1 Ratio of annual carbon sequestration by shallow coastal vegetation in the entire ocean (Nellemann, 2009).

Component	Area	Organic Carbon burial	
	Million km^2	Ton C ha^{-1} y^{-1}	Tg C y^{-1}
Vegetated habitats			
Mangroves	0.17 (0.3)	1.39, 0.20 – 6.54 (1.89)	17 – 23.6 (57)
Salt Marsh	0.4 (0.8)	1.51, 0.18 – 17.3 (2.37)	60.4 – 70 (190)
Seagrass	0.33 (0.6)	0.83, 0.56 – 1.82 (1.37)	27.4 – 44 (82)
Total vegetated habitats	0.9 (1.7)	1.23, 0.18 – 17.3 (1.93)	114 –131 (329)
Depositional areas			
Estuaries	1.8	0.5	81.0
Shelf	26.6	0.2	45.2
Total depositional areas			126.2
Total coastal burial			237.6 (454)
% vegetated habitats			46.89 (0.72)
Deep sea burial	330.0	0.00018	6.0
Total oceanic burial			243.62 (460)
% vegetated habitats			45.73 (0.71)

Note 1) Mean and maximum (in parentheses) estimates of annual organic carbon burial rate and area covered by blue carbon sinks. Carbon burial rates per hectare (from left to right are the mean, range of individual ecosystem estimates. Confidence limits are in parentheses) and global (as a range of reported global average rates of carbon burial, derived using different methods, with upper estimates derived using confidence limits for maximum area and average burial rates in parentheses). The data is for vegetated coastal areas and their percentage contribution to carbon burial in the coastal and global ocean (in brackets the burial rate and percentage contribution of vegetated habitats calculated from the upper estimates). Total burial rates of organic carbon in estuarine and shelf sediments and deep-sea sediments are provided for comparison. Data derived from reviews by Cebrián and Duarte (1996), Duarte et al. (2005a), and Bouillon et al. (2008).

2.2 CO_2 flux between the atmosphere and seawater (F_{CO2})

Shallow coastal waters with vegetation such as seagrass beds have been shown to have very high carbon storage. Although we know that shallow coastal waters have much higher carbon burial rates than the outer ocean as well as terrestrial vegetation, however, unlike terrestrial ecosystems, carbon burial rates underwater are not directly linked to atmospheric CO_2 removal because the water column separates the atmosphere from benthic systems in a complex carbon dynamics. Thus, although shallow coastal waters are considered a significant carbon reservoir, they may also be net emitters of atmospheric CO_2 through air-water CO_2 gas exchange (Chen et al., 2013; Regnier et al., 2013). In order to clarify the function of shallow coastal waters in reducing atmospheric CO_2, it is necessary to define not only the amount of carbon storage but also the amount of CO_2 uptake. The uptake of atmospheric CO_2 in shallow coastal waters is usually evaluated by calculating the CO_2 flux between the atmosphere and seawater (F_{CO2}).

The importance of coastal regions for atmospheric CO_2 uptake is receiving more attention in recent years (Bauer et al., 2013; Hjalmarsson et al., 2010; Kubo et al., 2017; Maher & Eyre, 2012; Tokoro et al., 2014), and current studies of F_{CO2} in coastal regions are not sufficient to predict the possible effects of human activities and other processes on the climate system. In the present study, there is still a lack of understanding of the control mechanisms by which some of the coastal regions behave as sources and others as sinks of atmospheric CO_2.

It has been suggested that the control of source/sink in coastal regions can be distinguished by latitude, e.g., coastal areas at low margins release CO_2 into the atmosphere due to high temperatures and significant inputs of organic carbon from terrestrial sources (Cai, 2011; Cai et al., 2006). However, the latitude division of source/sink areas is not an accurate description of the source/sink distribution trends in coastal regions, as more than temperature and organic matter inputs control the source/sink. In addition, the role of upwelling, riverine input, and other factors in the geological context of different regions and watersheds make the study of CO_2 sources/sinks in coastal areas highly uncertain.

Coastal regions are more significantly disturbed by anthropogenic disturbances than shelf seas. Biological activities brought about by processes such as anthropogenic inputs from terrestrial sources are more intense in coastal regions, where photosynthesis and aerobic respiration in coastal ecosystems will largely determine the role of CO_2 sources/sinks in this region (Bozec et al., 2012; Shadwick et al., 2011).

The current study of seasonal variability of CO_2 sources/sinks in coastal regions is also very challenging in time scales. Early studies by Cai's group considered the South Atlantic Bight as a source of atmospheric CO_2 (Löffler et al., 2012). Still, later studies with monthly observations and increased cross-sections found that it behaves as a source of atmospheric CO_2 in summer and exists as a net sink of atmospheric CO_2 throughout the year (-0.48 $mol \cdot m^{-2}\ yr^{-1}$). The main controlling factor of pCO_2 is the seasonal variation of sea surface temperature (Jiang et al., 2008a), so studying the target waters' higher spatial and temporal coverage is necessary.

In recent years, there has been considerable activity in studying CO_2 source/sink processes in shallow coastal waters. Borgesa et al. showed that the effects of intense primary production processes on the carbon cycle due to eutrophication in shallow coastal waters offset ocean acidification's impacts in surface seawater's carbon chemistry by numerical modeling (Borgesa & Gypensb, 2010). When measuring F_{CO2} in eelgrass beds (Tada et al., 2014), in seagrass beds along the Hashimizu coast facing Tokyo Bay (the entire water column includes not only seagrass but also phytoplankton), the pCO_2 in seawater is lower than that in the atmosphere, and atmospheric CO_2 tend to be absorbed from the atmosphere to seawater. Wind speed and pCO_2 in seawater are reported to be the leading direct influencing factors, while biological processes (respiration, decomposition, photosynthesis) are indirect influencing factors. It has also been reported that CO_2 in Lake Komuke, Hokkaido, is absorbed from the atmosphere to seawater, mainly around the center of the lake, directly influenced by wind speed and inflow load, and indirectly affected by biological processes (respiration, decomposition, and photosynthesis) in the lake. Bozec et al. found that biological processes (photosynthesis/respiration) were the main influences on the seasonal and daily variability of pCO_2 through 7 years of high-frequency pCO_2 records in Brest Bay (Bozec et al., 2011). This area behaved as a source of atmospheric CO_2 on an interannual scale due to more substantial aerobic

respiration processes. Moreover, the Scotian nearshore zone in the northwest Atlantic has a nearly equivalent effect of temperature and biological activity on pCO_2 throughout most of the year, except in spring, when this region behaves as a sink for atmospheric CO_2 due to water heating (Shadwick et al., 2011).

Based on previous studies, there is a great deal of uncertainty in estimating atmospheric CO_2 uptake in shallow coastal waters at this stage; this is mainly due to the complexity of the distribution and dynamics of pCO_2 in shallow coastal waters. The shallow coastal water is a complex system with many processes. Even within the same waters, there are often significant heterogeneities in the temporal and spatial distribution and dynamics of pCO_2. In addition to normal fluctuations in pCO_2 due to temperature changes (increasing temperature will reduce the solubility of CO_2 in water), upwelling, thermodynamic equilibrium, organic matter mineralization, and biological activity, and riverine input are the leading causes of this heterogeneity (Huertas et al., 2006; Ito et al., 2005; Jiang et al., 2008b). Moreover, many processes are antagonistic to each other; for example, while riverine input and upwelling can bring large amounts of nutrients and promote phytoplankton growth, reducing pCO_2 in the water column, the intake of large amounts of inorganic carbon and remineralization of organic matter will also cause an increase in pCO_2.

In order to understand the relationship between CO_2 fluxes and environmental factors in detail, it is necessary to conduct studies at more diverse shallow coastal waters and spatial and temporal scales. For example, only seagrass beds were targeted in the previous research mentioned above. Hence, the relationship between CO_2 fluxes and environmental factors in shallow coastal waters inhabited by seagrass beds and corals is unclear. In addition, the behavior of F_{CO2} and pCO_2 in seawater in such rare shallow coastal waters is currently unknown. The accumulation of measurement data allows us to analyze the factors that determine F_{CO2} and opens the way for future predictions.

2.3 CO_2 partial pressure (pCO_2) in seawater

CO_2 in the seawater is involved in chemical reactions at the air-water interface, the sediment-seawater interface, and seawater medium. It controls the pH of seawater and directly influences the chemical equilibrium processes in the sea, and plays an essential role in shaping the origin of life and maintaining the ecological environment. There are three forms of CO_2 in the sea: free CO_2 (CO_2(aq)), bicarbonate ion (HCO_3^-), and carbonate ion (CO_3^{2-}); in addition, carbonic acid (H_2CO_3) is also a form of seawater CO_2, but the percentage is tiny, only about 0.3% of the free CO_2 concentration (Fukushima et al., 2001).

Usually, we refer to CO_2 and H_2CO_3 together as "free CO_2", which can be expressed as pCO_2. As a critical parameter in the CO_2 system, pCO_2 is one of the most apparent parameters in the carbonate system of seawater with biological changes, and the determination of pCO_2 is essential for the study of air-water exchange and marine biological processes.

For pCO_2 in the surface seawater, the main factors affecting its concentration are as follows (Fig.2.2):

(1) Gas exchange through the air-sea interface

As mentioned in 2.2, the gas exchange of CO_2 between the surface waters of seawater and the atmosphere is mainly dominated by pCO_2 in the surface layer of seawater. Similarly, the gas exchange with atmospheric CO_2 also affects the pCO_2 in the surface layer of seawater ((1) in Fig.2.2). When pCO_2 in the atmosphere continues to increase due to human activities, the concentration of CO_2 in seawater will also gradually increase through the gas exchange. The ocean acidification caused by the increase of CO_2 in seawater is wide attention from the scientific community (McNeil & Matear, 2008; Northcott et al., 2019).

(2) Terrestrial input

The influence of terrestrial input on CO_2 system parameters is mainly concentrated at the confluence of rivers and oceans. Its variable physical, chemical, and biological processes lead to a much more complex biogeochemical cycle of carbon in shallow coastal waters than in marine waters, including all processes in the marine water

carbon cycle (air-sea interface gas exchange, vertical transport in the water column, sediment-seawater interface exchange, etc.), as well as it also includes the exchange of materials and energy with freshwater. In addition, a large amount of material coming from rivers and groundwater will significantly affect the carbon cycle mechanism in shallow coastal waters.

The most significant effect of terrestrial inputs on shallow coastal water ecosystems is the input of large amounts of nutrients and organic matter ((2), (3) in Fig.2.2). The nutrients and organic matter load from terrestrial sources have changed significantly with human activities on land use patterns, population growth due to urbanization, and industrial and domestic wastewater discharge, and has further altered the autotrophic/heterotrophic trophic status of the shallow coastal waters. In addition, bottom hypoxia due to estuarine eutrophication draws more attention from researchers (Conley et al., 2011; Kodama & Horiguchi, 2011).

(3) Biological activities

The carbon cycle in seawater is a complex biochemical process, and much of the downward transport of carbon in the ocean is related to marine biological processes. In the transmissive layer of the ocean surface, a large amount of phytoplankton absorbs CO_2 from seawater through photosynthesis. As a direct result, the pCO_2 value of surface seawater decreases, which is then converted into particulate organic carbon (POC) to form primary productivity ((4) in Fig.2.2). A portion of the POC produced by primary production is transferred to the bottom water column due to the sinking process ((8) in Fig.2.2). Some of the sinking processes will oxidize, decompose, and dissolve, and another part will be buried in the bottom sediment for a long time ((11) in Fig.2.2). The transfer of carbon from the ocean surface to the deep ocean by a series of biological processes such as organic matter production, sinking, and decomposition is called the "Biological Pump". The marine biological pump process dramatically enhances the ocean's ability to absorb CO_2 from the atmosphere. In contrast to the uptake of CO_2 by photosynthesis, respiration also affects the distribution of CO_2 in seawater through the release of CO_2 in the water column in marine areas ((5), (7) in Fig.2.2).

(4) Temperature and salinity

The dissolved CO_2 in seawater is influenced by temperature and salinity and correlates with them. Generally speaking, the higher the seawater temperature, the smaller the solubility of CO_2 and the higher the pCO_2.

Some researchers have tried to discuss the effect of temperature on the solubility of CO_2 in water by examining the impact of temperature and salinity variation on the dissociation constant of CO_2 in seawater and then using the changed dissociation constant to calculate the magnitude of the pCO_2 in water; when the salinity is fixed at 35, the ratio of alkalinity to dissolved inorganic carbon is 1.09, and the temperature varies between 0 and 35 °C, the relationship between temperature and pCO_2 is as follows:

$$\frac{d(\ln pCO_2)}{dt} = a \tag{2-1}$$

where *t*: water temperature (°C), and the value of *a* is between 0.0406 and 0.0422 (Millero, 2007).

If the effect of salinity on pCO_2 is taken into account, Millero suggested the following relationship between temperature, salinity, and pCO_2 for salinity between 17 and 36 (Millero, 2007):

$$\frac{d(\ln pCO_2)}{dt} = 0.044 - (8 \times 10^{-5}) \times S \tag{2-2}$$

where *t*: water temperature (°C), and *S*: salinity (psu).

From this relationship, it can be seen that the effect of temperature on pCO_2 is much greater than that of salinity. During periods of oligotrophy and low seawater temperatures, when biological activity is suppressed due to insufficient nutrient supply or low-temperature conditions, the temperature is likely to be the main factor influencing the distribution of pCO_2 in the water column (Bates et al., 1998; Borges et al., 2006).

(5) Ocean circulation

Changes in physical circulation in the ocean on different time scales can bring about significant changes in biogeochemical processes and air-water CO_2 exchange on a

regional or even larger spatial scale. Tsunogai et al. proposed the idea of the Continental Shelf Pump (CSP), which suggests that the horizontal transport of dissolved carbon from the shelf to the ocean at equal density along the seawater is another important mechanism for CO_2 removal from the shelf ((12) in Fig.2.2) (Tsunogai et al., 1999).

In addition, the upwelling of deep water rich in CO_2 and nutrients and the warming from deep cold water to warm water in the surface layer will lead to an increase in pCO_2 ((13) in Fig.2.2). On the one hand, the nutrients produced during remineralization of bottom waters enter the surface layer through upwelling and promote the primary production process in the surface layer. On the other hand, the upwelling of bottom CO_2-rich waters increases the pCO_2 of surface waters and supersaturates the pCO_2 of surface waters relative to the atmosphere.

The influence of upwelling on the trend of offshore CO_2 sources and sinks is undeniable. Although the seawater temperature is lower in the Bering Sea region at higher latitudes, this region behaves as a source region for atmospheric CO_2 because upwelling brings the bottom CO_2-rich waters to the surface layer (Mathis et al., 2011). In addition, due to the influence of upwelling brought by the monsoon, the Hong Kong nearshore marine area is a source area for atmospheric CO_2, both during the winter period when the water is heterotrophic and during the summer period when the water is autotrophic (Yuan et al., 2011). The offshore area that is more influenced by upwelling is defined by Dai et al. (Dai et al., 2013) as the oceanic control shelf, representing marine water's influence on the offshore through upwelling processes.

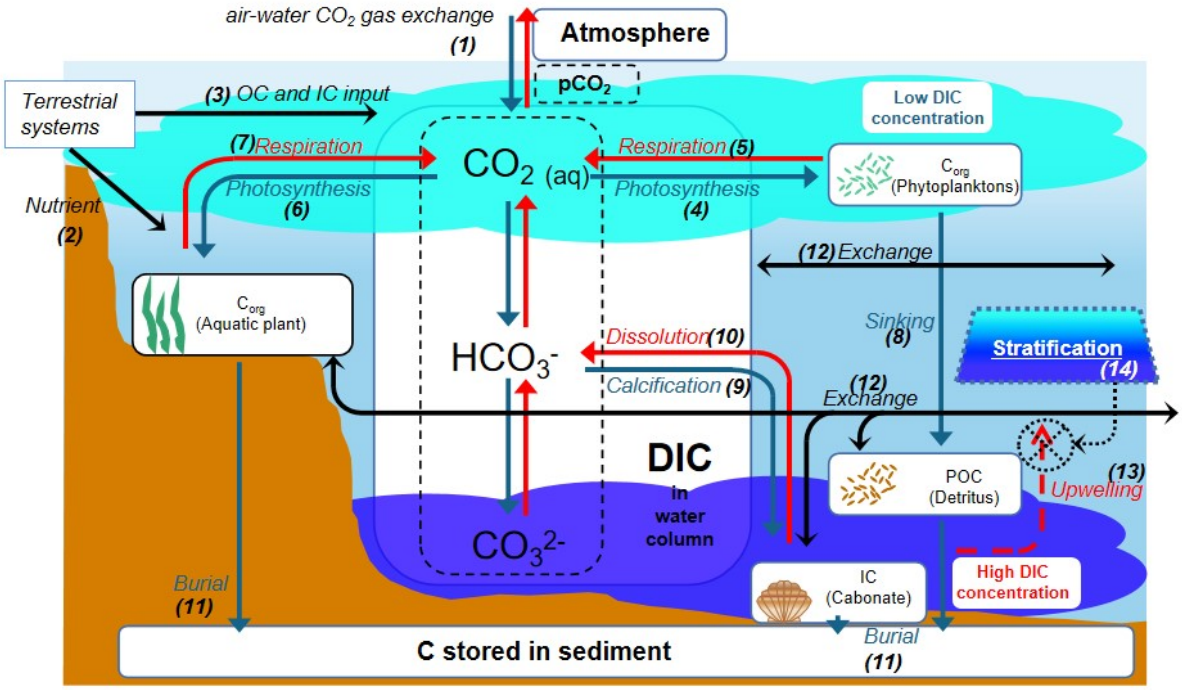

Figure 2.2 Schematic diagram of CO_2 dynamics in shallow coastal waters.

2.4 Effects of stratification on pCO_2 in shallow coastal waters

In shallow coastal waters, the pCO_2 in the surface water is usually lower than that in the bottom water after a series of physical processes and biological processes, but due to the influence of upwelling, the bottom CO_2-rich water is carried out to the surface layer and thus vertically mixed. However, stratification usually ((14) in Fig.2.2) occurs seasonally in shallow coastal waters, mainly in summer, inhibiting upwelling (Wakeham et al., 1987; Wiseman et al., 1997).

Previous studies have shown that pCO_2 is influenced by stratification. For example, a study in the coastal area of Osaka Bay (Fujii et al., 2011) reported that DIC decreased and pCO_2 decreased during stratification due to active photosynthesis of phytoplankton in the surface layer. On the other hand, in the bottom layer, DIC increased, and pCO_2 increased due to respiration of benthic organisms and mineralization of organic matter in the sediment.

In addition, the development of stratification inhibited the upwelling of suspended matter in the bottom layer and increased the transparency of the surface layer. As a result, the amount of light reaching the seawater increases, and the photosynthesis of the flora becomes more active. As a result, pCO_2 in the surface layer decreases (Chen et al., 2008).

In addition, vertical mixing is inhibited by stratification, and the upwelling of seawater with high DIC ($\fallingdotseq$ high pCO_2) in the bottom layer is also inhibited. As a result, the pCO_2 in the surface layer remained very low. However, the settling of particulate organic matter (POM) is not prevented by stratification (Koné et al., 2009). Therefore, the development of stratification did not affect the precipitation and deposition of organic matter.

Nevertheless, very few studies consider the effects of stratification on CO_2 fluxes and pCO_2 dynamics in shallow coastal waters. In order to explain the effect of stratification on pCO_2 in shallow coastal waters and to obtain a more comprehensive understanding of the complete carbon cycle mechanism in shallow coastal waters, as shown in Fig.2.2, we need to collect and analyze more data on CO_2 dynamics with

high spatial and temporal coverage in stratified shallow coastal waters. In this way, it is expected that the accuracy of future global estimates of atmospheric CO_2 reduction in shallow coastal waters will be improved.

References

Bates, N. R., Takahashi, T., Chipman, D. W., & Knap, A. H. (1998). Variability of pCO2 on diel to seasonal timescales in the Sargasso Sea near Bermuda. *Journal of Geophysical Research: Oceans*, *103*(C8), 15567–15585.

Bauer, J. E., Cai, W. J., Raymond, P. A., Bianchi, T. S., Hopkinson, C. S., & Regnier, P. A. G. (2013). The changing carbon cycle of the coastal ocean. *Nature*, *504*(7478), 61–70. https://doi.org/10.1038/nature12857

Borges, A. V, Schiettecatte, L. S., Abril, G., Delille, B., & Gazeau, F. (2006). Carbon dioxide in European coastal waters. *Estuarine, Coastal and Shelf Science*, *70*(3), 375–387.

Borgesa, A. V, & Gypensb, N. (2010). Carbonate chemistry in the coastal zone responds more strongly to eutrophication than ocean acidification. *Limnology and Oceanography*, *55*(1), 346–353.

Bouillon, S., Borges, A. V, Castañeda-Moya, E., Diele, K., Dittmar, T., Duke, N. C., Kristensen, E., Lee, S. Y., Marchand, C., & Middelburg, J. J. (2008). Mangrove production and carbon sinks: a revision of global budget estimates. Global Biogeochemical Cycles, 22(2).

Bozec, Y., Cariou, T., Macé, E., Morin, P., Thuillier, D., & Vernet, M. (2012). Seasonal dynamics of air–sea CO2 fluxes in the inner and outer Loire estuary (NW Europe). *Estuarine, Coastal and Shelf Science*, *100*, 58–71. https://doi.org/10.1016/j.ecss.2011.05.015

Bozec, Y., Merlivat, L., Baudoux, A.-C., Beaumont, L., Blain, S., Bucciarelli, E., Danguy, T., Grossteffan, E., Guillot, A., & Guillou, J. (2011). Diurnal to inter-annual dynamics of pCO2 recorded by a CARIOCA sensor in a temperate coastal ecosystem (2003–2009). *Marine Chemistry*, *126*(1–4), 13–26.

Cai, W. J. (2011). Estuarine and Coastal Ocean Carbon Paradox: CO2 Sinks or Sites of Terrestrial Carbon Incineration? *Annual Review of Marine Science*, *3*(1), 123–145. https://doi.org/10.1146/annurev-marine-120709-142723

Cai, W. J., Dai, M., & Wang, Y. (2006). Air-sea exchange of carbon dioxide in ocean margins: A province-based synthesis. *Geophysical Research Letters*, *33*(12). https://doi.org/10.1029/2006GL026219

Cebrián, J., & Duarte, C. M. (1995). Plant growth-rate dependence of detrital carbon storage in ecosystems. Science, 268(5217), 1606–1608.

Chambers, J. Q., Higuchi, N., Tribuzy, E. S., & Trumbore, S. E. (2001). Carbon sink for a century. *Nature*, *410*(6827), 429. https://doi.org/10.1038/35068624

Chen, C. T. A., Huang, T. H., Chen, Y. C., Bai, Y., He, X., & Kang, Y. (2013). Air–sea exchanges of CO2 in the world's coastal seas. *Biogeosciences*, *10*(10), 6509–6544. https://doi.org/10.5194/bg-10-6509-2013

Chen, C. T. A., Zhai, W., & Dai, M. (2008). Riverine input and air–sea CO2 exchanges near the Changjiang (Yangtze River) Estuary: Status quo and implication on possible future changes in metabolic status. *Continental Shelf Research*, *28*(12), 1476–1482. https://doi.org/10.1016/j.csr.2007.10.013

Conley, D. J., Carstensen, J., Aigars, J., Axe, P., Bonsdorff, E., Eremina, T., Haahti, B.-M., Humborg, C., Jonsson, P., & Kotta, J. (2011). Hypoxia is increasing in the coastal zone of the Baltic Sea. *Environmental Science & Technology*, *45*(16), 6777–6783.

Dai, M., Cao, Z., Guo, X., Zhai, W., Liu, Z., Yin, Z., Xu, Y., Gan, J., Hu, J., & Du, C. (2013). Why are some marginal seas sources of atmospheric CO2? *Geophysical Research Letters*, *40*(10), 2154–2158.

Duarte, C. M., Middelburg, J. J., & Caraco, N. (2005). Major role of marine vegetation on the oceanic carbon cycle. Biogeosciences, 2(1), 1–8. https://doi.org/10.5194/bg-2-1-2005

Fujii, T., Komai, Y., & Fujiwara, T. (2011). Carbon Dioxide Dynamics in Coastal Regions of Osaka Bay. *Journal of Japan Society of Civil Engineers, Ser. B2 (Coastal Engineering)*, *67*(2), I_911–I_915. https://doi.org/10.2208/kaigan.67.i_911

Fukushima, T., Ishibashi, T., & Imai, A. (2001). Chemical characterization of dissolved organic matter in Hiroshima Bay, Japan. *Estuarine, Coastal and Shelf Science*, *53*(1), 51–62.

Hjalmarsson, S., Chierici, M., & Anderson, L. G. (2010). Carbon dynamics in a productive coastal region—The Skagerrak. *Journal of Marine Systems*, *82*(4), 245–251. https://doi.org/https://doi.org/10.1016/j.jmarsys.2010.05.013

Huertas, I. E., Navarro, G., Rodríguez-Gálvez, S., & Lubián, L. M. (2006). Temporal patterns of carbon dioxide in relation to hydrological conditions and primary production in the northeastern shelf of the Gulf of Cadiz (SW Spain). *Deep Sea Research Part II: Topical Studies in Oceanography*, *53*(11–13), 1344–1362.

Ito, R. G., Schneider, B., & Thomas, H. (2005). Distribution of surface fCO2 and air–sea fluxes in the Southwestern subtropical Atlantic and adjacent continental shelf. *Journal of Marine Systems*, *56*(3–4), 227–242.

Jiang, L., Cai, W., Wanninkhof, R., Wang, Y., & Lüger, H. (2008a). Air-sea CO2 fluxes on the US South Atlantic Bight: Spatial and seasonal variability. *Journal of Geophysical Research: Oceans*, *113*(C7).

Jiang, L. Q., Cai, W. J., & Wang, Y. (2008b). A comparative study of carbon dioxide degassing in river-and marine-dominated estuaries. *Limnology and Oceanography*, *53*(6), 2603–2615.

Kodama, K., & Horiguchi, T. (2011). Effects of hypoxia on benthic organisms in Tokyo Bay, Japan: a review. *Marine Pollution Bulletin*, *63*(5–12), 215–220.

Koné, Y. J. M., Abril, G., Kouadio, K. N., Delille, B., & Borges, A. V. (2009). Seasonal Variability of Carbon Dioxide in the Rivers and Lagoons of Ivory Coast (West Africa). *Estuaries and Coasts*, *32*(2), 246–260. https://doi.org/10.1007/s12237-008-9121-0

Kubo, A., Maeda, Y., & Kanda, J. (2017). A significant net sink for CO2 in Tokyo Bay. *Scientific Reports*, *7*(1), 44355. https://doi.org/10.1038/srep44355

Löffler, A., Schneider, B., Perttilä, M., & Rehder, G. (2012). Air–sea CO2 exchange in the Gulf of Bothnia, Baltic Sea. *Continental Shelf Research*, *37*, 46–56. https://doi.org/10.1016/j.csr.2012.02.002

Maher, D. T., & Eyre, B. D. (2012). Carbon budgets for three autotrophic Australian estuaries: Implications for global estimates of the coastal air–water CO2 flux. *Global Biogeochemical Cycles*, *26*(1). https://doi.org/10.1029/2011GB004075

Mathis, J. T., Cross, J. N., & Bates, N. R. (2011). Coupling primary production and terrestrial runoff to ocean acidification and carbonate mineral suppression in the eastern Bering Sea. *Journal of Geophysical Research: Oceans*, *116*(C2).

McNeil, B. I., & Matear, R. J. (2008). Southern Ocean acidification: A tipping point at 450-ppm atmospheric CO₂ *Proceedings of the National Academy of Sciences*, *105*(48), 18860 LP – 18864. https://doi.org/10.1073/pnas.0806318105

Millero, F. J. (2007). The marine inorganic carbon cycle. *Chemical Reviews*, *107*(2), 308–341.

Nellemann, C. (2009). *Blue carbon. A UNEP rapid response assessment*.

Northcott, D., Sevadjian, J., Sancho-Gallegos, D. A., Wahl, C., Friederich, J., & Chavez, F. P. (2019). Impacts of urban carbon dioxide emissions on sea–air flux and ocean acidification in nearshore waters. *PLOS ONE*, *14*(3), e0214403. https://doi.org/10.1371/journal.pone.0214403

Regnier, P., Friedlingstein, P., Ciais, P., Mackenzie, F. T., Gruber, N., Janssens, I. A., Laruelle, G. G., Lauerwald, R., Luyssaert, S., Andersson, A. J., Arndt, S., Arnosti, C., Borges, A. V, Dale, A. W., Gallego-Sala, A., Goddéris, Y., Goossens, N., Hartmann, J., Heinze, C., … Thullner, M. (2013). Anthropogenic perturbation of the carbon fluxes from land to ocean. *Nature Geoscience*, *6*(8), 597–607. https://doi.org/10.1038/ngeo1830

Shadwick, E. H., Thomas, H., Azetsu-Scott, K., Greenan, B. J. W., Head, E., & Horne, E. (2011). Seasonal variability of dissolved inorganic carbon and surface water pCO2 in the Scotian Shelf region of the Northwestern Atlantic. *Marine Chemistry*, *124*(1), 23–37. https://doi.org/10.1016/j.marchem.2010.11.004

Tada, K., Tokoro, T., Watanabe, K., Moki, H., & Kuwae, T. (2014). SPATIAL DISTRIBUTION OF AIR-SEA CO2 FLUX AND ITS INFLUENCING FACTORS AT THE LAKE KOMUKE, HOKKAIDO. Journal of Japan Society of Civil Engineers, Ser. B3 (Ocean Engineering), 70(2), I_1188-I_1193. https://doi.org/10.2208/jscejoe.70.I_1188

Tokoro, T., Hosokawa, S., Miyoshi, E., Tada, K., Watanabe, K., Montani, S., Kayanne, H., & Kuwae, T. (2014). Net uptake of atmospheric CO2 by coastal submerged aquatic vegetation. *Global Change Biology*, *20*(6), 1873–1884. https://doi.org/10.1111/gcb.12543

Tsunogai, S., Watanabe, S., & Sato, T. (1999). Is there a "continental shelf pump" for the absorption of atmospheric CO2? *Tellus B: Chemical and Physical Meteorology*, *51*(3), 701–712.

Wakeham, S. G., Howes, B. L., Dacey, J. W. H., Schwarzenbach, R. P., & Zeyer, J. (1987). Biogeochemistry of dimethylsulfide in a seasonally stratified coastal salt pond. *Geochimica et Cosmochimica Acta*, *51*(6), 1675–1684. https://doi.org/10.1016/0016-7037(87)90347-4

Wiseman, W. J., Rabalais, N. N., Turner, R. E., Dinnel, S. P., & MacNaughton, A. (1997). Seasonal and interannual variability within the Louisiana coastal current: stratification and hypoxia. *Journal of Marine Systems*, *12*(1), 237–248. https://doi.org/10.1016/S0924-7963(96)00100-5

Yuan, X. C., Yin, K., Cai, W. J., Ho, A. Y., Xu, J., & Harrison, P. J. (2011). Influence of seasonal monsoons on net community production and CO 2 in subtropical Hong Kong coastal waters. *Biogeosciences*, *8*(2), 289–300.

Chapter 3

Field Measurement on Seawater CO_2 under Different Stratification States in the Yatsushiro Sea

3.1 Introduction

Of the carbon fixed by organisms on Earth, about 55% is fixed by marine organisms, which is called "blue carbon" (Nellemann & Corcoran, 2009). In particular, shallow coastal waters with vegetation such as seagrass beds have a high capacity to store carbon in sediments and are considered essential for reducing atmospheric CO_2, a typical greenhouse gas (Mcleod et al., 2011; Watanabe & Kuwae, 2015). However, there is a lack of knowledge and data to understand the actual state of blue carbon, and the current estimation results are highly variable and uncertain. In addition to water temperature, salinity, and wind speed, pCO_2 is used to calculate the amount of CO_2 absorbed by seawater. On the other hand, pCO_2 in shallow coastal waters varies greatly in space and time due to the influence of physical processes such as flow and biological processes such as photosynthesis by aquatic plants, calcification by corals. In other words, in order to improve the accuracy of calculating the amount of CO_2 absorbed by seawater in shallow coastal waters, it is necessary to obtain data on pCO_2 based on various conditions such as geography, topography, and ecosystems.

In previous studies, it has been reported that the dissolved inorganic carbon concentration (DIC) in the surface layer decreases with the development of stratification, and pCO_2 becomes smaller (Fujii et al., 2011; Tada, et al., 2018). However, the effects of biological processes (photosynthesis) on DIC reduction during stratification have not been investigated in detail. In addition, Tada et al. modeled pCO_2 and showed the necessity of examining the relationship between stratification and pCO_2 in more detail (Tada, et al., 2018).

In this study, we conducted several field measurements in the Yatsushiro Sea, where no measurements about CO_2 dynamics have been conducted in the past. The bay is characterized by the presence of corals and seagrasses in the temperate zone. The

field measurements were conducted during the strong stratification period, weak stratification period, and well-mixed period in order to understand in detail the effect of stratification conditions on pCO_2.

3.2 Overview of Field Measurement

3.2.1 Description of the Yatsushiro Sea

The Yatsushiro Sea, located in the western part of Kyushu island (Fig.3.1), is extremely closed compared to other inland bays in Japan and is characterized by a large tidal range and vast tidal flats and brackish water areas (Table 3.1). Therefore, a unique ecosystem has developed in the bay's shallow waters, with high biodiversity and rich biological productivity. The northern part of the bay has a solid inner bay character and tidal flats, while the southern part of the bay, south of the central part, has a rapid seawater exchange and a reef-like seafloor that gradually becomes more pelagic. The southern part of the Yatsushiro Sea and the sea area around the Amakusa Islands have been selected by the Ministry of the Environment as “a sea area of high importance from the viewpoint of biodiversity.” The bay is located along the coast of Kumamoto Prefecture, where the Tsushima Warm Current, a branch of the Kuroshio Current, flows. In particular, the southwestern part of the Amakusa Islands surrounding the bay is a significant habitat for reef-building corals in western Kyushu. The fifth nature conservation survey conducted by the Ministry of the Environment confirmed the existence of seagrass beds covering an area of about 1,141 ha.

The area of the bay is about 1,200 km^2. The basin area of the rivers flowing into the bay is approximately 3,000 km^2, and the major rivers are the Kuma River, the Hikawa River, and the Minamata River. The Kuma River is a first-class river with a basin area of about 1,880 km^2 and accounts for about 60% of rivers flowing into the Yatsushiro Sea. The inflow of fresh water during the rainy season from June to August lowers the salinity throughout the sea area. In the inner part of the bay, the salinity decreases significantly due to the increased inflow of rivers such as the Kuma River.

The Yatsushiro Sea is considered to be a unique coastal area in terms of physical conditions such as flow, topography, and ecosystem. Since there is a lack of knowledge about phytoplankton, seagrasses such as eelgrass, and corals inhabiting the bay at the same time, new research results on air-sea CO_2 flux, pCO_2 in seawater, and related environmental factors in the bay are expected.

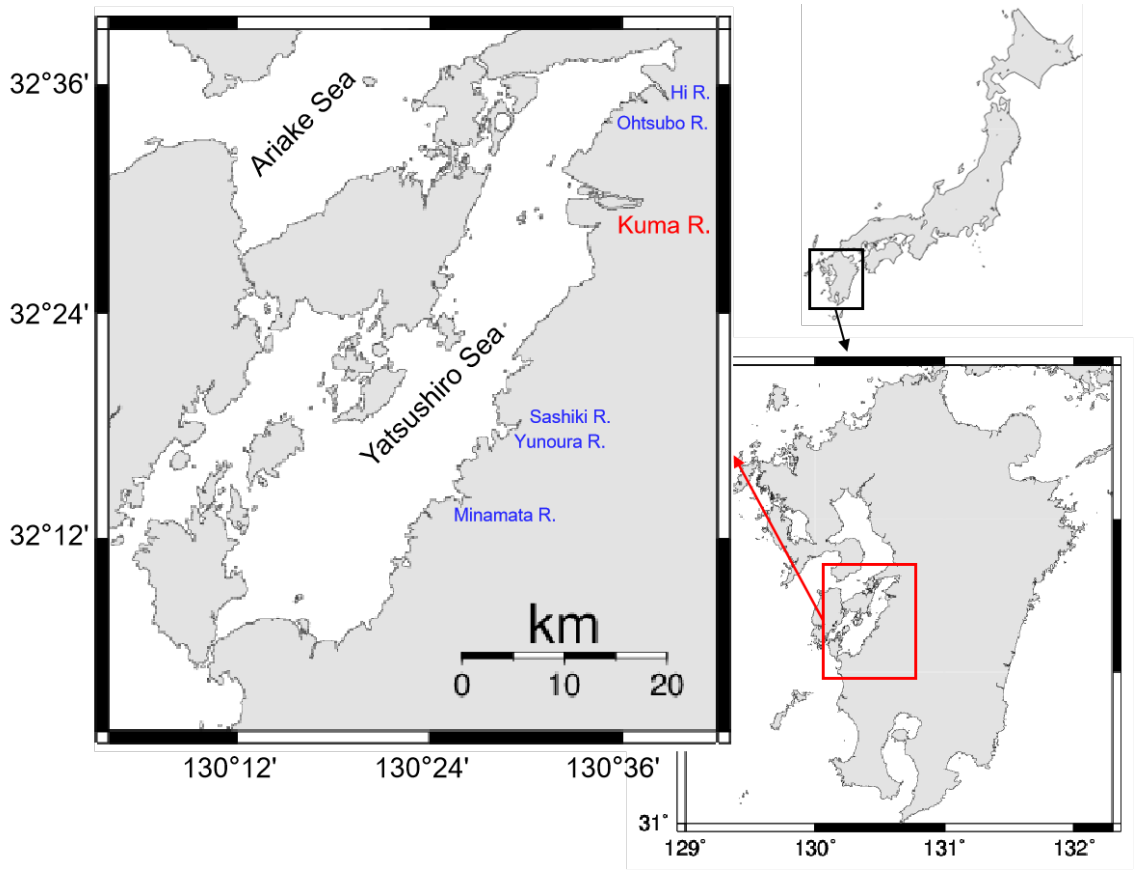

Figure 3.1 Location of the Yatsushiro Sea and the major rivers.

Table 3.1 Characteristics of the Yatsushiro Sea and comparison with other semi-enclosed bays (Ministry of the Environment, Japan (2006)).

Item	Ariake Sea	Yatsushiro Sea	Tachibana Bay	Tokyo Bay	Ise Bay	Osaka Bay
Water area (km^2)	1,700	1,200	745	1,380	2,342	1,447
Volume (km^3)	34	22	34	62	39	44
Average water depth (m)	20	22	48	45	17	30
Tidal flat area (ha)	18,841	4,085	406	1,734	2,901	79
Segrass bed area (ha)	1,599	1,141	1,661	1,428	2,278	110
Average tide difference [Spring tide] (m)	5.4	3.7	2.9	1.9	2.4	1.4
Geographical enclosed index	12.9	32.5	1.3	1.8	1.5	1.1
Inflow of first-class rivers (10^6m^3/year)	10,049	4,992	-	6,256	23,232	8,898
Basin area	8,420	3,409	342	7,597	16,191	5,766
Population in the basin (in thousands)	3,293	453	124	28,643	10,941	15,489

3.2.2 Location and date of field measurements

The measurement points are shown in Fig.3.2. The water sampling points of the end members are also shown in Fig.3.2. The measurement points were selected in the waters around the estuary of the Kuma River because of the strong influence of freshwater inflow from the river, which accounts for about 60% of the total area of the Yatsushiro Sea. There is a slight difference in the location of measurement points between summer and winter because gill nets were set at the points in winter, and it was not easy to anchor at the same points. The point was chosen to avoid shipping routes and fixed nets. The measurement vessel is a fishing boat (owned by the Minamata Fishermen's Cooperative Association) for summer measurements and a practice vessel, the Tsuruyo Maru (owned by Nagasaki University), for winter measurements.

The field measurements were conducted on August 26, 2018, during the summer stratification period, December 7, 2018, during the winter mixing period, and August 2, 2019, during the summer stratification period. If we consider only the development of stratification, it is more appropriate to conduct the measurements during the low tide period. However, there is no case study on pCO_2 in seawater in the Yatsushiro Sea, so it is unclear to what extent the phenomena in the bay affect pCO_2 in seawater. In addition, various factors, such as physical processes such as flow, affect pCO_2 in seawater. Therefore, in this study, we decided to conduct the measurement during the high tide period, when the horizontal flow fluctuation is large, and the physical phenomena such as upwelling are likely to occur clearly. The measurement time was from high tide around 9:00 to low tide around 15:00.

In the summer of 2018, the measurement point was located at 32°27' 30" N, 130°27' 37" E, and the water depth was about 20 m at high tide. The minimum temperature is about 29°C, and the maximum is about 33°C. In the winter of 2018, the measurement point was located at 32°27'14" N, 130°28'18" E, and the water depth was about 21 m at high tide. The maximum temperature was about 13.4°C (1:00), and the minimum temperature was 10.4°C (15:00), and the weather was cloudy all day. In the summer of 2019, the measurement point was at 32°27' 30" N, 130°27' 37" E (the same point as in the summer of 2018), and the water depth was about 21 m at high tide. The

maximum temperature was about 35.5°C (15:00), and the minimum temperature was 25.7°C (04:00), and the weather was clear all day.

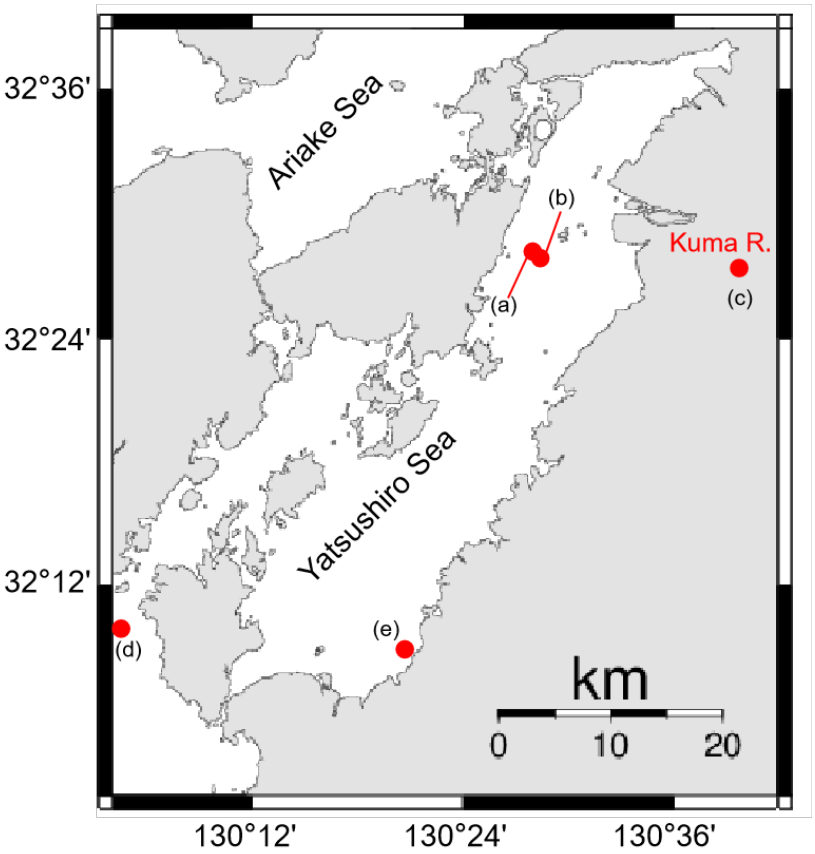

Figure 3.2 Field measurement points and end member water sampling points.

Note 1) (a): Summer measurement point, (b): Winter measurement point,

(c): end member sampling point for river water (Kuma River),

(d): Water sampling point for external seawater (Ushibuka),

(e): end member sampling point for open seawater (Minamata Southern).

3.3 Methods

3.3.1 Water quality measurement and sampling

CTD measurements and water sampling were conducted during the half-tide period from high tide (9:00 am) to low tide (3:00 pm). CTD measurements included vertical profiles of water temperature, salinity, density. Water samples were for analysis of DIC and total alkalinity (TA). CTD measurements were conducted approximately every 20 minutes using a multi-item water quality meter (ProDSS, YSI). Water samples were collected at high tide, 1.5 hours after high tide, at the full ebbing tide, 1.5 hours before low tide, and at low tide. The samples were collected in 250-mL Duran bottles, and the DIC was fixed by injecting secondary mercury chloride solution. The value of DIC and TA were analyzed using a flow-through carbonate analyzer (MDO-02, made by Kimoto Electronics Co., Ltd.) and a total alkalinity titrator (ATT-15, made by Kimoto Electronics Co., Ltd.) owned by Kitami Institute of Technology. From the obtained DIC, TA, salinity, and water temperature, pCO_2 is calculated from the carbon-based chemical equilibrium relational semi-empirical equation (Zeebe & Wolf-Gladrow, 2001). The equation used in this study is the one developed in the 'seacarb' package in R (Lavigne & Gattuso, 2010).

3.3.2 Indicators of biological processes (ΔDIC, ΔTA)

(1) Description of ΔDIC, ΔTA

In the case of seawater, bicarbonate ions account for more than 90% of DIC. When the CO_2 concentration in water changes, bicarbonate, and carbonate ions compensate for part of the change in CO_2 concentration; DIC changes depending on biological processes, with DIC increasing when respiration and decomposition activities dominate and decrease when photosynthesis activities dominate. A positive correlation (0.37) between ΔDIC and pCO_2 in water has been shown in previous studies (Tada et al., 2015).

In addition, there is a strong positive correlation between salinity and DIC. The higher the salinity, the higher the DIC, which increases the amount of CO_2 taken up into the water as ions such as bicarbonate ions, resulting in a higher DIC. Therefore, in the absence of biological processes, DIC can be determined by a simple mixing ratio of freshwater and open seawater, assuming a steady-state DIC (end member) at the inflow/outflow boundary.

TA fluctuates due to the calcification of calcium carbonate by corals and other organisms that form the calcium carbonate skeleton. When calcium carbonate dissolves, TA increases, and when it precipitates, TA decreases. In other words, TA decreases in the presence of organisms such as corals. A previous study showed that there is a negative correlation (-0.17) between ΔTA and pCO_2 in water. There is also a strong positive correlation between salinity and TA (Tada et al., 2015). This is because the higher the salinity, the more minerals such as calcium and magnesium are taken up, and the higher the TA. Therefore, in the absence of the influence of biological processes, TA can be determined by a simple mixing ratio of freshwater and open seawater, assuming a steady-state TA (end member) at the outflow/inflow boundary. Fig.3.3 shows a scatter plot of salinity and total alkalinity based on previous studies conducted in Ise Bay, Tokyo Bay, and Osaka Bay (Taguchi et al., 2009). River water data (end members) flowing into each area are also plotted in the scatter diagram. The asterisk (*) in the figure is the average value (salinity 34.82, total alkalinity 2293 μmol/kg) of the North Pacific Subtropical Mode Water (NPSTMW) obtained from the CDIAC (Carbon Dioxide Information Analysis Center) database. Table 3.2 shows the regression analysis's standard errors and correlation

coefficients of total alkalinity with salinity in each sea area. The correlation coefficients are high at 0.99 or higher for all the sea areas, and the scatter plot of salinity and total alkalinity is almost a straight line. In addition, the total alkalinity of the river water end members and the open sea end members are almost conservatively mixed, indicating that the influence of biological processes such as coral calcification is negligible in these waters.

In the analysis of the variability of pCO_2 in seawater, it is known that the indexes of biological activity (ΔDIC and ΔTA) are fundamental influencing factors. However, in studies of seawater pCO_2 in temperate coastal areas in Japan, the effect of calcification by corals and other organisms is considered negligible, and the method of analyzing seawater pCO_2 fluctuations using only ΔDIC is common.

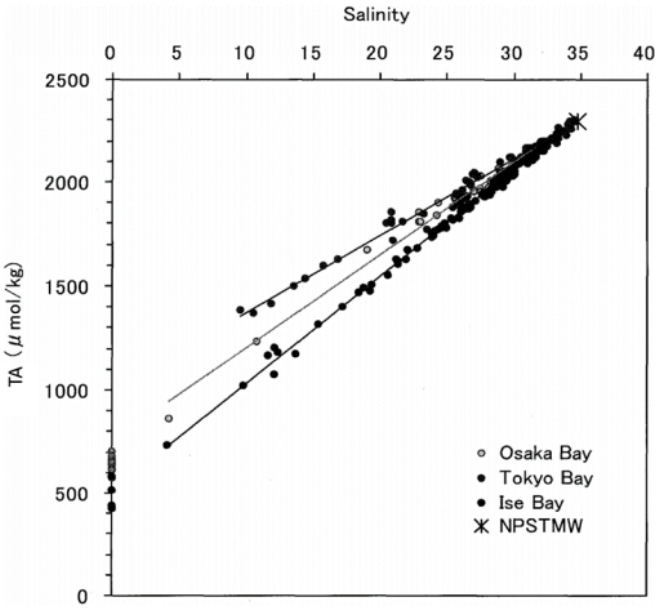

Figure 3.3 Scatter plot of salinity and total alkalinity in 3 Japanese bays (Taguchi et al., 2009).

Note 1) NPSTMW： North Pacific Sub-Tropical Mode Water

Table 3.2 Regression analysis of total alkalinity against salinity (Taguchi et al., 2009).

Sea	R	n	a	b	SE
Ise Bay	0.997	159	51.53	518	21
Tokyo Bay	0.991	59	36.77	1006	34
Osaka Bay	0.991	33	44.55	759	35

Note 1) R: correlation coefficient; n: number of samples; a: regression coefficient; b: intercept; SE: standard error of regression equation (standard deviation of residuals).

(2) Calculation of ΔDIC and ΔTA

As shown in (1), DIC and TA can be determined by the simple mixing ratio of freshwater and open seawater, assuming that the end members at the outflow/inflow boundary are in a steady state without the influence of biological processes. Fig.3.4 shows the conceptual diagram for calculating ΔDIC, and ΔTA is calculated similarly.

However, this calculation method has a problem that changes in DIC and TA caused by inflow water from rivers other than the one targeted as the inflow point affect ΔDIC and ΔTA. The same problem arises when seawater flows into the inner bay from a point other than the one set as the outflow point. In the Yatsushiro Sea, which is the target of this study, the closure of the inner bay is exceptionally high, and the Kuma River alone accounts for most of the river inflow, so such problems are unlikely to occur. However, in order to understand the factors of ΔDIC and ΔTA more precisely, it is necessary to study in detail the influence of the outflow and inflow from the Ariake Sea and river water from other rivers than the Kuma River on the Yatsushiro Sea.

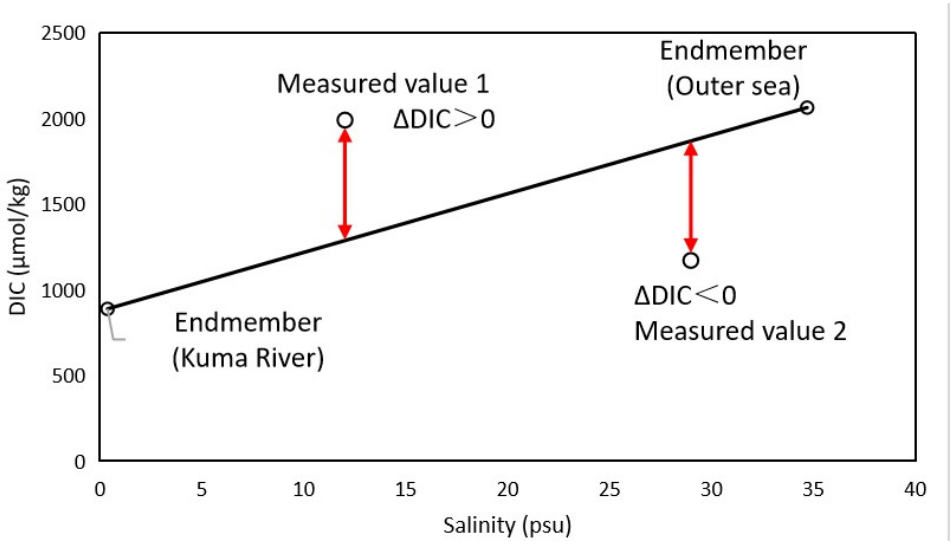

Figure 3.4 Conceptual diagram of ΔDIC calculation (ΔTA is calculated similarly).

(3) Water sampling for end members

In order to calculate the variation of DIC and TA by biological processes, it is necessary to measure DIC and TA in rivers and the open sea (at the inflow/outflow boundary). This value at the outflow/inflow boundary point is called the end members. In this study, the river water was sampled at Yokogawa, Kuma River (32° 28′09.0″N, 130°38′37.7″E). The Kuroshio Subsurface Water (KSSW) sampled by the previous study (Qu et al., 2018) was used as the end member of the open sea. Water samples for the river water were taken at 13:25 on December 15, 2018 and 17:50 on August 1, 2019, at Yokogawa, Kuma River. In addition water sampling in the Ushibuka was conducted at 17:00 on December 7, 2018, the same day as the winter measurement schedule. Another water sample was taken at 16:06~16:20 on December 15, 2018, at the Minamata.

In the Kuma River, water samples were collected at Yokogawa, the downstream flow station, except for the tidal zone. Water was collected by bucket sampling from the bridge. One preliminary sample was also taken. In the Ushibuka and the Minamata, bucket samples were taken from the ship, and one preliminary sample was also taken. For each sampling, secondary mercury chloride solution was added immediately after sampling for fixing the carbonate.

(4) Review the validity of the sampled end members and reset the end members

The data from Ushibuka and Minamata, which were collected as end members of the open sea water in the field measurements, were found to be inappropriate as end members because of the influence of organisms by comparison with previous studies.

In a previous study, three empirical equations for calculating TA from salinity based on data from field measurements were presented (Table 3.2) (Taguchi et al., 2009). These three areas are located in the temperate zone, and the correlation coefficient R of the empirical equation is more than 0.99, which means that the TA can be explained by salinity alone.

Based on these three empirical equations, Table 3.3 compares the expected TA without the influence of biological processes calculated from the salinity of the water sampling results and the TA from water sampling. In both Minamata and Ushibuka, the TA was smaller than that estimated from salinity in the area without biological processes. It was confirmed that the data from Ushibuka and Minamata, which were collected as end members of the open seawater, were inappropriate because of the influence of biological processes.

Table 3.3 Comparison between estimated values from salinity using empirical equation and measured values.

	Previous study		**Minamata**	**Ushibuka**
Salinity (psu)	34.58	35.15	34.58	35.15
DIC (μmol/kg)	-	-	1985.17	1970.99
TA (μmol/kg)	2292.32	2317.56	2222.61	2247.37

In this study, we use the Kuroshio Subsurface Water (KSSW) measured by a previous study as the end member of the open seawater (Qu et al., 2018). The KSSW is measured at depths of 100 to 300 meters. It is known that the Tsushima Current, which is separated from the Kuroshio Current, flows into the Yatsushiro Sea.

Table 3.4 shows a comparison between the measured values of KSSW (Kuroshio Subsurface Water), the TA calculated from salinity by the empirical equation of Taguchi et al. (see Table 3.4), and the measured values of this study. Comparing the TA by KSSW and Taguchi et al. shows that the values of TA are almost identical. This indicates that the relationship between salinity and TA at the Qu et al. site is

comparable to that measured by Taguchi et al. in three domestic seas and that the Qu et al. measurement results can be regarded as the general external seawater flowing around Japan.

Table 3.4 Comparison of measured values by Qu et al. (2018) with TA determined from salinity based on empirical equations by Taguchi et al. (2015) and measured values in this study.

	Kuma River (Summer)	**Kuma River (Winter)**	**KSSW**	**Previous study (Taguchi et al.,)**	**Minamata**	**Ushibuka**
Salinity (psu)	0.16	0.37	34.69	34.69	34.58	35.15
DIC (μmol/kg)	814.29	888.81	2064	-	1985.17	1970.99
TA (μmol/kg)	662.87	794.36	2293	2286	2222.61	2247.37

Note 1) Values used as end members in this study are indicated by yellow markers.

3.4 Results and Discussions

3.4.1 Confirmation of stratification

Fig.3.5 shows isopleths of temperature, salinity, and seawater density σ_t on August 26, 2018, during the summer stratification period, December 7, 2018, during the well-mixed period, and August 2, 2019, the summer stratification period. The vertical axis represents the water depth, the horizontal axis represents the time trend, and the colors represent the water temperature, salinity, and seawater density σ_t. On August 2, 2019, the σ_t results confirmed the development of strong density stratification. Weak density stratification development was measured on August 26, 2018, and well mixing of seawater was measured on December 7, 2018 (August 2, 2019, August 26, 2018, and December 7, 2018, the summer stratification period and the winter mixing period, respectively, are referred to as the strong stratification period, weak stratification period, and mixing period, respectively.).

Density stratification was more strongly developed on August 2, 2019, than on August 26, 2018, during the summer stratification period because both temperature and salinity stratification were strongly developed. The water temperature stratification was strongly developed because the high solar radiation warmed the surface water temperature, and the salinity stratification was strongly developed because the river inflow from the Kuma River was increased by the high precipitation.

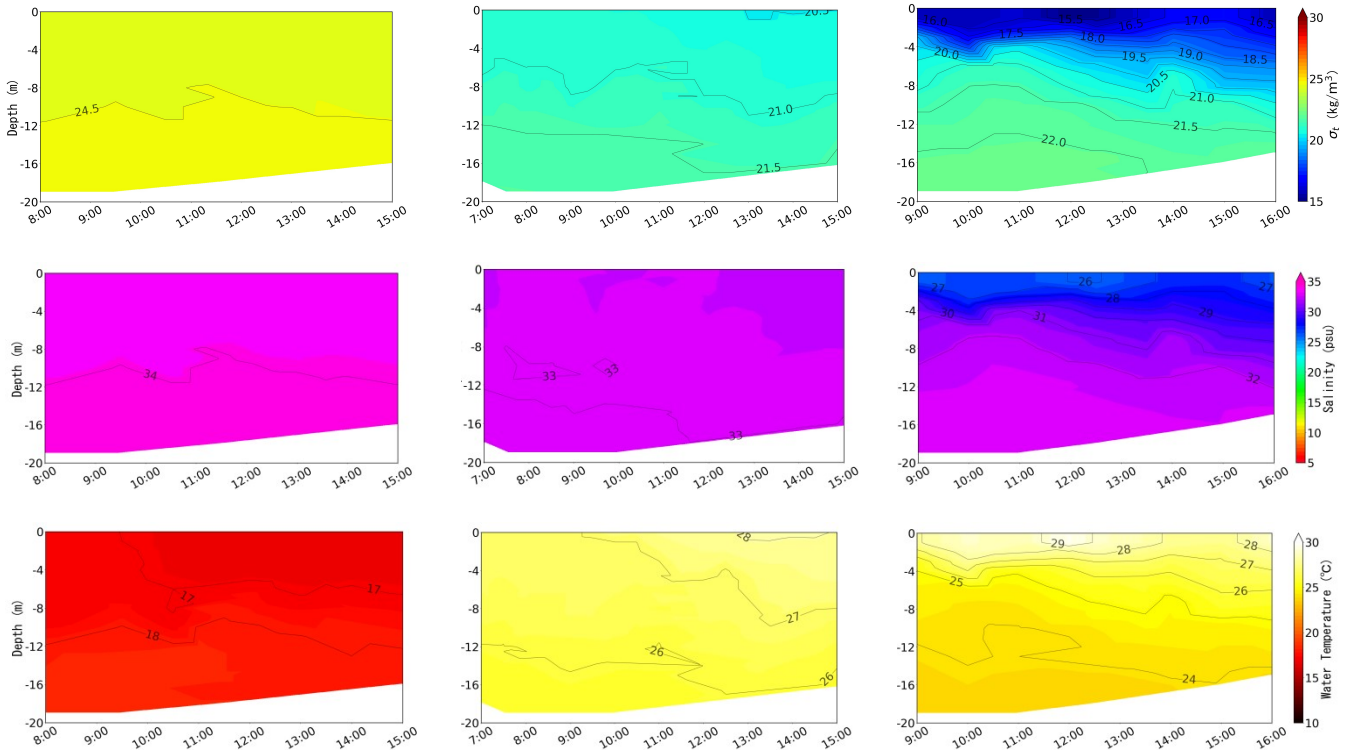

2018/12/07 (Well-mixed period)

2018/08/26 (Weak stratification period)

2019/08/02 (Strong stratification period)

Figure 3.5 Isopleths of σ_t (top), salinity (middle), and water temperature (bottom) for each mixing state at the measurement point ((a, b) in Fig.3.2) located at the estuary of the Kuma River.

3.4.2 Distribution of ΔDIC

Figure 3.6 shows ΔDIC isopleths during the well-mixed period (December 7, 2018), the weak stratification period (August 26, 2018), and the strong stratification period (August 2, 2019). The vertical axis represents the water depth, the horizontal axis represents the time trend, and the color represents the value of ΔDIC. As we can see from (c), tremendous negative ΔDIC values were found near the water surface during the strong stratification period. A negative value of ΔDIC indicates a more significant effect of photosynthesis. In the weak stratification stage, the ΔDIC was uniformly about -120 μmol/kg below the salt leap layer (about 8-12 m depth), while in the mixing stage, it was about -70 μmol/kg. Therefore, it is confirmed that the negatively large ΔDIC is concentrated in the surface layer with the development of stratification.

As we can see from isopleths of ΔDIC ((c) in Fig.3.6) and chlorophyll-a (Fig.3.7) during strong stratification (August 2, 2019), Since chlorophyll-a is an indicator of phytoplankton abundance in water, it was confirmed that phytoplankton was concentrated in the surface layer during the strong stratification period. In addition, extremely negative ΔDIC values were found near the water surface, suggesting that photosynthesis by phytoplankton strongly influences the surface layer during the strong stratification period.

These results suggest that vertical mixing is suppressed as stratification develops and that the effect of photosynthesis by phytoplankton is concentrated in the surface layer.

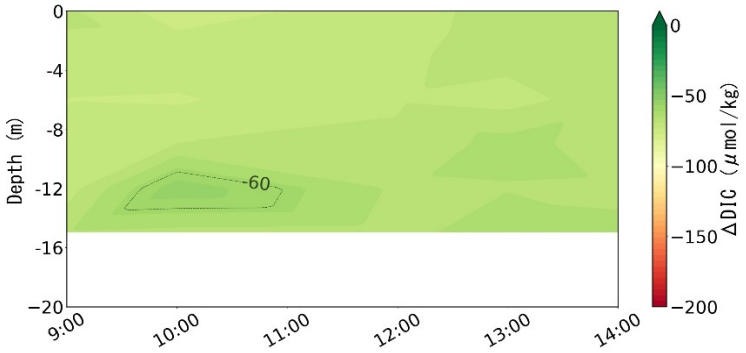

(a) Isopleth of ΔDIC in the well-mixed period (December 7, 2018)

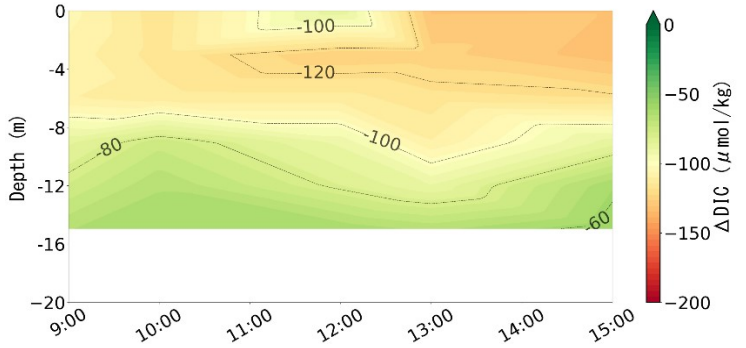

(b) Isopleth of ΔDIC in the weak stratification period (August 26, 2018)

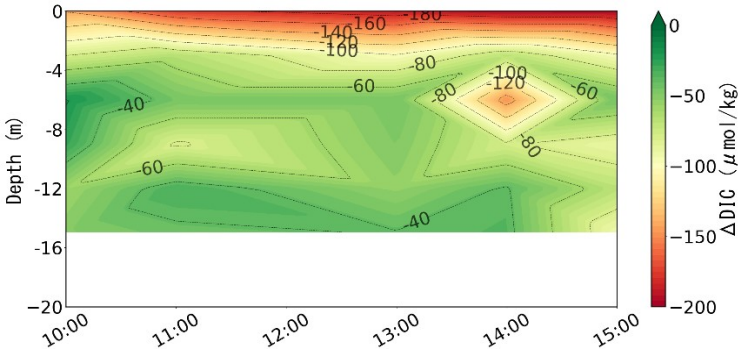

(c) Isopleth of ΔDIC in the strong stratification period (August 2, 2019)

Figure 3.6 Isopleths of ΔDIC for each mixing state at the measurement point.

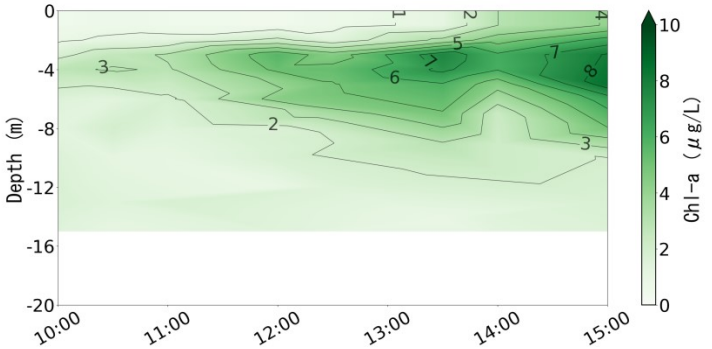

Figure 3.7 Isopleth of Chl-a in the strong stratification period (August 2, 2019).

3.4.3 Distribution of ΔTA

Figure 3.8 shows the isopleths of ΔTA during the well-mixed period (December 7, 2018), the weak stratification period (August 26, 2018), and the strong stratification period (August 2, 2019). The vertical axis represents the water depth, the horizontal axis represents the time trend, and the color represents the value of ΔTA. In the strong stratification period, ΔTA values were different at different depths, but in the weak stratification and mixing periods, ΔTA values were generally around -60 μmol/kg, with no apparent differences in variability.

In this study, the water mass structure was examined using TS-Cluster, a water mass classification software developed by the National Institute of Fisheries Research and Education, to investigate the variation of ΔTA caused by the inflow of water from coral-inhabited areas. Figure 3.9 shows the T-S diagram during the strong stratification period (August 2, 2019). The T-S diagram plots the vertical distribution of water temperature and salinity with water temperature on the vertical axis and salinity on the horizontal axis. Figure 3.9 and (c) in Fig.3.8 show that the distribution of ΔTA generally corresponds to that of water masses during the strong stratification period.

These results indicate that the inflow of coral-influenced water masses into the measurement point may have caused the change in ΔTA.

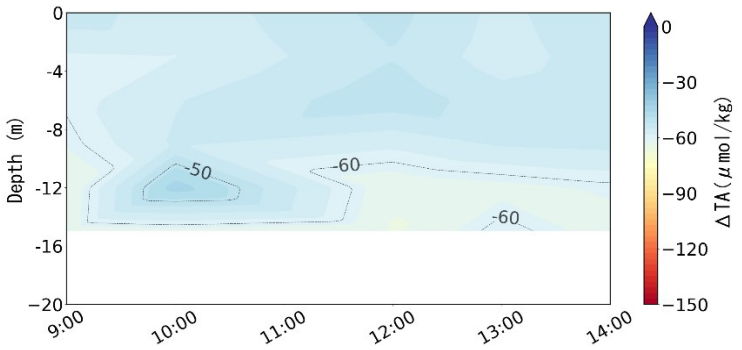

(a) Isopleth of ΔTA in the well-mixed period (December 7, 2018)

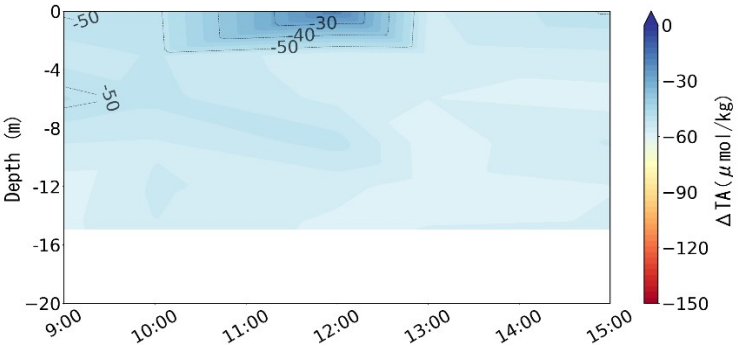

(b) Isopleth of ΔTA in the weak stratification period (August 26, 2018)

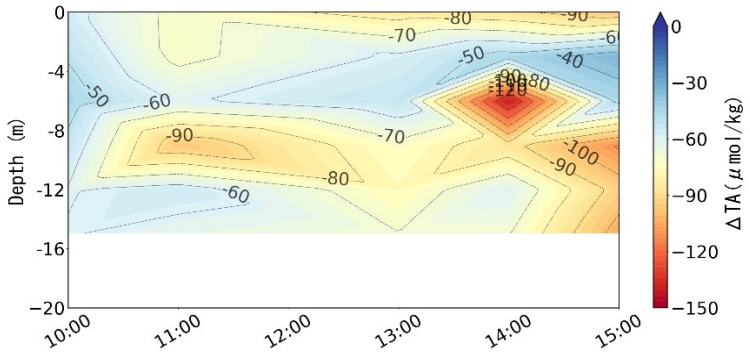

(c) Isopleth of ΔTA in the strong stratification period (August 2, 2019)

Figure 3.8 Isopleths of ΔTA for each mixing state at the measurement point.

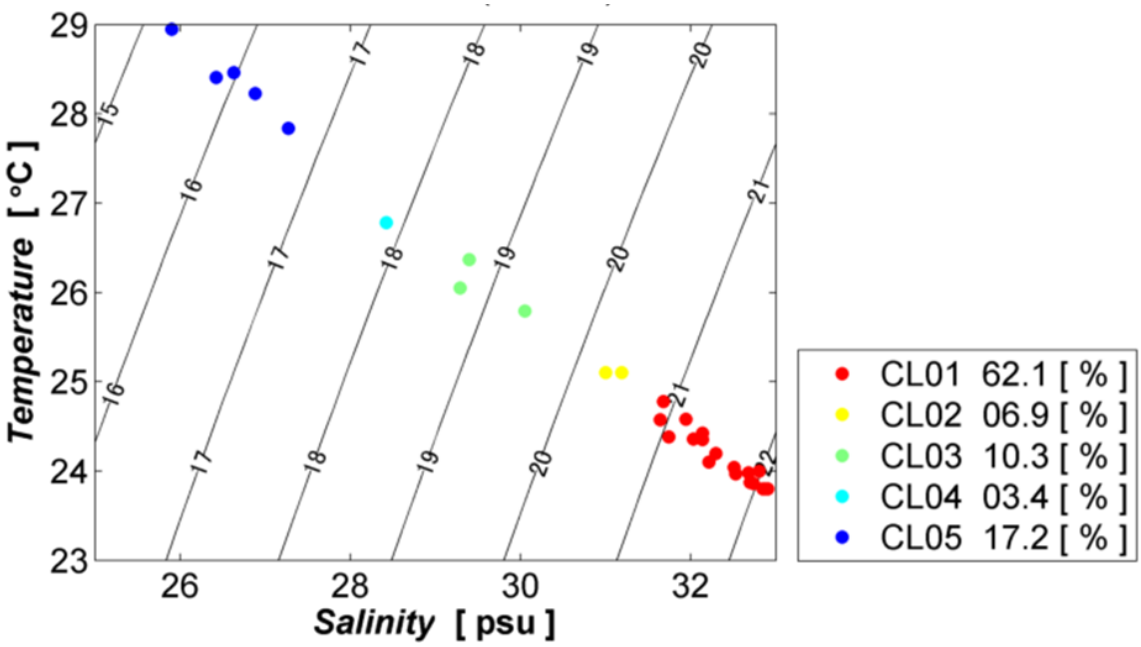

Figure 3.9 T-S diagram during the strong stratification period (August 2, 2019).

Note 1) The contour line in the figure shows the σ_t.

Note 2) The legend on the right side shows the cluster number (CL-01 to the maximum number of clusters) and the occurrence rate [%].

3.4.4 Distribution of pCO_2 in seawater and discussion of factors causing fluctuations

Figure 3.10 shows the isopleths of pCO_2 during the well-mixed period (December 7, 2018), the weak stratification period (August 26, 2018), and the strong stratification period (August 2, 2019). The vertical axis indicates the water depth, the horizontal axis indicates the time trend, and the color indicates the value of pCO_2. In the strong stratification period, the seawater CO_2 partial pressure difference between the surface and bottom layers was significant. The difference in CO_2 partial pressure between the surface and bottom layers was larger in the strong stratification period than in the weak stratification period, and the same was true in the weak stratification period. Furthermore, pCO_2 in seawater was uniform throughout the mixing period. As shown in Section 3.4.2, the CO_2 partial pressure in seawater decreased due to the concentration of the effect of photosynthesis by phytoplankton in the surface layer, which suppressed vertical mixing as the stratification developed.

The partial pressure of CO_2 in seawater in the surface layer during both the stratification and well-mixed periods was lower than the partial pressure of CO_2 in the atmosphere of 412 μatm at the measurement point, confirming the absorption of CO_2 from the atmosphere into seawater.

Thus, it was confirmed that the variation of pCO_2 in seawater in the Yatsushiro Sea was affected by photosynthesis and calcification. Section 3.4.2 shows that stratification suppresses vertical mixing and concentrates the effect of photosynthesis by phytoplankton in the surface layer. This phenomenon lowered pCO_2 in seawater in the surface layer and promoted CO_2 absorption from the atmosphere into the sea. In addition, Section 3.4.3 indicates that pCO_2 in seawater may fluctuate due to the inflow of water from coral habitats during strong stratification.

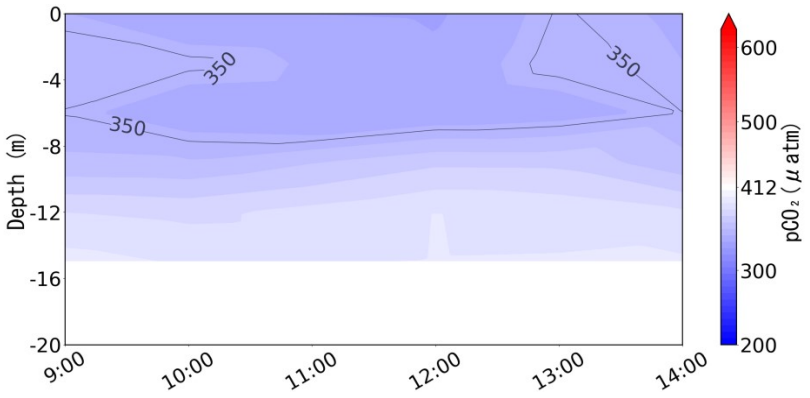

(a) Isopleth of pCO_2 in the well-mixed period (December 7, 2018).

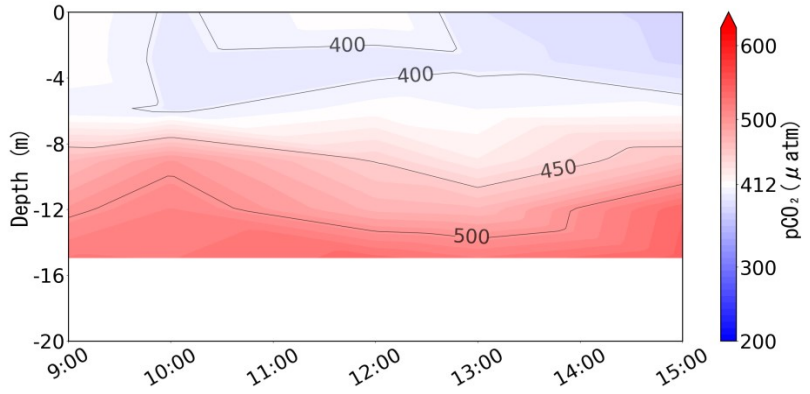

(b) Isopleth of pCO_2 in the weak stratification period (August 26, 2018).

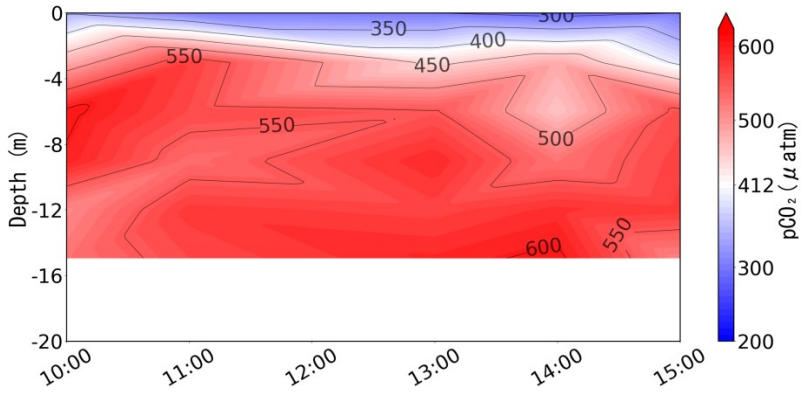

(c) Isopleth of pCO_2 in the strong stratification period (August 2, 2019).

Figure 3.10 Isopleths of pCO_2 for each mixing state at the measurement point.

3.4.5 Effect of each factor on the pCO_2 in seawater

We performed a multi-variable single regression analysis of the measurement results. When two or more variables are used and quantitative data is handled, a scatter plot matrix combining all the variables can be created to grasp the relationships among the data visually.

From Fig.3.11, the correlations among the variables were positive (0.40, 0.26, 0.54) for water temperature, DIC, and ΔDIC, negative (-0.17) for ΔTA, and weak (0.074, 0.022) for salinity and TA, compared to the pCO_2 in seawater. In addition, there was a strong correlation (0.98, 0.95) between salinity, TA, and DIC. Here, TA and DIC are both affected by bicarbonate ions in seawater and can be explained by salinity.

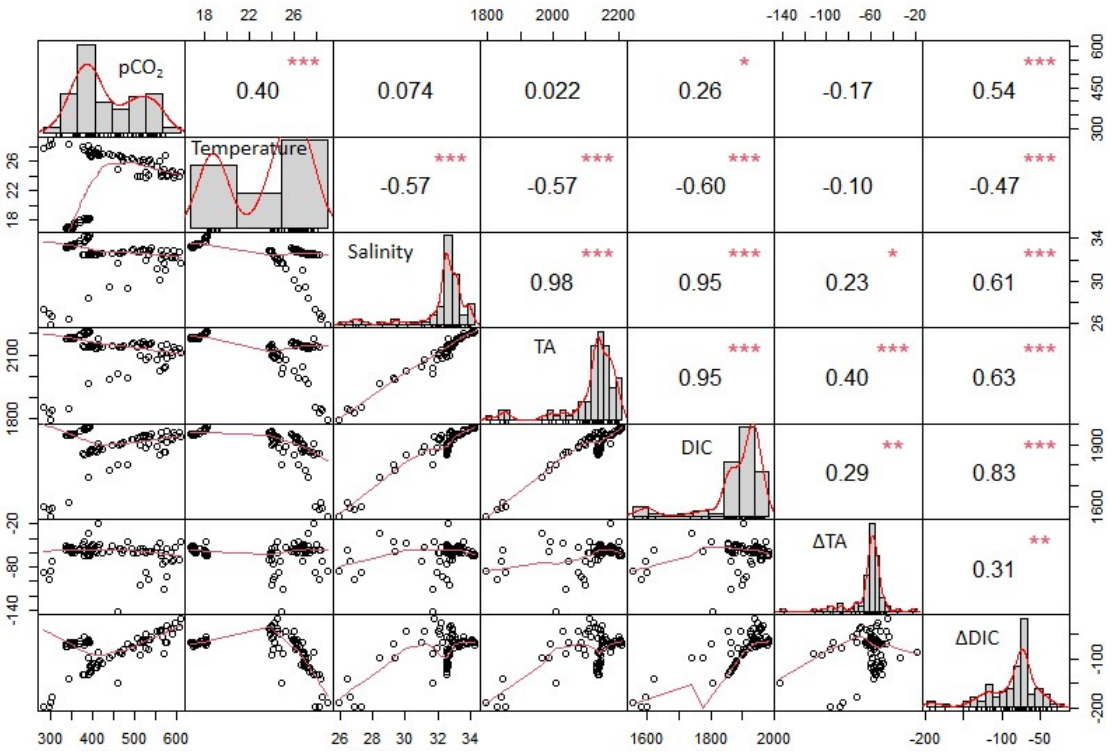

Figure 3.11 Correlation coefficients and paired scatter plots between each variable. Multiple linear regression (Pearson's correlation coefficients and *p*-values) (*$p \leqslant 0.05$, **$p \leqslant 0.01$, ***$p \leqslant 0.001$).

Note 1) The upper triangular matrix shows the single correlation coefficient, the lower triangular matrix shows the paired scatter plot, and the diagonal components show the histogram.

Note 2) The units of each variable are: pCO_2 in seawater (μatm), water temperature (°C), salinity (psu), TA (μmol/kg), DIC (μmol/kg), ΔDIC (μmol/kg), and ΔTA (μmol/kg).

3.5 Conclusions

In this study, we conducted the first field measurements of CO_2 dynamics in the Yatsushiro Sea, and the factors affecting the dynamics of pCO_2 in seawater were analyzed.

We confirmed from the vertical distribution of σ_t that the field measurements were in the mixing period (December 7, 2018), the weakly stratified period (August 26, 2018), and the strongly stratified period (August 2, 2019), respectively. Moreover, the variation of pCO_2 with stratification development was confirmed by comparing pCO_2 distribution at each mixing state.

From the calculation of ΔDIC, it was confirmed that with the development of stratification, vertical mixing was suppressed, and pCO_2 in seawater decreased due to the concentration of photosynthesis by phytoplankton in the surface layer, which promoted CO_2 absorption into seawater. The calculation of ΔTA indicates that pCO_2 in seawater may fluctuate due to the inflow of water from coral habitats during the strong stratification period. These results confirm the effects of photosynthesis and calcification on the variability of seawater pCO_2 in the Yatsushiro Sea.

References

Fujii, T., & Fujiwara, T. (2012). Continuous Measurement of Carbon Dioxide Concentration in the Surface Seawater of Osaka Bay. *Journal of Japan Society of Civil Engineers, Ser. B2 (Coastal Engineering)*, *68*(2), I_1061–I_1065. https://doi.org/10.2208/kaigan.68.I_1061

Fujii, T., Komai, Y., & Fujiwara, T. (2011). Carbon Dioxide Dynamics in Coastal Regions of Osaka Bay. *Journal of Japan Society of Civil Engineers, Ser. B2 (Coastal Engineering)*, *67*(2), I_911--I_915. https://doi.org/10.2208/kaigan.67.i_911

Lavigne, H., & Gattuso, J. (2010). *seacarb: seawater carbonate chemistry with R*. R package version.

Mcleod, E., Chmura, G. L., Bouillon, S., Salm, R., Björk, M., Duarte, C. M., Lovelock, C. E., Schlesinger, W. H., & Silliman, B. R. (2011). A blueprint for blue carbon: toward an improved understanding of the role of vegetated coastal habitats in sequestering CO2. *Frontiers in Ecology and the Environment*, *9*(10), 552–560. https://doi.org/10.1890/110004

Nellemann, C., & Corcoran, E. (2009). *Blue carbon: the role of healthy oceans in binding carbon: a rapid response assessment*. UNEP/Earthprint.

Qu, B., Song, J., Yuan, H., Li, X., & Li, N. (2018). Carbon chemistry in the mainstream of Kuroshio current in eastern Taiwan and its transport of carbon into the east China sea shelf. *Sustainability*, *10*(3), 791.

Tada, K., Nakayama, K., Komai, K., T,sai J. W., Sato, Y., & Kuwae, T. (2018a). ANALYSIS OF DISSOLVED INORGANIC CARBON DUE TO SEAGRASS IN A STRATIFIED FLOW. *Journal of Japan Society of Civil Engineers, Ser. B3 (Ocean Engineering)*, *74*(2), I_444–I_449. https://doi.org/10.2208/jscejoe.74.I_444

Tada, K., Nakayama, K., & Kuwae, T. (2018b). DEVELOPMENT OF CO_2 PARTIAL PRESSURE ECOLOGICAL MODEL IN THE SEAGRASS MEADOW. *Journal of Japan Society of Civil Engineers, Ser. B2 (Coastal Engineering)*, *74*(2), I_1237–I_1242. https://doi.org/10.2208/kaigan.74.I_1237

Tada, K., Tokoro, T., Watanabe, K., Moki, H., & Kuwae, T. (2015). OBSERVATIONS AND STATISTICAL PREDICTIONS OF CO_2 FUGACITY SHALLOW WATERS IN JAPAN. *Journal of Japan Society of Civil Engineers, Ser. B2 (Coastal Engineering)*, *71*(2), I_1333–I_1338. https://doi.org/10.2208/kaigan.71.I_1333

Taguchi, F., Fujiwara, T., Yamada, Y., Fujita, K., & Sugiyama, M. (2009). Alkalinity in Coastal Seas around Japan. *Bulletin on Coastal Oceanography*, *47*(1), 71–75. https://doi.org/10.32142/engankaiyo.47.1_71

Watanabe, K., & Kuwae, T. (2015). How organic carbon derived from multiple sources contributes to carbon sequestration processes in a shallow coastal system? *Global Change Biology*, *21*(7), 2612–2623.

Zeebe, R. E., & Wolf-Gladrow, D. (2001). *CO2 in seawater: equilibrium, kinetics, isotopes* (Issue 65). Gulf Professional Publishing.

Chapter 4
Evaluation of Hydrodynamic Effects on CO_2 Dynamics in the Yatsushiro Sea

4.1 Introduction

As a sink of carbon sequestration and storage, coastal waters are considered to be particularly important (McLeod et al., 2011; Watanabe & Kuwae, 2015). The shallow coastal waters absorb about 45 to 71% of blue carbon (seas from coast to continental shelf (< depth of 200 m)). In mangrove forests, salty wetlands, and seagrass beds located in shallow coastal waters, only 0.05% of the plants are present compared to the existing amount of all land plants, but their annual carbon stock is comparable to the amount of carbon stored in all the terrestrial plants on the earth. Some studies have estimated that the rate of carbon accumulation is higher in coastal sediments (238 Tg C yr^{-1}) than that in open ocean sediments (6 Tg C yr^{-1}) (Nellemann & Corcoran, 2009). Therefore, coastal waters with vegetation such as algae are essential sinks for carbon sequestration and storage.

However, researches on coastal waters are far less than researches on the open ocean. Recently, Europe and the United States began to focus on the study of the dynamics of carbon dioxide in coastal waters (Chen & Borges, 2009). While, as the country with the sixth-longest coastline in the world, Japan has extremely rich coastal resources, which is very important for storing and sequestrating carbon. However, data on carbon dioxide dynamics in coastal waters around Japan are very scarce. In order to predict more accurately and prevent the adverse effects of global warming, it's pretty necessary to understand the dynamics of pCO_2 in seawater in a variety of coastal oceans around Japan.

According to the chemical equilibrium relationship, pCO_2 in seawater is mainly calculated from water temperature, salinity, DIC, and TA (Zeebe & Wolf-Gladrow, 2001). These variables can fluctuate complicatedly on a short time scale. In addition, pCO_2 in seawater varies greatly in time and space due to various factors, such as physical processes like flows of seawater, and mixing of seawater and riverine fresh

water, and biological processes like photosynthesis and respiration of aquatic plants calcification caused by corals.

In order to more accurately understand the dynamic distribution of pCO_2 in the Yatsushiro Sea, we need to investigate the biological processes that affect CO_2 in the Yatsushiro Sea. However, before focusing on the biological processes, we also need to analyze the hydrodynamic effects first.

From the field measurement results of Chapter 3, we find that the ΔTA values are unusually low, especially in the strong stratification period, and we speculate that it is possible that the effect is caused by the inflow of seawater from other sea areas. Since we selected the measurement point near the strait connected with the Ariake Sea, we speculate that it may be due to the inflow of seawater from the Ariake Sea that causes this anomalous value. Even if the value of ΔDIC and ΔTA were calculated by using the Kuma River as one of the end member point, which occupies about 60% catchment area of the whole. We also have to consider the effects of the inflow from the other rivers. For this reason, we will develop a numerical model to evaluate these hydrodynamic effects.

4.2 Comparison of ΔDIC and ΔTA

The comparison between ΔDIC and ΔTA obtained from 2018's measurements and ones from the previous study (Tada et al., 2015) is shown in Table 4.1. As we can see, compared to seagrass meadow, ΔDIC shows similar values, but ΔTA is extremely low. Therefore, we can consider that DIC and TA measured at the measurement point are affected by plants' photosynthesis and the calcification of corals. However, although ΔDIC and ΔTA are calculated by considering the influence of the A-class river Kuma River, which accounts for 60% of the whole catchment area inflow into the Yatsushiro Sea, we still need to evaluate the effects of other smaller rivers. In addition, because the measurement point is located near the strait between the Ariake Sea and the Yatsushiro Sea, the effects of the inflow of seawater from the Ariake Sea on the measured data must be considered as well. Thus, we can consider that the factors affecting DIC and TA at the point are hydrodynamic factors such as the seawater inflow from the Ariake Sea and the freshwater inflow from other small rivers, and biological factors such as the photosynthesis of seagrasss and phytoplankton and the calcification of corals. Next, we developed a numerical model to evaluate the hydrodynamic factor's effects in 2018.

Table 4.1 Comparison between ΔDIC and ΔTA obtained from the measurement and ones from the previous study (Tada et al., 2015).

	Measurement area	Ecosystem type	ΔDIC (μmol/kg)	ΔTA (μmol/kg)
This study	Yatsushiro sea (2018/8/26)	unknown	-118.1±15.0	-57.3±13.3
	Yatsushiro sea (2018/12/7)	unknown	-70.2±2.7	-58.8±2.4
Previous study (Tada et al., 2015)	Furen lagoon	seagrass bed	-62.0±18.7	-29.1±22.6
	Komuke lagoon	seagrass bed	-230.3±85.2	16.7±119.3
	Hashirimizu coast	seagrass bed	-36.5±9.0	9.5±4.9
	Nojima coast	seagrass bed	-311.7±206.2	-1.1±21.9
	Matsuwa mudflat	mudflat	8.9±101.0	44.9±48.8
	Banzu mudflat	mudflat	27.6±15.6	50.3±88.8
	Futtsu mudflat	mudflat	-85.6±108.7	-45.9±27.5
	Fukidogawa estuary	coral reef	17.5±14.9	-111.3±21.9
	Shiraho coast	coral reef	-48.4±177.7	-132.1±113.2

4.3 Hydrodynamic model

4.3.1 Description of Delft3D-FLOW module

Delft3D is an open-source 2D/3D numerical simulation software package developed by WL Delft Hydraulics. The software is a flexible framework for simulating water flow, water quality, waves, ecology, sediment transport in fluvial, estuarine, and coastal environments, and the interactions between the various processes. In this study, the FLOW module in Delft3D was utilized as the modeling tool for developing the hydrodynamic model.

The FLOW module is the core of Delft3D. It is a multi-dimensional (2D or 3D) hydrodynamic (and transport) simulation program that calculates non-steady flow and transport phenomena resulting from tidal and meteorological forcing on a curvilinear, boundary fitted grid, or spherical coordinates. In 3D simulations, the vertical grid is defined following the so-called σ coordinate approach or Z-layer approach. The details of the coordinate system are present in Section 4.3.2.

The mathematical principle of the hydrodynamic model Delft3D-FLOW is mainly to solve the Navier-Stokes equations for incompressible fluids under shallow water assumptions using the finite difference method (Deltares, 2017). Furthermore, the continuity equation and momentum equations are present in Section 4.3.3.

4.3.2 Coordinate system

The horizontal grid applied in the model has a rectangular grid with a Cartesian frame of reference (Deltares, 2017). The vertical grid system is expressed using the σ coordinate system. The vertical dimension is divided into a number of σ layers. Instead of having the vertical coordinates following the depth, they are following the bathymetry. By doing so, the number of vertical grid points remains the same throughout the domain no matter how deep the water column is. Therefore, the number of σ layers is the same throughout the domain, but their thickness varies depending on the depth. The advantage of this vertical coordinate system is that it gives a smooth representation of the bottom topography (Deltares, 2017). The σ coordinate system is defined as below:

$$\sigma = \frac{z - \zeta}{d + \zeta} = \frac{z - \zeta}{H} \tag{4-1}$$

where z is the vertical coordinate in physical space, ζ is the water level above the reference plane at z=0 (m), and d is the depth below the reference plane (m). H is the total water depth (m) and is given by:

$$H = d + \zeta \tag{4-2}$$

The values of σ are at the free surface σ = 0 and at the bottom σ = -1 (Deltares, 2017). The number of layers, as well as their thickness, is at first determined in Delft3D-FLOW. In the coupling process, the number of sigma layers may be redefined. Usually, the hydrodynamic modeling requires a more detailed grid than that of the water quality model; therefore, the number of layers may be reduced in order to reduce the computational time (Deltares, 2017).

4.3.3 Equations

(1) Continuity equation

$$\frac{\partial \varsigma}{\partial \mathrm{t}}+\frac{1}{\sqrt{G_{\xi\xi}}\sqrt{G_{\eta\eta}}}\frac{\partial\left[(d+\varsigma)u\sqrt{G_{\xi\xi}}\right]}{\partial\xi}+\frac{1}{\sqrt{G_{\xi\xi}}\sqrt{G_{\eta\eta}}}\frac{\partial\left[(d+\varsigma)v\sqrt{G_{\eta\eta}}\right]}{\partial\xi}=Q \qquad (4\text{-}3)$$

where ς is related to the reference surface, it is the water depth on this reference surface, t is the time step, d denotes the water column's depth under the reference surface, the coefficient in ξ direction, $\sqrt{G_{\eta\eta}}$ is the variation coefficient in η direction, u and v is the average flow speed in ξ and η direction, Q is the flow variation value because of the all complex impact.

And Q is defined by:

$$Q=H\int_{-1}^{0}(q_{in}-q_{out})d\sigma+P-E \qquad (4\text{-}4)$$

where q_{in} and q_{out} are the flow input and output in unit time (1/s), P is the amount of precipitation (m/s), E is the evaporation capacity (m/s).

(2) Momentum equations

ξ direction：

$$\frac{\partial u}{\partial t}+\frac{u}{\sqrt{G_{\xi\xi}}}\frac{\partial u}{\partial\xi}+\frac{v}{\sqrt{G_{\eta\eta}}}\frac{\partial u}{\partial_{\eta}}+\frac{\omega}{d+\zeta}\frac{\partial u}{\partial\sigma}+\frac{uv}{\sqrt{G_{\xi\xi}}\sqrt{G_{\eta\eta}}}\frac{\partial\sqrt{G_{\xi\xi}}}{\partial\eta}- \qquad (4\text{-}5)$$

$$\frac{v^2}{\sqrt{G_{\xi\xi}}\sqrt{G_{\eta\eta}}}\frac{\partial\sqrt{G_{\eta\eta}}}{\partial\xi}-fv=-\frac{1}{\rho_0\sqrt{G_{\xi\xi}}}P_{\xi}+F_{\xi}+\frac{1}{(d+\zeta)^2}\frac{\partial}{\partial\sigma}\left(v_V\frac{\partial u}{\partial\sigma}\right)+M_{\xi}$$

η direction：

$$\frac{\partial v}{\partial t}+\frac{u}{\sqrt{G_{\xi\xi}}}\frac{\partial v}{\partial \xi}+\frac{v}{\sqrt{G_{\eta\eta}}}\frac{\partial v}{\partial_{\eta}}+\frac{\omega}{d+\zeta}\frac{\partial v}{\partial \sigma}+\frac{uv}{\sqrt{G_{\xi\xi}}\sqrt{G_{\eta\eta}}}\frac{\partial\sqrt{G_{\eta\eta}}}{\partial \xi}-\frac{u^2}{\sqrt{G_{\xi\xi}}\sqrt{G_{\eta\eta}}}\frac{\partial\sqrt{G_{\xi\xi}}}{\partial \eta}$$
$$+fu=-\frac{1}{\rho_0\sqrt{G_{\eta\eta}}}P_{\eta}+F_{\eta}+\frac{1}{(d+\zeta)^2}\frac{\partial}{\partial\sigma}\left(v_V\frac{\partial v}{\partial\sigma}\right)+M_{\eta} \quad (4\text{-}6)$$

where ω denotes the longitudinal velocity in the σ coordinate, f denotes Coriolis force coefficient, $f = 2\Omega sin\varphi$, Ω and φ is the angular velocity, ρ_0 is the water density. Density variations are neglected, except in the baroclinic pressure terms, P_{ξ} and P_{η} represent the pressure gradients. F_{ξ} and F_{η} is the turbulent flow in ξ and η direction, v_V denotes the variation of vertical coefficient of eddy viscosity. M_{ξ} and M_{η} represent the contributions due to external sources or sinks of momentum (external forces by hydraulic structures, discharge or withdrawal of water, wave stresses, etc.).

4.3.4 Set up of hydrodynamic model

In this study, a numerical model using Delft3D-FLOW, a general-purpose three-dimensional coastal flow model developed by Yano et al. (2010), was used for the simulation (Yano et al., 2010). This model combines the Ariake Sea and the Yatsushiro Sea, and its computational domain is shown in Fig.4.1.

A Cartesian coordinate system with a resolution of 10" (Δx = 250m) was used in the horizontal direction, and a σ coordinate system with 10 layers (5% × 3 layers, 10% × 4 layer, and 15% × 3 layers from the surface to the bottom, respectively) was used in the vertical direction. The SGS model evaluated horizontal eddy viscosity and eddy diffusion coefficients, and vertical eddy viscosity and eddy diffusion coefficients were evaluated by the k-ε model and incorporated into the tidal flatness model (ebb and flood model). The calculation time frame is from January 1, 2018, to January 1, 2019, with a time step of 3 minutes.

As shown in Fig.4.1, the open boundary is located on the line connecting Akune, Kagoshima Prefecture, and Kabashima Strait, Nagasaki Prefecture. The amplitudes and slow angles of the main four tides (M2, S2, K1, and O1) were adjusted according to the existing harmonic constants at both ends, and a total of 40 tidal components were obtained. For the adjustment of harmonic constants, we refer to Tai and Yano et al. (Yano et al., 2010).

In this study, freshwater inflows from eight first-class rivers (Chikugo, Yabe, Kase, Rokkaku, Kikuchi, Shirakawa, Midorikawa, and Kuma) and nine major second-class rivers (Kashima, Shioda, Seki, Tsuboi, Hikawa, Otsubo, Sashiki, Yura, and Minamida) were considered. The flow rate of the first-class rivers is the hourly flow rate at the station nearest to the estuary in the non-tidal area obtained from the hydrological water quality database of the Ministry of Land, Infrastructure, Transport and Tourism (MLIT) of Japan. To account for inflow downstream of the station, the flow rate at the station is corrected by multiplying it by a factor calculated by dividing the station's catchment area by the total area of the watershed. For second-class rivers, the calculation is based on the ratio of the catchment area to nearby first-class rivers.

The solar radiation and wind data were obtained from Kumamoto station and

Yatsushiro station of Japan Meteorological Agency (JMA) Amedas, respectively. The sea surface temperature at the open boundary was obtained from the daily sea surface temperature and water temperature data at a depth of 50 m from the Fukuoka Regional Meteorological Observatory.

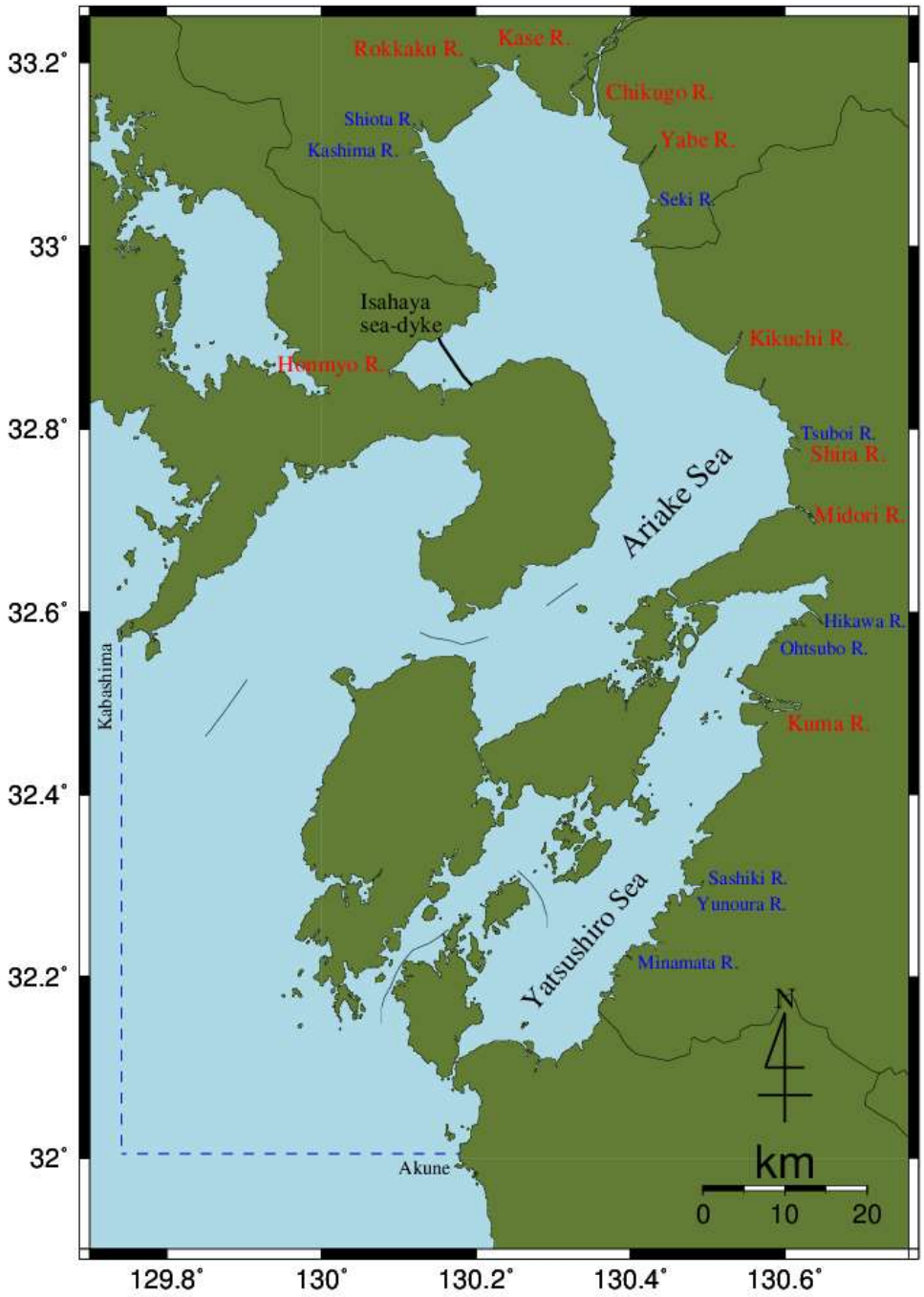

Figure 4.1 Computational domain and open boundaries of hydrodynamic model.

4.4 Particle tracking model

In this study, a particle tracking model to calculate the amount of seawater inflow from the Ariake Sea and freshwater one from small rivers was developed by applying the PART module in Delft3D.

4.4.1 Description of the Delft3D-PART module

The Delft3D-PART module uses a particle tracking approach using data from the FLOW module (2D or 3D) stream to simulate transportation and simple water quality operations. The dynamic concentration distribution can be calculated by monitoring the 3D trajectory through time and estimating the particle mass in the grid cell of the model.

In addition to the random displacement of particles at each time step, these processes are deterministic. Because the simulated behavior is random and the number of particles is limited, the particle tracking approach is based on the random walk method (Rubinstein et al., 2016).

Particle tracking allows for precise spatial models of water quality processes and subgrid concentration distributions to be generated. The Delft3D-PART is best suited for studying the instantaneous or continuous release of the middle range (200 m-15 km), plume simulation (such as oil spill), and simulation of the transport of substances such as salt, bacteria, rhodamine dye, oil, BOD or other conserved or decaying chemicals (following first-order kinetics).

In Delft3D-PART, two modules are available, the Tracer module (simulation of conservative or first-order decaying substances.) and the Oil spill module (simulation of oil spills with floating and dispersed oil fractions). In this study, the Tracer module was applied. In addition, since we are simulating the inflow of water from different regions this time, the effects of vertical and horizontal dispersion are not considered.

4.4.2 Number of particles

The number of particles per release used in the simulation is important for the accuracy of the results. Because of the stochastic nature of the dispersion process, a large number of particles are required to obtain the best results. In general, the precision varies with the square root of the number of particles.

The number of particles required depends on several factors, namely:

1. The length of the simulation.
2. The expected extent of spreading of the particles.
3. The size of the cells in the computational grid.
4. The number of releases.
5. The number of layers used in the vertical direction and the accuracy required over vertical direction.

The precision of the simulation is commonly described as the lowest concentration that a single particle in the cell can represent. The mass of the particle divided by the volume of the cell in which the particle resides is the least concentration level that can be represented by a particle. The formula for determining the number of particles is shown below (Equation 4-7).

$$C_{\min} = \frac{m_{particle}}{A_{cell} \times h_{layer}} = \frac{M_{total}}{N_{total} \times A_{cell} \times h_{layer}} \tag{4-7}$$

where C_{min} denotes the minimum concentration resolution (kg/m^3), $m_{particle}$ denotes the mass per particle (kg), A_{cell} denotes the surface area of the computational cell (m^2), h_{layer} denotes the local layer thickness (m), N_{total} denotes the total number of particles in the release (-), M_{total} denotes the total mass of release (kg).

4.4.3 Set up of particle tracking model

Since this particle tracking model is calculated based on the hydrodynamic model results, the output data from the FLOW module needs to be combined first.

From the process of coupling data from the FLOW module, the dispersion coefficients in the horizontal and vertical directions have been derived. And the simulation time frame was set from July 1st to September 1st, 2018. And the time step of the PART module was set for 1 hour. The number and sizes of the σ layers used in the hydrodynamic simulation remained the same.

In this study, we simulated the influx of the Ariake Sea and the influx of the rivers, respectively. In calculating the amount of the inflow of the Ariake Sea, we set the total number of particles to be 4,480,000 by releasing 20 units instantaneous release at the same time. In calculating the inflow of the river, we set 5 continuous release points corresponding to 5 rivers, including the Kuma River, each of which released a total of 1,000,000 particles. Both of them were using dye release as a substance.

When we calculate the part of the Ariake Sea as Calculation A, we set two instantaneous particle release areas near the strait between two seas, see (a) in Fig.4.2. The radius of them was set by 5,000 meters (top one) and 4,250 meters (bottom one). And we distributed all of the particles into 10 layers for uniform release. The longitudinal thickness of the release we set to 20 m which is closer to the average water depth of the release areas. In order to more easily confirm the final particle concentration flowing into the measurement point, we set the concentration of the release to 1.0 kg/m^3. Considering the effect of tides on seawater exchange, we set four different tidal periods as release start times in July as Case 1 to 4, and compare the results of each. The details of release start times are shown in Table 4.2.

When we calculate the part of rivers as Calculation B, we set 5 continuous releases for each river, including Kuma River, for comparison with other rivers, see (b) in Fig.4.2. Otherwise, the release of Kuma River is divided into two parts in order to correspond to river discharge data. The release of river particles was set for release from layer 1 (surface layer). The radius of release was set for 1 meter. The release rate was set to the measured river flow rate, and the interpolation method uses linear interpolation with a time interval of 2 hours. The concentration of all released

particles was 1.0 kg/m^3.

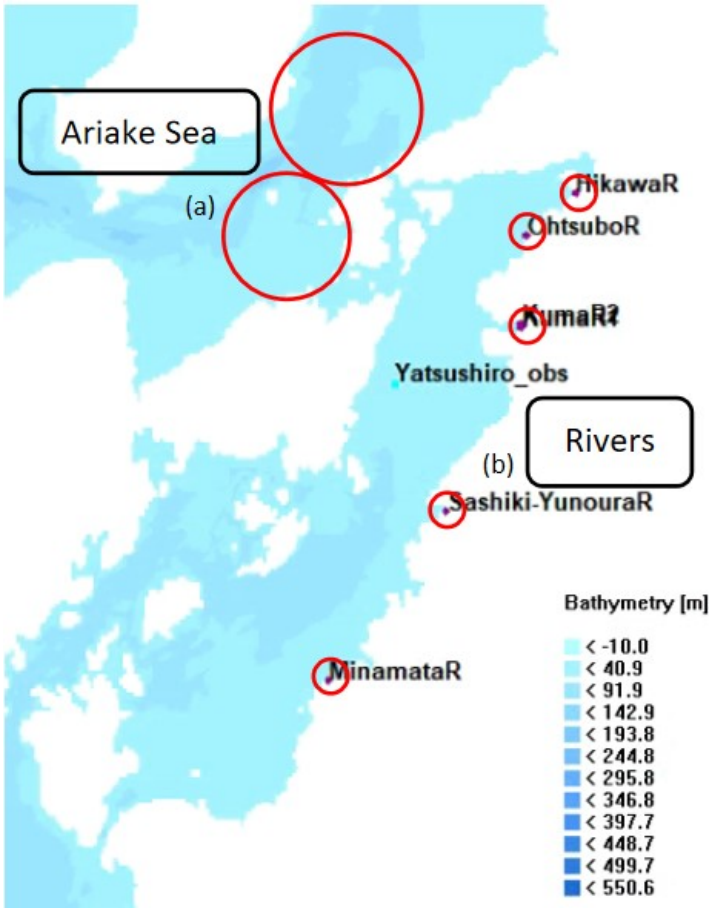

Figure 4.2 Location of releases for particle tracking model.

Table 4.2 Set up time of instantaneous releases

	Period	Tide time	Set up time	Tide level (cm)
Spring tide	High tide (Case 1)	2018/7/14 22:27	2018/7/14 22:00	431
	Low tide (Case 2)	2018/7/14 16:00	2018/7/14 16:00	-7
Neap tide	High tide (Case 3)	2018/7/21 15:46	2018/7/21 16:00	303
	Low tide (Case 4)	2018/7/21 21:43	2018/7/21 22:00	179

4.5 Results and Discussions

In this chapter, the study focuses on the flow of water, so we do not discuss the process of heat transport, salinity transport, etc. The performance of this hydrodynamic model to simulate water flow has been well verified in previous studies, and the verification process is omitted here. The simulated performance of material transport in the water column will be rigorously verified in the later ecological modeling process.

4.5.1 Results and discussions of Calculation A (the Ariake Sea)

Fig.4.3 shows the horizontal distribution of particle concentration for each Case in the surface layer when there was just an inflow of particles at the measurement point (the position is shown in Fig.4.2). We found that particles from the Ariake Sea took about two days to reach our measurement point when it was a high tide period (Case 1 and Case 2) and about three days during a low tide period (Case 3 and Case 4). In addition, in all four cases, most of the particles from the Ariake Sea prefer to exchange with the outer sea through the strait on the left rather than flowing into the Yatsushiro Sea.

Figure 4.4 shows the horizontal distribution of the particle concentrations for each Case in the surface layer when the concentration of particles at the measurement point reached maximum value. From the results, we can see that when the particle concentration at the measurement point gradually reaches the highest value, most of the particles flow out to the outer sea through the strait on the left side of the Ariake Sea. In addition, the area affected by the influx of the Ariake Sea in the Yatsushiro Sea was only near the strait.

We compared the trends of particle concentrations in these 4 cases flowing into our measurement point, and the result is shown in Fig.4.5. We can see that the maximum peak of particle concentration is about 0.021 kg/m^3 on 18th July 2018 8:00 in case of initial release at the low tide of spring tide (Case 2), which means the largest effects of the inflow of seawater from the Ariake Sea can be evaluated as about 2.1% by this simulation.

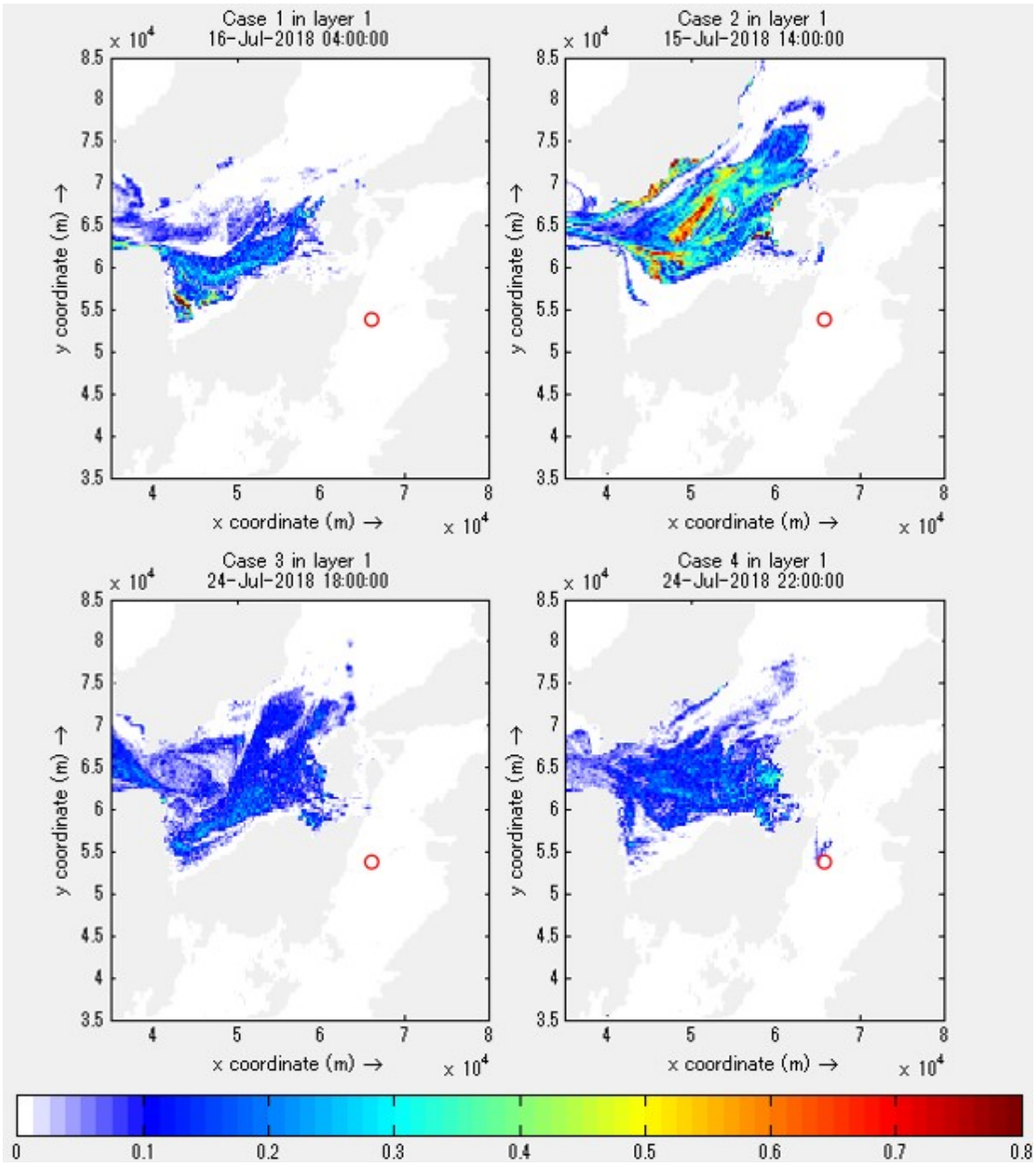

Figure 4.3 Horizontal distribution of particle concentration for each Case in the surface layer when there was just an inflow of particles at the measurement point (red circle).

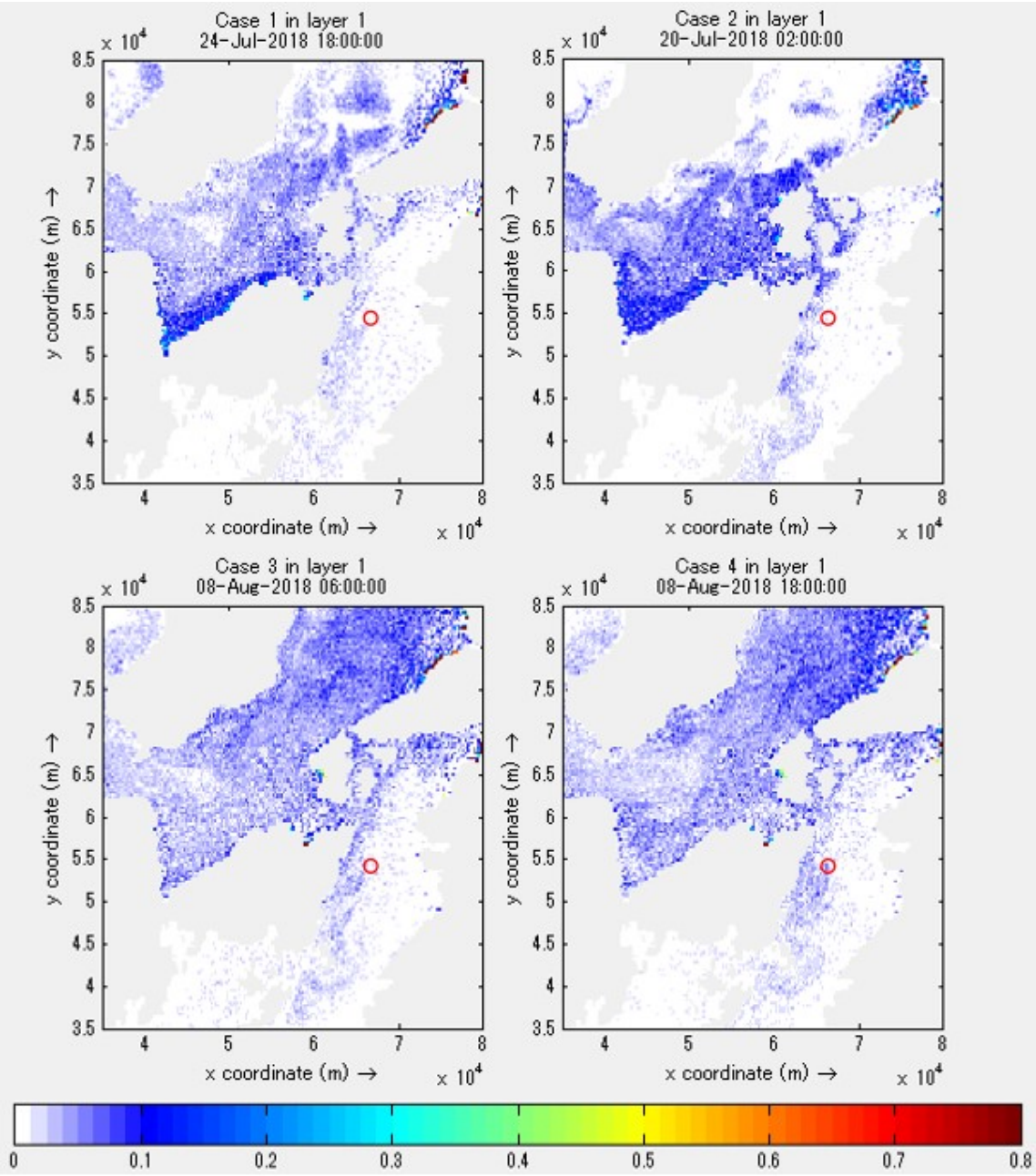

Figure 4.4 Horizontal distribution of the particle concentrations for each Case in the surface layer when the concentration of particles at the measurement point (red circle) reached maximum value.

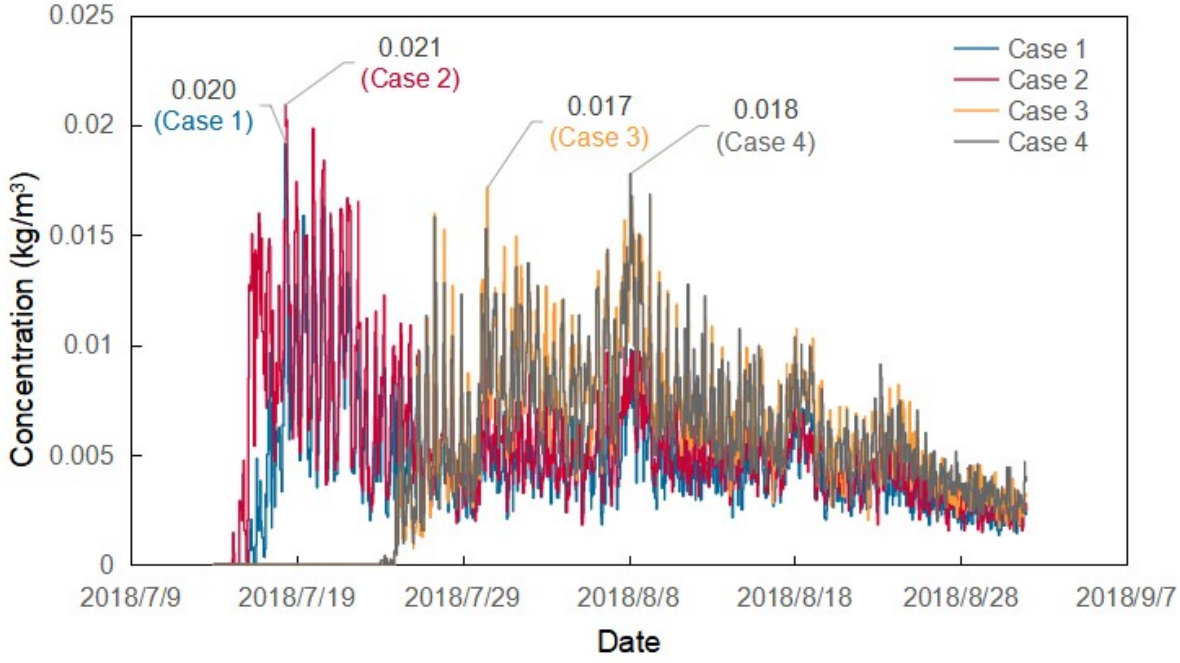

Figure 4.5 Comparison of particle concentrations in four cases.

4.5.2 Results and discussions of Calculation B (the rivers)

In Calculation B, we estimated the effects of the inflow from five rivers, one A-class river (Kuma River), four B-class rivers (Hikawa River, Ohtsubo River, Minamata River, and Sashiki-Yunoura River).

Figures 4.6 and 4.7 show the horizontal distribution of particle concentrations in the surface layer when the particle concentration from the Kuma River and B-class rivers flowing into the measurement point is maximum. The vertical axis and horizontal axis represent the distance from open boundaries, and the color represents the particle concentration.

As we can see from Fig.4.6, the freshwater from the Kuma River can basically affect the entire Yatushiro Sea. And a considerable amount flows into the Ariake Sea through the strait and causes effects. The situations of the four B-class rivers are quite different (Fig.4.7). According to the Hikawa River, which is located in the northernmost part of the Yashitsuro Sea, it has a relatively large flow, resulting in its influence reaching the central part of the Yatsushiro Sea. In addition, it can be seen that there is a considerable amount of volume staying in the strait between the Yatsushiro Sea and the Ariake Sea. As for the other three B-class rivers, due to their low flow rates, basically, the impact area is only in a small radius near their respective estuaries.

We compared the trends of particle concentrations in these five rivers flowing into our measurement point, and the result is shown in Fig.4.8. As we can see that the measurement point area was significantly affected by the freshwater from the Kuma River, and its maximum concentration reaches about 0.728 kg/m^3. And we calculated the ratio of the maximum concentration of B-class rivers to the maximum concentration of the Kuma River, and the result is shown in Table 4.3. We found that the inflow effects of the other rivers are totally accounted for about 3.54% of the value of the Kuma River, which means small enough to be negligible.

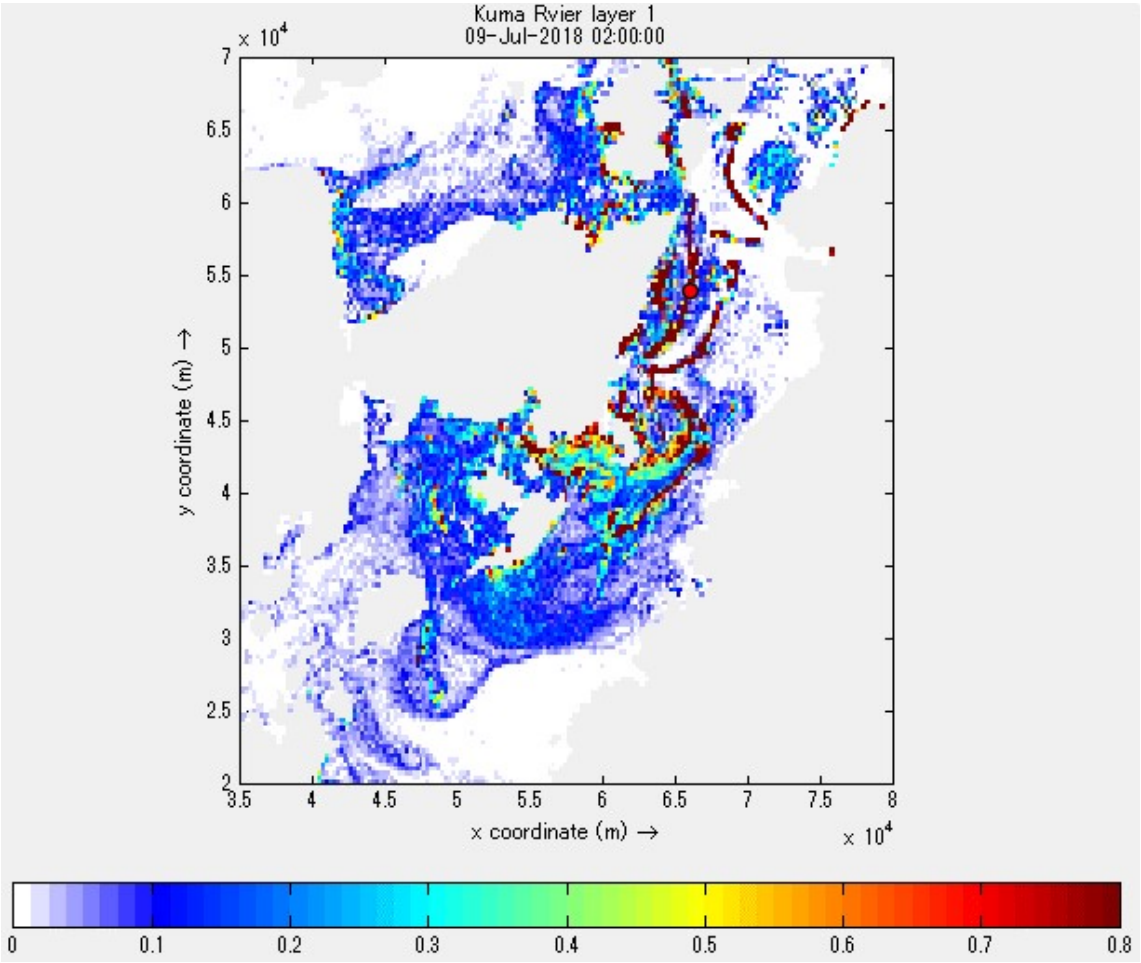

Figure 4.6 Horizontal distribution of particle concentrations in the surface layer when the particle concentration from the Kuma River flowing into the measurement point (red circle) is maximum.

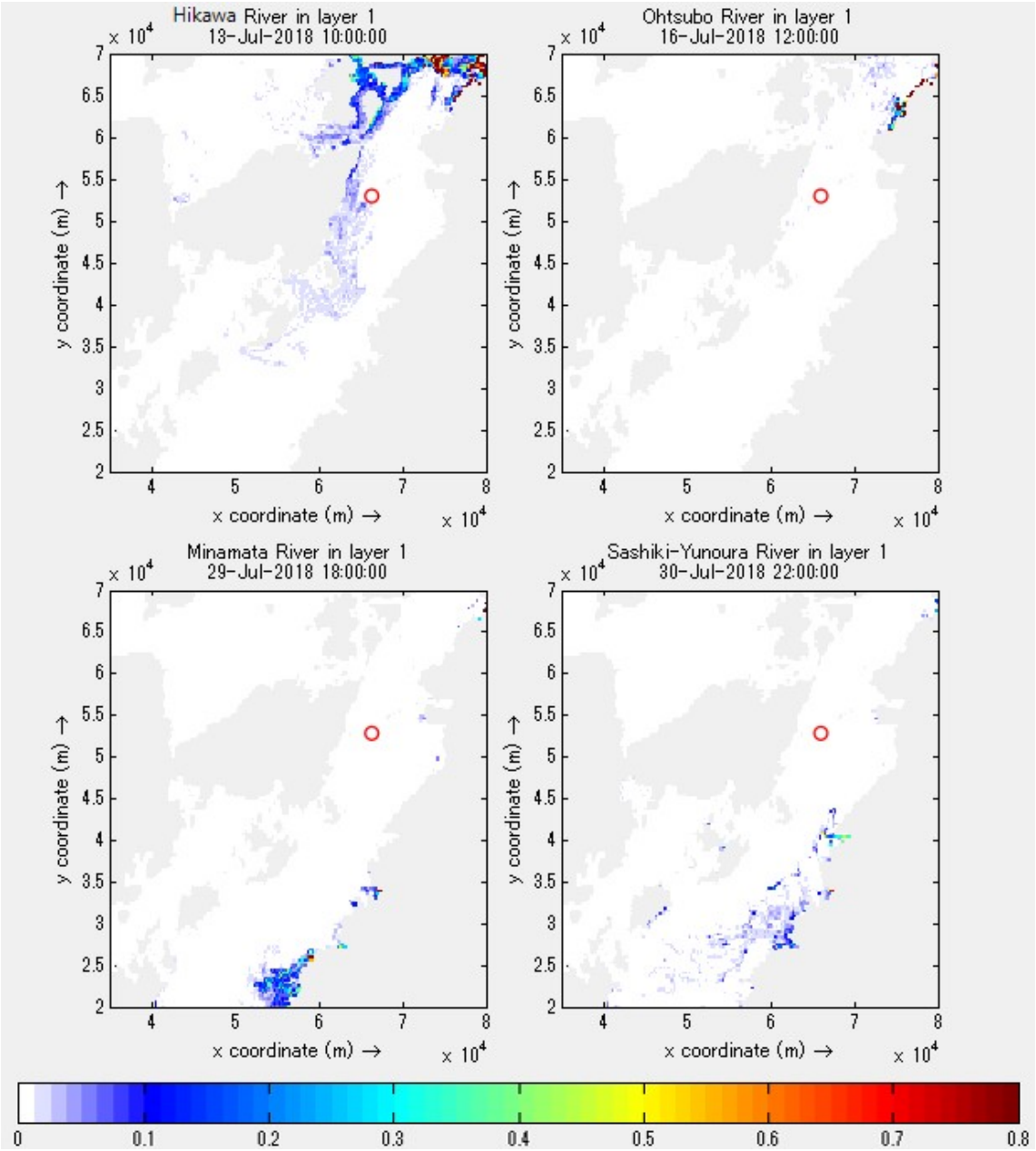

Figure 4.7 Horizontal distribution of particle concentrations in the surface layer when the particle concentration from the B-class rivers flowing into the measurement point (red circle) is maximum.

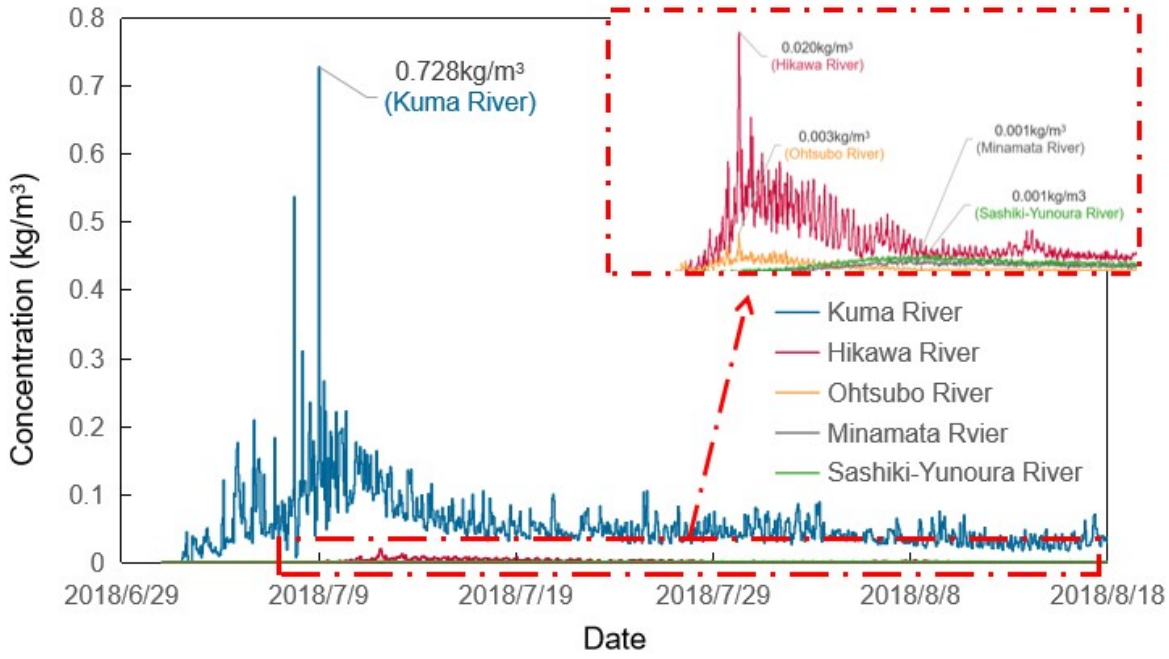

Figure 4.8 Trends of particle concentrations in these five rivers flowing into our measurement point

Table 4.3 Ratio of the maximum concentration of B-class rivers to the maximum concentration of the Kuma River

	Kuma River	**Hikawa River**	**Minamata River**	**Ohtsubo River**	**Sashiki-Yunoura River**	**Total of B-class rivers**
Maximum of particle concentration (kg/m^3)	0.728	0.020	0.001	0.003	0.001	0.026
Ratio to the Kuma River	100%	2.75%	0.14%	0.45%	0.20%	3.54%

4.6 Conclusions

We compared the measured ΔTA values in the Yatushiro Sea with those of previous studies to analyze the factors affecting the CO_2 dynamics in the Yatsushiro Sea, and evaluated the physical effects affecting the CO_2 dynamics in the Yatsushiro Sea by hydrodynamic and particle tracking models. As a result of this study, we found out the followings:

1. The values of ΔTA are extremely low compared to the previous studies, revealing that this region may be affected not only by biological processes but also by the inflow of seawater from other regions or freshwater from other rivers.

2. The maximum effect of the measurement point by the inflow of seawater from the Ariake Sea can be evaluated as about 2.1%, which is negligible.

3. The freshwater inflow affecting the measurement point is mainly from the Kuma River, and the effect of other rivers is small to negligible.

References

Chen, C. T. A., & Borges, A. V. (2009). Reconciling opposing views on carbon cycling in the coastal ocean: Continental shelves as sinks and near-shore ecosystems as sources of atmospheric CO2. *Deep Sea Research Part II: Topical Studies in Oceanography*, *56*(8-10), 578-590.

Deltares. (2017). Delft3D-FLOW users' manual; simulation of multi-dimensional hydrodynamic flows and transport phenomena, including sediments. *Version: 3.15, Deltares, Delft, The Netherlands (2017)*.

McLeod, E., Chmura, G. L., Bouillon, S., Salm, R., Björk, M., Duarte, C. M., Lovelock, C. E., Schlesinger, W. H., & Silliman, B. R. (2011). A blueprint for blue carbon: Toward an improved understanding of the role of vegetated coastal habitats in sequestering CO2. *Frontiers in Ecology and the Environment*, *9*(10), 552-560. https://doi.org/10.1890/110004

Nellemann, C., & Corcoran, E. (2009). *Blue carbon: the role of healthy oceans in binding carbon: a rapid response assessment*. UNEP/Earthprint.

Rubinstein, R. Y., & Kroese, D. P. (2016). Simulation and the Monte Carlo method (Vol. 10). John Wiley & Sons.

Tada, K., Tokoro, T., Watanabe, K., Moki, H., & Kuwae, T. (2015). OBSERVATIONS AND STATISTICAL PREDICTIONS OF CO_2 FUGACITY SHALLOW WATERS IN JAPAN. *Journal of Japan Society of Civil Engineers, Ser. B2 (Coastal Engineering)*, *71*(2), I_1333-I_1338. https://doi.org/10.2208/kaigan.71.I_1333

Watanabe, K., & Kuwae, T. (2015). How organic carbon derived from multiple sources contributes to carbon sequestration processes in a shallow coastal system? *Global Change Biology*, *21*(7), 2612-2623. https://doi.org/10.1111/gcb.12924

Yano, S., Winterwerp, J. C., Tai, A., & Saita, T. (2010). Numerical Experiments on Features of Nonlinear Tide and Its Influences on Sediment Transport in the Ariake Sea and the Yatsushiro Sea. *Journal of Japan Society of Civil Engineers, Ser. B2 (Coastal Engineering)*, *66*(1), 341-345. https://doi.org/10.2208/kaigan.66.341

Zeebe, R. E., & Wolf-Gladrow, D. (2001). *CO2 in seawater: equilibrium, kinetics, isotopes* (Issue 65). Gulf Professional Publishing.

Chapter 5
Numerical Modeling of Seawater CO_2 Dynamics Considering the Influence of Fresh Water Inflow in the Yatsushiro Sea

5.1 Introduction

Field measurements are frequently regarded as one of the most efficient approaches for determining biogeochemical distribution and dynamics in seawater. in order to improve the accuracy of the estimation of coastal CO_2 absorption. In our Chapter 3 study, we implemented field measurements of CO_2 dynamics in several different stratification states in the Yatsushiro Sea, and we need more data in order to get a more comprehensive picture of the characteristics and states of CO_2 dynamics in the bay. However, it is very difficult to obtain long term and wide scale seawater CO_2 data through field measurement. For this situation, numerical simulation is an effective method to complement field measurements data for further analysis.

In this study, we are going to develop a 3D numerical hydrodynamic-ecological coupled model that can simulate the pCO_2 dynamics in different stratification states. Furthermore, we attempted to characterize the Spatio-temporal variability of CO_2 uptake after water discharge using the developed model.

In this study, the FLOW and WAQ modules in Delft3D (version 4.04.01) were utilized as the modeling tools. This framework has been effectively implemented to simulate ocean circulation, stratification, and water quality in various coastal waters (Alosairi & Alsulaiman, 2019; Niu et al., 2016). And there are several successful cases for simulating the CO_2 cycle in surface water by applying the Delft3D-WAQ module (Chen et al., 2019; Menshutkin et al., 2014).

5.2 Hydrodynamic model

In this study, the hydrodynamic model was set up based on the model used in Chapter 4 to further optimize its performance in the vertical direction. The improvement is made by further refining the σ coordinate system in the vertical direction into 17 layers (2% × 10 layers, 5% × 1 layer, 10% × 3 layers, and 15% × 3 layers from the surface to the bottom, respectively), and then calibrating the background eddy coefficients of the model based on the measured values of salinity, water temperature and seawater density with the stratification state.

In addition, for the wind data, hourly data recorded by AMeDAS Yatsushiro were used. Wind speeds were converted to sea breeze using Carruthers' conversion factor from surface to offshore wind as cited by Arakawa et al. (2007) (Table 5.1) (Arakawa et al., 2007). Assuming that AMeDAS Yatsushiro is on land with many obstructions, the wind speed ratio between the ground-borne wind and the measured surface wind is 0.3. The wind speed ratio between the ground and sea breezes is 0.6, so the measured wind speed ratio between the ground and sea breezes is 0.6 / 0.3 = 2. In other words, the measured wind speed is multiplied by two to obtain the wind speed of the sea breeze.

Table 5.1 Relationship between measured wind speed *V* and ground impulse wind speed *Vg* by Carruthers (Arakawa et al., 2007).

Location	Wind speed ratio (V/V_g)
Sea	0.60
low island	0.55
The windward side of the coast, near the lowlands	0.50
Coast on leeward side, near low land or sea	0.40
Open land with few obstructions	0.40
City or land with a lot of obstructions.	0.30

5.3 Ecological model

5.3.1 Description of Delft3D-WAQ module

Delft3D-WAQ is a module of the ecological section, which is used to simulate biological processes in water bodies and sediments and various processes of solute transport and transformation. The WAQ module mainly solves the advection-diffusion-reaction equations for each computational grid by combining the results of the FLOW module (e.g., Spatial and temporal distribution of salinity, water temperature, flow rate, and turbulence dispersion coefficient). Therefore, the computational domain, the resolution, the number of layers in the σ-coordinate system, the location of the freshwater inflow, and the flow velocity are the same as in the hydrodynamic model. This ecological module provides a framework for various user-selected substances and processes, allowing for greater freedom in simulating physical, biochemical, and biological processes. It offers the user a wide range of frameworks for choosing the substances and processes to be simulated, giving more flexibility in simulating physical, biochemical, and biological processes (Deltares, 2014, 2018). The structural diagram of the ecological model used in this study is shown in Fig.5.1. Among them, the interaction of phytoplankton dynamics, nutrients cycling, and inorganic carbon cycling in the upper and bottom water column are considered in this model as the key process affecting the objective of this study (i.e., pCO_2 dynamics in the water column).

The model settings of this ecological model were done mainly by referring to the generic ecological model (GEM) setting (Blauw et al., 2009). Considering the wide coverage of this model and the complex physical and biochemical processes in the target waters, we simplified the GEM model by considering only one phytoplankton process (i.e., green algae) and assuming the decomposition rate of dissolved organic matter to be that of the inorganic matter immediately after production. This simplification has been proved to be reliable in previous simulation studies for anoxic states in the Ariake Sea (Hao et al., 2021; Tadokoro & Yano, 2019). Based on the simplified model, we added the processes of DIC, TA, and pH to simulate the CO_2 dynamics in the water column.

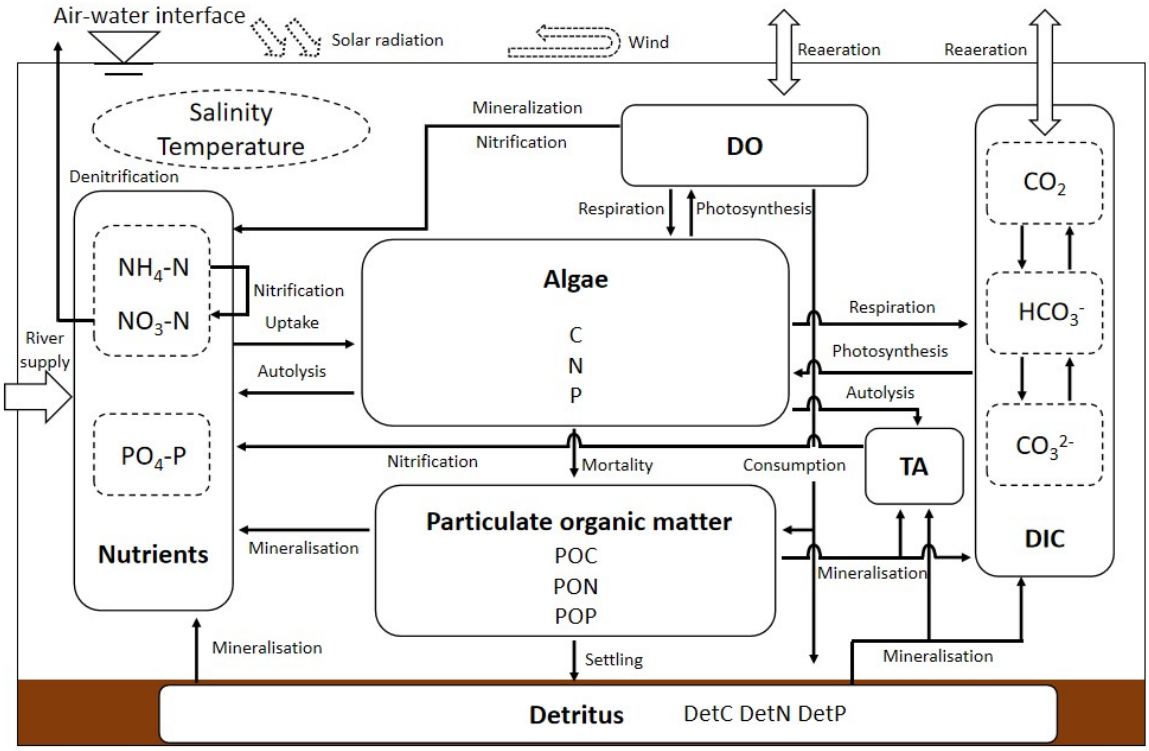

Figure 5.1 Structural diagram of the ecological model.

5.3.2 Mass transport equations

Delft3D solves the mass balance for the different substances by dividing the water system into small boxes, i.e., computational cells. Mass transported from one cell to the next serves as a negative term in the first computational cell and positive in the receiving computational cell. A substance may be converted from one to another within a computation cell, which happens when simulating a water quality process.

By solving the mass balances of each selected state variable, Delft3D-WAQ computes the transport and physical (bio)chemical and biological processes. The first one, transport, includes advective and dispersive transport—the transport by flowing water and the carrier resulting from concentration difference, respectively. Dispersion is calculated according to Fick's diffusion law (Deltares, 2014). The advective-dispersion equation in the x-, y- and z-direction is described below：

$$\frac{\partial C}{\partial t}+u\frac{\partial C}{\partial x}+v\frac{\partial C}{\partial y}+w\frac{\partial C}{\partial z}-\frac{\partial}{\partial x}(D_x\frac{\partial C}{\partial x})-\frac{\partial}{\partial y}(D_y\frac{\partial C}{\partial y})-\frac{\partial}{\partial z}(D_z\frac{\partial C}{\partial z})=0 \qquad (5\text{-}1)$$

where C denotes the concentration of the state variable (g/m^3), u, v, w is the velocity components (m/s), D_x, D_y, D_z denote the dispersion coefficient (m^2/s), x, y, z are the spatial coordinates (m) and t means time (s) (Deltares, 2018). The flow velocities and dispersion coefficients in the horizontal and vertical direction originate from the hydrodynamic results from Delft3D-FLOW, which uses a turbulence model to calculate the vertical velocities.

To incorporate the physical, (bio)chemical, and biological processes, as well as incoming river loads, two additional terms are added to the advective-dispersion equation. Hence, the equation may be called the advective-dispersion-reaction equation and is written accordingly:

$$\frac{\partial C}{\partial t}+u\frac{\partial C}{\partial x}+v\frac{\partial C}{\partial y}+w\frac{\partial C}{\partial z}-\frac{\partial}{\partial x}(D_x\frac{\partial C}{\partial x})-\frac{\partial}{\partial y}(D_y\frac{\partial C}{\partial y})-\frac{\partial}{\partial z}(D_z\frac{\partial C}{\partial z})= S(x,y,z)+P(x,y,z) \qquad (5\text{-}2)$$

where S is the term describing the source of a substance entering the water regime by river discharge and by ocean water from the outer boundary, P denotes the term describing physical, (bio)chemical and biological processes (Deltares, 2014).

There are nine state variables chosen for this ecological model. They are nitrate (NO_3^-), ammonium (NH_4^-), ortho-phosphate (PO_4^-), phytoplankton (ALG), particulate organic carbon (POC), particulate organic nitrogen (PON), particulate organic phosphorus (POP), dissolved oxygen (DO) and dissolved inorganic carbon (DIC). The mass balances for each state variable are given in the equations below:

$$\frac{\Delta ALG}{\Delta t} = B_{gro,C} - B_{mor,C} + q \tag{5-3}$$

$$\frac{\Delta POM}{\Delta t} = B_{mor,M} - B_{dec,M} - B_{set,M} + q \tag{5-4}$$

$$\frac{\Delta NO_3}{\Delta t} = B_{nit} - B_{den} - B_{gro,NO3} + q \tag{5-5}$$

$$\frac{\Delta NH_4}{\Delta t} = B_{dec,N} - B_{nit} - B_{gro,NH4} + B_{aut,N} + B_{mel,N} + q \tag{5-6}$$

$$\frac{\Delta PO_4}{\Delta t} = B_{dec,P} - B_{gro,p} + B_{aut,p} + B_{mel,P} + q \tag{5-7}$$

$$\frac{\Delta O_2}{\Delta t} = B_{rea,O2} + B_{gro,O} - B_{dec,O} - B_{nit} + B_{den} + B_{sod} + q \tag{5-8}$$

$$\frac{\Delta DIC}{\Delta t} = B_{rea,CO2} - B_{gro,C} + B_{dec,C} + q \tag{5-9}$$

where q denotes the load and transport, B represents the physical, (bio)chemical and biological processes. About subscripts of B, *gro*: net algae growth, *res*: respiration, *mor*: mortality, *dec*: decomposition, *set*: settling, *nit*: nitrification, *den*: denitrification, *sod*: sediment oxygen demand, *aut*: autolysis, *rea*: reaeration. The formulation of each state variable is described in the following sections.

5.3.3 Phytoplankton

There are three main processes involved in phytoplankton in Delft3D-WAQ: gross primary production, respiration, and mortality. The difference between gross primary production ($B_{gpp,C}$) minus respiration ($B_{rsp,C}$) is called net primary production and is the rate of biomass accumulation (Equation 5-10). The equations for the other processes are shown in Equations (5-11)~(5-13).

$$B_{gro,C} = B_{gpp,C} - B_{\mathrm{res,C}} \tag{5-10}$$

$$B_{gpp,C} = \left\{\alpha_1 \cdot \beta_1^{(T-20)} \cdot \mu_{\mathrm{nut}} \cdot \mu_{\mathrm{lt}}\right\} \cdot C_{ALG} \tag{5-11}$$

$$B_{rsp,C} = \left\{\alpha_2 \cdot \beta_2^{(T-20)}\right\} \cdot C_{ALG} \tag{5-12}$$

$$B_{mor,C} = \left\{\alpha_3 \cdot \beta_3^{(T-20)}\right\} \cdot C_{ALG} \tag{5-13}$$

where α_1: maximum growth rate at 20°C, β_1: water temperature effect, T: water temperature (°C), μ_{nut}: nutrient limitation of photosynthesis, μ_{lt}: light intensity limitation of photosynthesis, α_2: respiration rate at 20°C, β_2: water temperature effect, α_3: death rate at 20°C, β_3: water temperature effect, C_{ALG}: concentration of phytoplankton.

(1) Gross primary production

Gross primary production is the total amount of energy produced through photosynthesis. By capturing the energy from the sunlight, primary producers can store it in organic compounds by converting carbon dioxide and water into organic compounds (Falkowski & Raven, 2013). The overall chemical formula is written below:

$$CO_2 + 2H_2O + light \longrightarrow (CH_2O) + O_2 + H_2O \tag{5-14}$$

In this model, three factors are chosen to affect the rate of gross primary production, temperature, availability of nutrients, and light.

There are several forms of equations for nutrient limitation, but here we introduce two: one that combines Monod-type expressions and the other that follows Liebig's idea of the law of the minimum.

The expression that combines Monod type expressions:

$$\mu_{nut} = \prod_{i=1}^{n} \left(\frac{C_i}{K_{s,i} + C_i} \right) \tag{5-15}$$

Expression according to Liebig's minimal law (Kizaburo, 1993):

$$\mu_{nut} = \min \left(\frac{C_1}{K_{s,1} + C_1}, \frac{C_2}{K_{s,2} + C_2}, \ldots \right) \tag{5-16}$$

Where $K_{s,i}$ is the half-saturation constant. C_i is the nutrient concentration. While Equation (5-15) is expressed as a product of Monod-type equations, Equation (5-16) expresses each nutrient limitation as a Monod-type equation, and then the one that is the minimum is the nutrient limitation. In general, the latter is more commonly used [e.g., (Yamaguchi & Hayami, 2018; Yokoyama, 1993)]. Therefore, the latter was adopted in this model. Since there are two types of nutrients, N and P, Equation (5-16) can be expressed as follows:

$$\mu_{nut} = \min \left(\frac{C_N}{K_{s,N} + C_N}, \frac{C_P}{K_{s,P} + C_P} \right) \tag{5-17}$$

Dissolved inorganic carbon (DIC) was also regarded as a rate-limiting resource for phytoplankton, as indicated by the availability of CO_2 and bicarbonate (HCO_3^-) for photosynthesis (Verspagen et al., 2014).

Many attempts have been made to approximate the photosynthetic response of phytoplankton to light intensity using appropriate mathematical expressions. The simplest expression is the hyperbolic equation shown below.

$$\mu_{lt} = \frac{I}{1/I_{opt} + I} \tag{5-18}$$

Where I is the light intensity and I_{opt} is the optimal light intensity. However, this equation cannot represent the effect of photosynthesis inhibition under high light conditions. For this reason, Steele (1962) and Kramer-Nixon (1987) proposed the following equation (Nixon et al., 1987; Steele, 1962).

$$\mu_{lt} = \frac{I}{I_{opt}} \exp\left(1 - \frac{I}{I_{opt}}\right) \tag{5-19}$$

The light intensity I in the water column is attenuated by turbidity. This can be described by the Lambert-Beer law.

$$I(z') = I_0 \exp\left(-k_{lt} \cdot z'\right) \tag{5-20}$$

where I_0 is the light intensity at the sea surface, k_{lt} is the dissipation coefficient, and z' is an arbitrary water depth. Substituting this into Equation (5-19), we can obtain the specific photosynthetic rate at any depth.

(2) Respiration

The gross primary production is the total amount of energy produced by the algal cell, but some of this energy is consumed by cellular respiration. Cellular respiration is the process by which energy is extracted through the oxidation of organic carbon to CO_2 and H_2O. Different from photosynthesis, no light is required, and oxygen is consumed. In this model, respiration is performed when the algal cell grows (increasing biomass) and maintains the cell's functions, i.e., the basal metabolism. The respiration associated with cell growth is in direct relation to the gross primary production using a fraction, α_{gr}. The respiration rate necessary to maintaining the cell alive is related to the temperature (Deltares, 2014).

(3) Mortality

In this model, the mortality rate of algae is a function of temperature, where a higher temperature promotes a higher mortality rate. When algae die, a fraction of the biomass is directly released into the water as already dissolved inorganic matter. This process is called autolysis. However, most of the biomass stays intact and continues in the nutrient cycle as detritus, here referred to as particulate organic matter (Deltares, 2014). In reality, the mortality of phytoplankton is also affected by the predation from zooplankton, shells, fish, and other aquatic organisms, by a so-called top-down control (Acha et al., 2015; Valiela & Valiela, 1995). However, the higher level of the food chain is not simulated in this model, and therefore, predation on algae is neglected. By the way, the algal mortality caused by salinity stress is also not considered.

5.3.4 Particle organic matters

Three processes of POM were considered: phytoplankton mortality, decomposition, and settling, as shown in Equation (5-4).

(1) Phytoplankton mortality

In general, when phytoplankton dies, they transform into detritus, which can be distinguished into particle organic matter (POM) and dissolved organic matter (DOM). Blauw et al. (2009) found that the ratio of POM to DOM can be determined by the following equation (Blauw et al., 2009):

$$POM : DOM = 7 : 3 \tag{5-21}$$

This ratio was also adopted in this model. Therefore, B_{mor} and POM are expressed by the following equations.

$$B_{mor,POC} = \left(1 - \alpha_{aut}\right) \cdot B_{mor,C} \tag{5-22}$$

$$B_{mor,PON} = \left(1 - \alpha_{aut}\right) \cdot B_{mor,C} \cdot s_N \tag{5-23}$$

$$B_{mor,POP} = \left(1 - \alpha_{aut}\right) \cdot B_{mor,C} \cdot s_P \tag{5-24}$$

where α_{aut}: ratio of dissolved to suspended solids (=0.3), s_N, s_P: elemental composition *N/C* ratio and *P/C* ratio.

(2) Decomposition

The decomposition of organic matter is mainly due to the activity of bacteria. However, there are few models of bacteria, and most of them assume that the decomposition rate depends on the water temperature. As for the water temperature response of the decomposition rate, the power function type was given as before.

$$B_{dec,M} = \left\{\alpha_4 \cdot \beta_4^{(T-20)}\right\} \cdot C_{POM} \tag{5-25}$$

where β_4: water temperature effect. For α_4, the following equation was used according to (Hydraulics, 2005a).

$$\alpha_4 = k_{decL,M} + f_{dec,nut} \cdot \left(k_{decH,M} - k_{decL,M}\right) \tag{5-26}$$

where $k_{decL,M}$ is the minimum decomposition rate at 20°C and $k_{decH,M}$ is the maximum

decomposition rate at 20°C. The coefficient $f_{dec,nut}$ is given by:

$$f_{dec,nut} = \min\left[\frac{(C_{PON}/C_{POC}) - f_{sL,N}}{f_{sU,N} - f_{sL,N}}, \frac{(C_{POP}/C_{POC}) - f_{sL,P}}{f_{sU,P} - f_{sL,P}}\right] \tag{5-27}$$

where $f_{s,N}$ is a measure of the amount of nitrogen relative to the amount of carbon, and $f_{s,P}$ is a measure of the amount of phosphorus relative to the amount of carbon. The subscripts U and L denote the maximum and minimum, respectively.

(3) Settling

The settling of POM can be modeled by the following equation.

$$B_{set,M} = f_{set} \cdot w_s \cdot \frac{C_{POM}}{D} \tag{5-28}$$

where w_s is the settling rate, D is the water depth, and f_{set} is a coefficient that reflects the effect of bottom shear stress as shown in the following equation.

$$f_{set} = \max\left[0, 1 - \left(\frac{\tau}{\tau_c}\right)\right] \tag{5-29}$$

where τ: base shear stress, τ_c: critical shear stress, and τ is the result of the flow calculation described in Section 4.3 and 5.2.

5.3.5 Inorganic nutrients

The three compartments of inorganic nutrients are ammonium, nitrate, and phosphate. The processes are absorption by phytoplankton, nutrient release during mortality, decomposition of organic matter, and nitrification. The decomposition of organic matter has been explained in the section on POM, so it is not explained in this section.

(1) Absorption by phytoplankton

In order for phytoplankton to proliferate through photosynthesis, nutrients are required. In the model, the nutrient absorption rate was calculated by multiplying the growth rate, which is the difference between the photosynthetic rate and the respiratory rate, by the elemental composition N/C ratio (s_N) and P/C ratio (s_P).

$$B_{gro,NH4} = \left(B_{gro,C} \cdot s_N\right) \cdot f_{uptN} \tag{5-30}$$

$$B_{gro,NO3} = \left(B_{gro,C} \cdot s_N\right) \cdot \left(1 - f_{uptN}\right) \tag{5-31}$$

$$B_{gro,PO4} = B_{gro,C} \cdot s_P \tag{5-32}$$

where f_{uptN}: the total nitrogen content effect of nutrients, modeled by the following equation.

$$f_{uptN} = \begin{cases} \dfrac{C_{NH_4}}{C_{NH_4} + C_{NO_3}} & \left(C_{NH_4} \le C_{c,NH_4}\right) \\ \dfrac{\left\{\left(C_{NH_4} - C_{c,NH_4}\right) + \left(\dfrac{C_{c,NH_4}}{C_{NO_3} + C_{c,NH_4}}\right) \cdot \left(R_{DIN} - C_{NH_4} + C_{c,NH_4}\right)\right\}}{R_{DIN}} & \left(C_{NH_4} - C_{c,NH_4} < R_{DIN}\right) \\ 1 & \left(C_{NH_4} - C_{c,NH_4} \ge R_{DIN}\right) \end{cases} \tag{5-33}$$

$$R_{DIN} = \left(B_{\mathrm{gro},C} \cdot s_N\right) \cdot \Delta t \tag{5-34}$$

where $C_{c,NH4}$ is the limiting ammonium salt concentrations, and Δt is the time step in the numerical calculation.

(2) Nutrient release during mortality

The nutrient release associated with mortality is given by the following equation, which is similar to the one given in the section on POM.

$$B_{aut,M} = \alpha_{aut} \cdot B_{mor,C} \cdot s_M \tag{5-35}$$

(3) Melting

The mechanism of melting from sediment is remarkably complex and depends on physical properties such as the roughness composition and organic deposition of the seafloor, as well as biological and chemical properties such as the population density of benthic organisms, mud temperature and nutrient concentration. Since the benthic environment was not modeled in detail in the present model, it was assumed to depend only on the water temperature T and the concentration of organic matter in the sediment, as in the case of organic matter decomposition, and was given as the melting flux.

$$B_{mel,M} = \left\{\alpha_5 \cdot \beta_5^{(T-20)}\right\} \cdot C_{s,M} \tag{5-36}$$

where α_5: the melting rate at 20°C, β_5: water temperature effect, and $C_{s,M}$: concentration of organic matter in the sediment (M: C, N, P). The concentration of organic matter in the sediment was determined only by the sedimentation of particle organic matter.

(4) Nitrification

Nitrification of ammonium salts is originally decomposed to nitrite and then to nitrate. However, in this model, only the following chemical reaction equation is considered because nitrite is not modeled, and the model is simplified.

$$NH_4^+ + 2O_2 \rightarrow NO_3^- + 2H^+ + H_2O \tag{5-37}$$

The reaction rate of nitrification is related to the activity of nitrifying bacteria, and a form of water temperature response is considered. For this reason, we adopt the following expression, which considers the dependence on water temperature T and dissolved oxygen concentration C_{DO}.

$$B_{nit} = \left\{f_{ox} \cdot \alpha_6 \cdot \beta_6^{(T-20)}\right\} \cdot C_{NH_4} \tag{5-38}$$

where f_{ox}: oxygen concentration effect, α_6: nitrification rate at 20°C, and β_6: water temperature effect. The following equation was given for the coefficient f_{ox}.

$$f_{ox} = \begin{cases} 0 & \left(C_{DO} \le C_{\mathrm{cr},DO}\right) \\ \dfrac{C_{DO} - C_{cr,DO}}{C_{op,DO} - C_{cr,DO}} & \left(C_{cr,DO} < C_{DO} < C_{op,DO}\right) \\ 1 & \left(\mathrm{C_{DO}} \ge C_{op,DO}\right) \end{cases} \tag{5-39}$$

where $C_{cr,DO}$: critical dissolved oxygen concentration in nitrification, $C_{op,DO}$: optimal dissolved oxygen concentration in nitrification.

5.3.6 Dissolved oxygen

There are five processes related to dissolved oxygen (DO): reaeration, photosynthetic production, consumption by decomposition of organic matter, nitrification, and oxygen demand in the bottom sediment. The production by photosynthesis, consumption by decomposition of organic matter, and nitrification are given by the following equations, using the elemental composition O/C ratio (s_O) and O/N ratio (S_{NO}) as shown in the following equation.

$$B_{gro,O} = B_{gro,C} \cdot s_O \tag{5-40}$$

$$B_{dec,O} = B_{dec,C} \cdot s_O \tag{5-41}$$

$$B_{nit,O} = B_{nit} \cdot s_{NO} \tag{5-42}$$

(1) Reaeration of oxygen

The reaeration flux was given by the following equation using the saturated oxygen content.

$$B_{rea,O2} = k_{a,O2} \cdot \frac{C_{DOs} - C_{DO}}{D} \tag{5-43}$$

where $k_{a,O2}$: reaeration coefficient of oxygen, C_{DOs}: saturation oxygen content, and D: water depth.

Strictly speaking, the reaeration coefficient is a function of flow velocity, wind velocity, and water temperature, but many ecological models give a constant value as a representative value. Examples of representative values are 0.15 (day^{-1}), 0.2 (day^{-1}), and 0.6 (day^{-1}).

A number of model equations have been proposed for oxygen saturation, but one model equation introduced in WL/Delft Hydraulics (2005) is presented here. This equation is based on (Fair et al., 1968; Hydraulics, 2005b; Truesdale et al., 1955; Weiss, 1970).

$$C_{DOs} = \left\{a_{sat,O} - b_{sat,O} \cdot T + \left(c_{sat,O} \cdot T\right)^2 - \left(d_{sat,O} \cdot T\right)^3\right\} \cdot \left(1 - \frac{Cl}{m_{sat,O}}\right) \tag{5-44}$$

where $a_{sat,O}$, $b_{sat,O}$, $c_{sat,O}$, $d_{sat,O}$, $m_{sat,O}$: constants, Cl: Chlorine concentration. The values of each constant are shown in Table 5.2. The following equation has been proposed for chlorine concentration to relate it to salinity S (Kono, 2010).

$$Cl = \frac{1.0047154}{1.815069} S \tag{5-45}$$

As shown in Equations (5-42) and (5-43), the amount of saturated oxygen depends on water temperature and salinity. Their relationship is shown in Fig.5.2.

(2) Oxygen demand in sediment

The oxygen demand of bottom sediments is related to various factors such as decomposition of bottom sediments by bacteria, respiration of benthic organisms, and oxidation of nitrogen, but these mechanisms have not been elucidated in detail. In the Ariake Sea, Abe (2003) collected bottom sediment and calculated the oxygen demand rate by laboratory experiments, but the rate was calculated as a constant value due to the limitation of the time of collecting bottom sediment (Abe, 2003). However, in reality, the values vary depending on water temperature and other factors. Therefore, a functional equation affected only by water temperature activity was used in this model.

$$B_{sod} = \left(\frac{B_{sod,0}}{D} + \alpha_7 \cdot \beta_7^{(T-20)} \right) \cdot f_{sod} \tag{5-46}$$

where $B_{sod,0}$: reference oxygen demand rate, α_7: oxygen demand rate at 20°C, β_7: water temperature effect, and D: water depth. The coefficient f_{sod} is given by the following equation.

$$f_{sod} = \begin{cases} 0 & \left(C_{DO} < C_{cr,sod}\right) \\ \dfrac{C_{DO} - C_{cr,sod}}{C_{op,sod} - C_{cr,sod}} & \left(C_{cr,sod} \le C_{DO} \le C_{op,sod}\right) \\ 1 & \left(C_{DO} > C_{op,sod}\right) \end{cases} \tag{5-47}$$

where $C_{cr,sod}$: critical oxygen content for oxygen demand, $C_{op,sod}$: optimal oxygen content for oxygen demand.

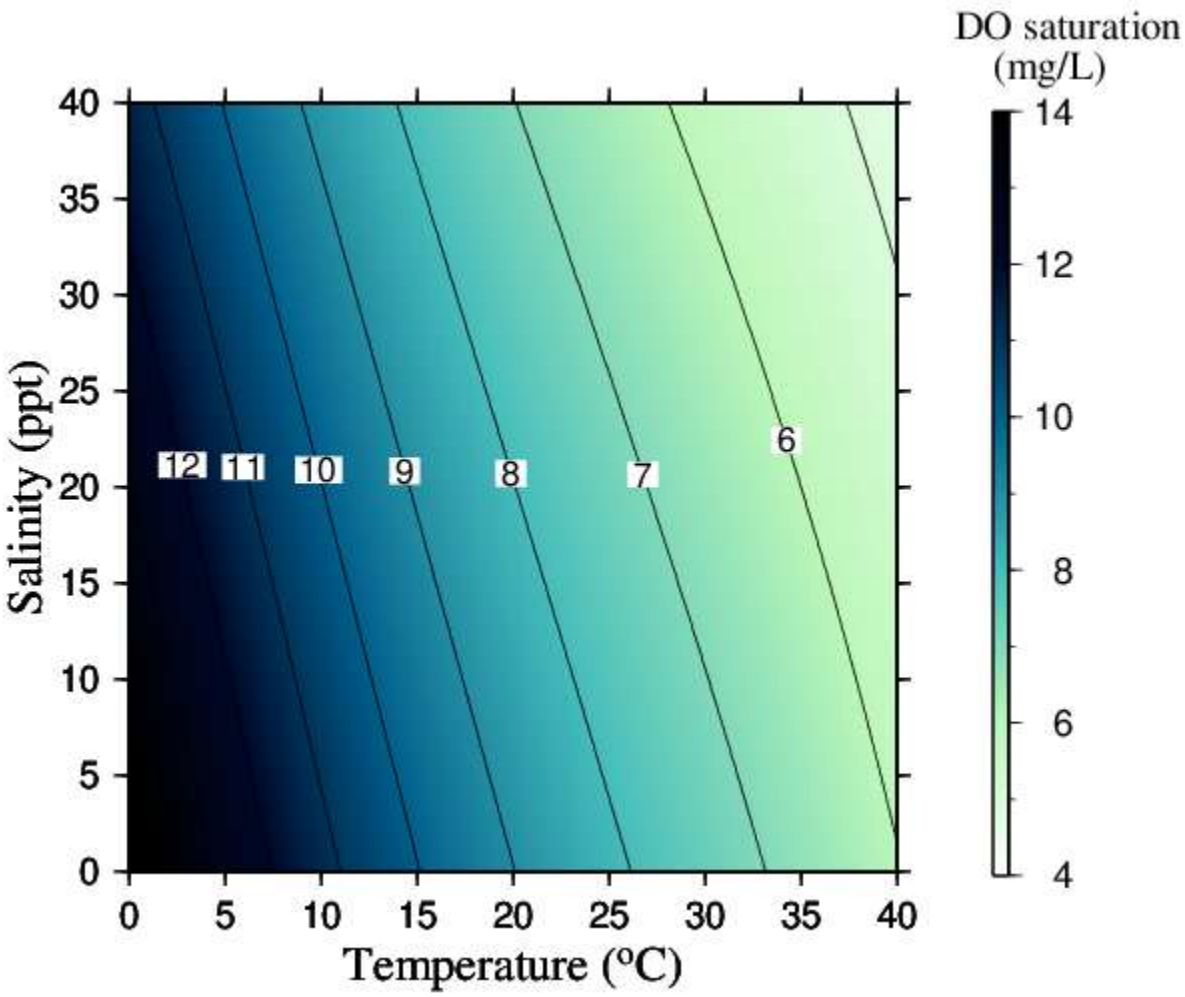

Figure 5.2 Contour of saturated oxygen content by water temperature and salinity.

Table 5.2 Value of each parameter.

Coefficient	Value
$a_{sat,O}$	14.652
$b_{sat,O}$	0.41022
$c_{sat,O}$	0.089392
$d_{sat,O}$	0.042685
$m_{sat,O}$	10^5

5.3.7 Dissolved inorganic carbon

There are four processes related to DIC: reaeration, photosynthetic production, and decomposition of organic matter. The formula of the photosynthetic production, production by respiration, and decomposition of organic matter are shown in Equations (5-11, 5-12, 5-25).

(1) Reaeration of carbon dioxide

CO_2 in surface water tends to be saturated relative to the atmospheric CO_2 concentration. However, CO_2 production and consumption processes in the water column offset the saturation, resulting in either a CO_2-excess or a CO_2-deficit. In addition, the CO_2 concentration depends on the pH:

$$\begin{aligned} &CO_2 + H_2O \Leftrightarrow H_2CO_3 + H_2O \Leftrightarrow \\ &HCO_3^- + H_3O^+ + H_2O \Leftrightarrow CO_3^{2-} + 2H_3O^+ \end{aligned} \tag{5-48}$$

The resulting oversaturation or undersaturation leads to reaeration, i.e., carbon dioxide exchange between the atmosphere and water. The reaction may lead to a flow of CO_2, either to the atmosphere or to the water. The difference between the saturation and the actual CO_2 concentration and the difference in the flow rates of water and upper air can enhance this process. Since the lake is relatively stagnant, only the wind speed is an essential driver for the lake. The reaeration rate tends to saturate at low wind speeds (< 3 m/s). On the other hand, flow velocity may be the main driving force in rivers. Both forces may be important in estuaries.

The reaeration rate is expressed as a linear function of the temperature-dependent mass transfer coefficient in water and the difference between the saturation concentration of CO_2 and the actual concentration, as shown below.

$$B_{rea,CO2} = k_{a,CO2} \cdot \frac{C_{CO2s} - C_{CO2}}{D} \tag{5-49}$$

where $k_{a,CO2}$: reaeration coefficient of carbon dioxide, C_{CO2s}: saturation carbon dioxide concentration, C_{CO2}: actual carbon dioxide concentration, and D: water depth. Similar to the reaeration coefficient of oxygen, $k_{a,CO2}$ is a function of flow velocity, wind velocity, and water temperature, and many ecological models give a constant

value as a representative value. Examples of representative values are 0.5 day^{-1}, and 1 day^{-1}.

Carbon dioxide reaeration is carried out in proportion to the difference between the saturation concentration of carbon dioxide and the actual dissolved carbon dioxide concentration. The saturation concentration of carbon dioxide is mainly a function of the partial pressure of carbon dioxide in the atmosphere, water temperature, and salinity. However, the partial pressure of carbon dioxide in the atmosphere is assumed to be constant.

In Delft3D-WAQ, the calculation of the saturation concentration is performed as a separate process, which has been implemented with two alternative formulas. Weiss (1974) and Stumm and Morgan (1981) describe this calculation (Stumm, 1981; Weiss, 1974). In this study, Weiss's formula is utilized.

$$C_{CO2s} = 44 \times 1000 \times p_{CO2,air} \cdot \exp\left(a_{sat,C} - \frac{b_{sat,C}}{Tf} \cdot + c_{sat,C} \cdot \ln(Tf) + S \cdot (m_{sat,C} + n_{sat,C} \cdot Tf + o_{sat,C} \cdot Tf^2) \right) \quad (5\text{-}50)$$

where $a_{sat,C}$, $b_{sat,C}$, $c_{sat,C}$, $d_{sat,C}$, $m_{sat,C}$, $n_{sat,C}$, $o_{sat,C}$: constants, $pCO_{2,air}$: atmospheric carbon dioxide partial pressure. The values of each constant are shown in Table 5.3. Tf denotes the temperature function, shown below.

$$Tf = \left(\frac{T + 273}{100} \right) \quad (5\text{-}51)$$

Table 5.3 Value of each parameter.

Coefficient	Value
$a_{sat,C}$	-58.0931
$b_{sat,C}$	2385.73
$a_{sat,C}$	0.015264
$d_{sat,C}$	0.28569
$m_{sat,C}$	0.027766
$n_{sat,C}$	-0.025888
$o_{sat,C}$	0.0050578

5.3.8 Summary of each process parameter

In the ecological model, the process parameter were set base on the setting of the DO model by Tadokoro et al. (2019). On this basis, we incorporated processes of DIC, TA and pH to simulate the seawater CO_2 dynamics in the Yatsushiro Sea. The process parameters used in this model is shown in Table 5.4.

Table 5.4 Process parameters of the ecological model.

Description	Symbol	Value	Unit	Reference
State Variables				
Ammonium	C_{NH4}	*	gN/m^3	
Nitrate	C_{NO3}	*	gN/m^3	
Ortho-phosphate	C_{PO4}	*	gP/m^3	
Particulate organic carbon	C_{POC}	*	gC/m^3	
Particulate organic nitrogen	C_{PON}	*	gN/m^3	
Particulate organic phosphorus	C_{POP}	*	gP/m^3	
Particulate organic carbon in sediment	$C_{s,C}$	*	gC/m^2	
Particulate organic nitrogen in sediment	$C_{s,N}$	*	gN/m^2	
Particulate organic phosphorus in sediment	$C_{s,P}$	*	gP/m^2	
Dissolved oxygen concentration	C_{DO}	*	gO_2/m^3	
Dissolved carbon dioxide concentration	C_{CO2}	*	gCO_2/m^3	
Algae biomass	C_{ALG}	*	gC/m^3	
Fluxes				
Net algae growth	B_{gro}	*	$gM/m^3/day$	
Gross primary production	B_{gpp}	*	$gM/m^3/day$	
Algae respiration	B_{rsp}	*	$gM/m^3/day$	
Algae mortality	B_{mor}	*	$gM/m^3/day$	
Decomposition of POM	B_{dec}	*	$gM/m^3/day$	
Settling flux	B_{set}	*	$gM/m^3/day$	
Autolysis of algae mortality	B_{aut}	*	$gM/m^3/day$	
Melting flux	B_{mel}	*	$gM/m^2/day$	
Nitrification	B_{nit}	*	$gM/m^3/day$	
Reaeration of O_2	$B_{rea,O2}$	*	$gO_2/m^3/day$	
Reaeration of CO_2	$B_{rea,CO2}$	*	$gCO_2/m^3/day$	
Sediment oxygen demand	B_{sod}	*	$gO_2/m^3/day$	
Limiting factors				
Nutrient limitation factor for algae growth	μ_{nut}	*	-	
Radiation limitation factor for algae growth	μ_{lt}	*	-	
Nutrient limitation factor for dec. of POM	$f_{dec,nut}$	*	-	
Oxygen limitation factor for nitrification	f_{ox}	*	-	

Table 5.4 Succession.

Description	Symbol	Value	Unit	Reference
Parameters and constants				
Algae				
Potential maximum production rate at 20°C	α_1	1.5	day^{-1}	(D)
Potential maximum respiration rate at 20°C	α_2	0.041	day^{-1}	(Y)
Potential maximum mortality rate at 20°C	α_3	0.2	day^{-1}	(Y)
Temperature factor for primary production	β_1	1.06	-	(Y)
Temperature factor for respiration	β_2	1.07	-	(Y)
Temperature factor for mortality	β_3	1.07	-	(Y)
Half saturation constant for nitrogen for algae growth	$K_{s,N}$	0.005	gN/m^3	(G)
Half saturation constant for phosphorus for algae growth	$K_{s,P}$	0.001	gP/m^3	(G)
Light intensity at water surface	I_0	***	W/m^2	
Optimum light intensity for algae	I_{opt}	96.898	W/m^2	(Y)
Attenuation coefficient	k_{lt}	1.5	m^{-1}	(C)
Particulate organic matter				
Fraction of autolysis	α_{aut}	0.3	-	(B)
Maximum mineralization rate at 20°C of POC	$k_{decH,C}$	0.24	day^{-1}	(C)
Minimum mineralization rate at 20°C of POC	$k_{decL,C}$	0.22	day^{-1}	(C)
Maximum mineralization rate at 20°C of PON	$k_{decH,N}$	0.24	day^{-1}	(C)
Minimum mineralization rate at 20°C of PON	$k_{decL,N}$	0.08	day^{-1}	(B)
Maximum mineralization rate at 20°C of POP	$k_{decH,P}$	0.24	day^{-1}	(C)
Minimum mineralization rate at 20°C of POP	$k_{decL,P}$	0.08	day^{-1}	(B)
Temperature factor for decomposition	β_4	1.047	-	(G)
Upper limit stoichiometric constant PON	$f_{sU,N}$	0.15	gN/gC	(D)
Lower limit stoichiometric constant PON	$f_{sL,N}$	0.1	gN/gC	(D)
Upper limit stoichiometric constant POP	$f_{sU,P}$	0.015	gP/gC	(D)
Lower limit stoichiometric constant POP	$f_{sL,P}$	0.01	gP/gC	(D)
Settling velocity of POM	w_s	0.432	m/day	(Y)
Critical shear stress for POM	τ_c	0.3	N/m^2	(D)
Nutrients				
Fraction of ammonium in nitrogen uptake	f_{uptN}	*	-	
Critical ammonium concentration	$C_{c,NH4}$	0.01	gN/m^3	(D)
N:C ratio in algae biomass	s_N	0.16	gN/gC	(D)
P:C ratio in algae biomass	s_P	0.02	gP/gC	(D)
Potential maximum elution rate at 20°C	α_5	0.03	day^{-1}	(D)
Temperature factor for elution	β_5	1.09	-	(D)
Potential maximum nitrification rate at 20°C	α_6	0.02	day^{-1}	(Y)
Temperature factor for nitrification	β_6	1.03	-	(Y)

Table 5.4 Succession.

Description	Symbol	Value	Unit	Reference
Dissolved oxygen				
Critical concentration of DO for nitrification	$C_{cr,DO}$	1	gO_2/m^3	(D)
Optimal concentration of DO for nitrification	$C_{op,DO}$	5	gO_2/m^3	(D)
O:C ratio in POC	s_O	2.67	gO_2/gC	(D)
O:N ratio in NO_3	s_{NO}	4.571	gO_2/gN	(D)
Reaeration factor of O_2	$K_{a,O2}$	0.7	day^{-1}	(Y)
Saturation dissolved oxygen concentration	C_{DOs}	*	gO_2/m^3	
Chloride concentration	Cl	*	gCl/m^3	
Specified SOD	D_{sod0}	1.5	$gO_2/m^2/day$	(C)
Potential maximum SOD rate at 20°C	α_7	0.5	$gO_2/m^3/day$	(C)
Temperature factor for SOD	β_7	1.07	-	(C)
Critical concentration of DO for SOD	$C_{cr,sod}$	0	gO_2/m^3	(D)
Optimum concentration of DO for SOD	$C_{op,sod}$	0.5	gO_2/m^3	(C)
Dissolved inorganic carbon				
Reaeration factor of CO_2	$K_{a,CO2}$	1	day^{-1}	(C)
Saturation carbon dioxide concentration	C_{CO2s}	*	gCO_2/m^3	
Atmospheric partial pressure of CO_2	pCO_{2air}	***	µatm	
Total alkalinity		*		
Alkalinity	*Alka*	*	$gHCO_3/m^3$	(D)
pH				
Simple calculation of pH	*pH_simp*	*		
Minimum allowed calculated pH	*pH_min*	1	-	(D)
Maximum allowed calculated pH	*pH_max*	14	-	(D)
Physical input data				
Salinity	S	**	ppt	
Water temperature	T	**	°C	
Water depth	D	**	m	
Shear stress	τ	**	N/m^2	

* : Calculated in Delft3D-WAQ

** : Calculated in Delft3D-FLOW

*** : Observation data

(B) : Blauw, *et. al.*(2009)

(C) : Calibrated

(D) : Delft3D-WAQ

(G) : Gurel, *et. al.*(2005)

(Y) : Yamaguchi, *et. al.*(2018)

5.3.9 Formulation of nutrient loading equations for rivers

Measurements of nutrient concentrations in rivers have been conducted only in first-class rivers, but continuous measurements such as water level and flow rate records have not been implemented. Therefore, the L-Q equation, a commonly used equation for estimating water quality parameters, developed a nutrient runoff loading equation for the river.

The target rivers were seven first-class rivers that flow into the Ariake Sea (Rokkaku River, Kase River, Chikugo River, Yabe River, Kikuchi River, Shira River, and Midori River), excluding the Honmyo River, and one first-class river that flows into the Yatsushiro Sea (Kuma River).

Table 5.5 shows the names of the flow rate and water quality monitoring stations in each river targeted in this study, and Fig.5.3 shows the locations of these stations. The flow stations were selected so that the distance between the water quality station and the flow station would be short in any river. The period for which data were used was the entire period for which records were available. The four nutrient items are ammonium form nitrogen (NH4-N), nitrite form nitrogen (NO3-N), orthophosphate form phosphorus (PO4-P), and total organic carbon (TOC). Due to the lack of data on particulate organic carbon (POC), particulate organic nitrogen (PON), and particulate organic phosphorus (POP), which are required for Delft3D-WAQ, the following methods were used to estimate them using TOC.

1. It was assumed that TOC in river water is mostly plant-derived and follows the same laws as algae.

2. As described in Section 5.3.4, when algae die, they are decomposed in the ratio DOM: POM=7:3. Therefore, POC was calculated from TOC, assuming that TOC:DOC: POC=10:7:3 in river water.

3. Based on the Redfield ratio of algae C:N: P=106:16:1, PON and POP were calculated from POC, assuming that POC:PON: POP=106:16:1 in river water.

As an example of the L-Q equation, the result by (Tadokoro & Yano, 2019) is shown in Fig.5.4.

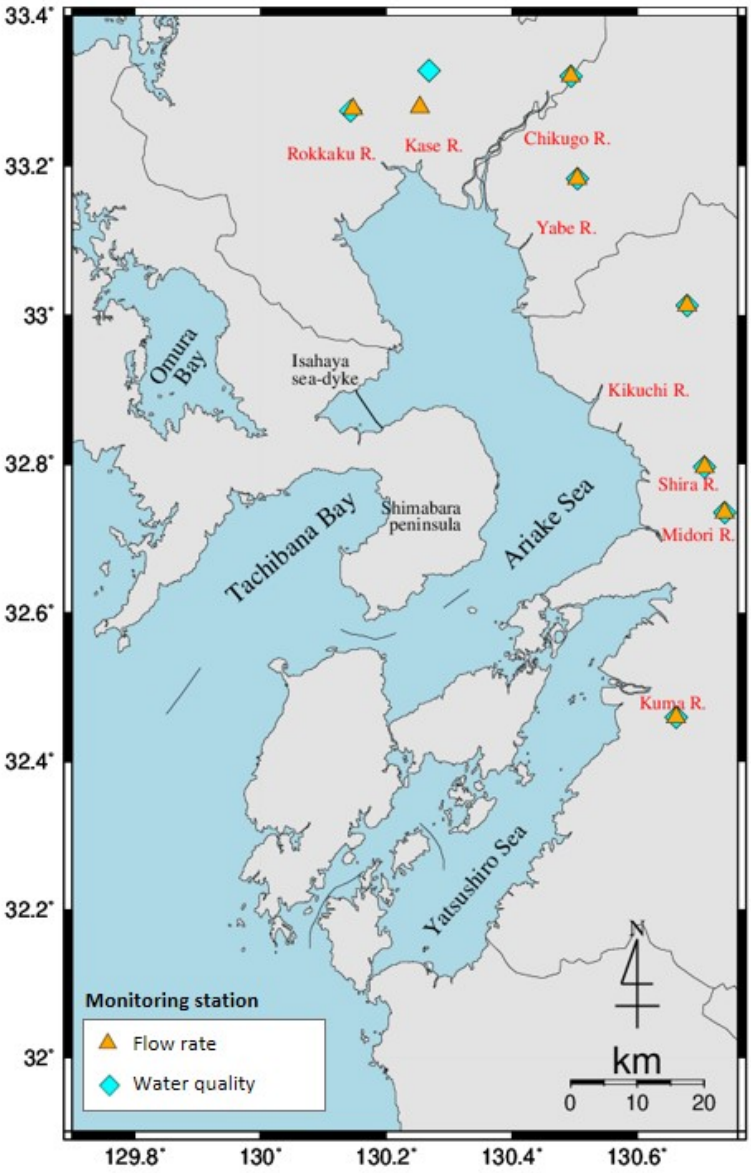

Figure 5.3 Location of the flow rate and water quality monitoring stations.

Table 5.5 Names of flow rate and water quality monitoring stations.

Rivers	Flow rate monitoring stations	Water quality monitoring stations
Chikugo	Senoshita	Senoshita
Yabe	Funagoya	Funagoya
Kase	Ikemori	Kanjinbashi
Rokkaku	Myoukenbashi	Hazamazeki
Kikuchi	Yamaga	Yamaga
Shira	Yotsugibashi	YotsugibasHi
Midori	Jounan	Jounan
Kuma	Yokoishi	Yokoishi

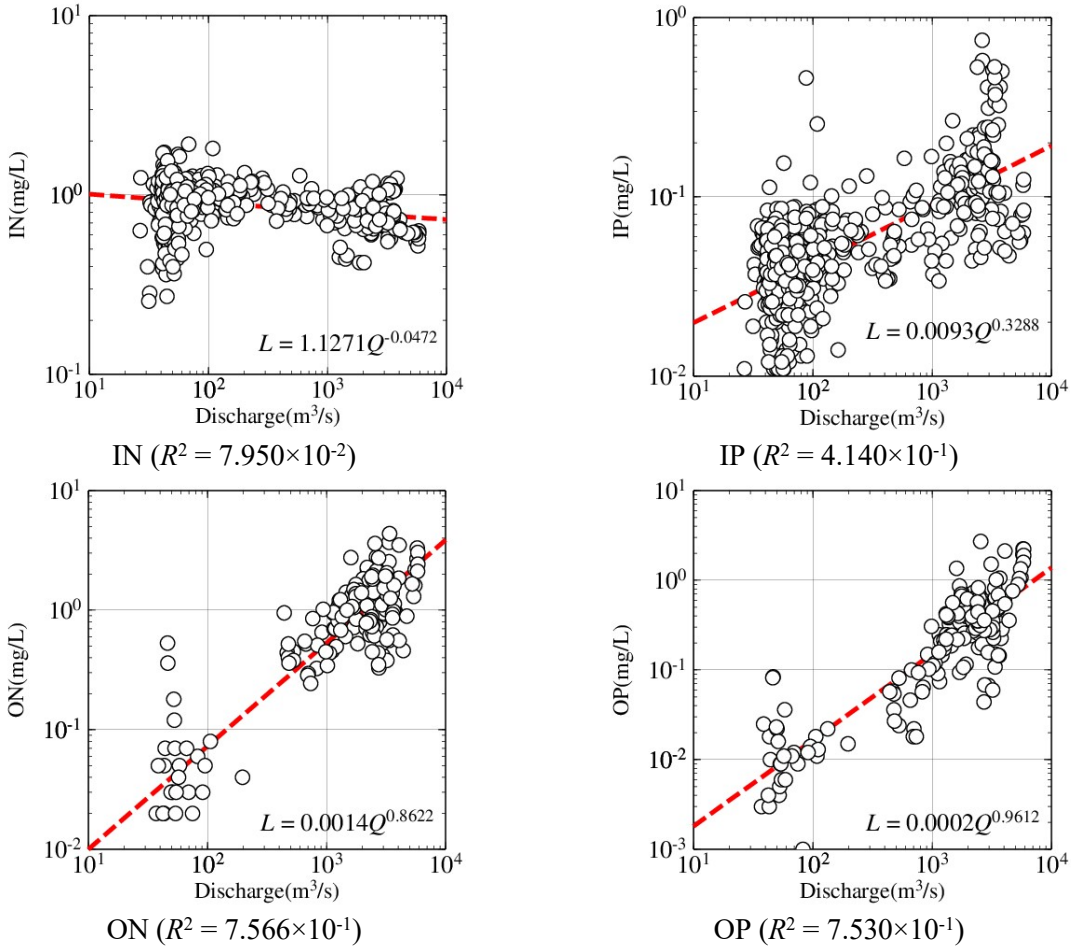

Figure 5.4 Results of L-Q equation by Tadokoro et al. (2019) (Chikugo River).

5.4 Model calibration and verification

We calibrate and verify the hydrodynamic and ecological model parameters for the easily stratified area near the Kuma River estuary using the results of three field measurements of CO_2 dynamics in seawater at different stratification periods implemented at point (a, b) in Fig.3.2. We chose water temperature, salinity, density, DIC, TA, and pCO_2 as objects.

To quantitatively evaluate the model performance, three performance metrics were selected: the root means square error (*RMSE*), the Pearson's correlation coefficient (*r*), the refined Willmott index (d_{ref}) .

A "good" model has a low *RMSE*. Pearson's correlation coefficient *r* was used to evaluate the model performance.

$$RMSE = \sqrt{\sum_{i=1}^{n} \frac{(m_i - o_i)^2}{n}} \tag{5-52}$$

where m_i: simulated values, o_i: measured values, *n*: the number of measurement data.

A value of *r* near 1 shows a good correlation between measurements and simulation, whereas values near 0 suggest weaker and often inconsequential correlations.

$$r = \frac{\sum_{i=1}^{n}(m_i - \overline{m})(o_i - \overline{o})}{\sqrt{\sum_{i=1}^{n}(m_i - \overline{m})^2}\sqrt{\sum_{i=1}^{n}(o_i - \overline{o})^2}} \tag{5-53}$$

where m_i: simulated values, o_i: measured values, $\overline{m}$: mean of simulated values, $\overline{o}$: mean of measured values, *n*: the number of measurement data.

The refined Willmott index d_{ref} is a modeling efficiency index that ranges from -1 to 1. A value that is closer to 1 suggests that the model is performing better.

$$d_{ref} = \begin{cases} 1 - \dfrac{\sum_{i=1}^{n} |m_i - o_i|}{2 \cdot \sum_{i=1}^{n} |o_i - \bar{o}|}, \text{when } \sum_{i=1}^{n} |m_i - o_i| \le 2 \cdot \sum_{i=1}^{n} |o_i - \bar{o}| \\ \dfrac{2 \cdot \sum_{i=1}^{n} |o_i - \bar{o}|}{\sum_{i=1}^{n} |m_i - o_i|} - 1, \text{when } \sum_{i=1}^{n} |m_i - o_i| > 2 \cdot \sum_{i=1}^{n} |o_i - \bar{o}| \end{cases} \quad (5\text{-}54)$$

To verify the model's reproducible performance of the CTD distribution and CO_2 dynamics in seawater in the vertical direction, we also used contour plots to compare the simulation results with measurements.

5.5 Results and Discussions

5.5.1 Model calibration and verification

The results of the three field measurements we implemented at point a were used for calibration and verification of the numerical model simulation results near the estuary of the Kuma River, and the final statistical verification results are displayed in table 5.6. Among them, salinity, σ_t, and water temperature were used for the verification of the hydrodynamic module. There is a strong correlation between the simulated CTD results and the measured values ($r > 0.9$). The highest correlation was found for water temperature ($r > 0.97$), but its RMSE was relatively high, probably since the measurement site is located near the estuary of the Kuma River and is strongly influenced by the freshwater inflow. The river temperature data input to the model is obtained from the prediction of the L-Q equation based on the temperature and flow of the previous years, which has some errors. The RMSE of both σ_t and salinity showed low values (0.95 kg/m^3 and 0.92 psu). The d_{ref} values for each variable indicate that the model has a good performance (> 0.6) for the hydrodynamic simulation of this region. In general, the model's hydrodynamic simulation performance in the Kuma River estuary is in an acceptable range overall, where the performance of the variation trend is better than the numerical fitting performance.

Table 5.6 Summary performance statistics for model verification.

Variable	Units	[1]*r*	[2]*RMSE*	[3]d_{ref}	[4]*n*
Salinity	psu	0.92	0.93	0.60	423
σ_t	kg/m^3	0.95	0.98	0.74	423
Temperature	℃	0.97	1.45	0.85	423
DIC	μmol/kg	0.94	33.10	0.82	89
TA	μmol/kg	0.94	45.79	0.67	89
pCO_2	μatm	0.87	65.56	0.66	89

[1] *r*: Pearson's correlation coefficient.

[2] *RMSE*: root mean square error.

[3] d_{ref}: refined Willmott index.

[4] *n*: number of samples.

For the verification of the ecological model, we chose DIC, TA, and pCO_2 as object variables. Regarding the value of DIC, it has a Pearson correlation value of 0.94, showing a very strong correlation, while the RMSE of 33.10 μmol/kg is at a low

level (1.74%) relative to the mean of the measured DIC (1899.4 μmol/kg). The simulated TA, also shows a very strong correlation for the measured data (r = 0.94), and the ratio of RMSE to the mean of the measured values is at a very low level (2.16%). Whereas the r-value of pCO_2 was lower (0.87) relative to the last two, but again showed a strong correlation, its RMSE value (65.56 μatm) was slightly higher (15%) relative to the ratio of the mean of the measured values, but still in an acceptable range (< 30%). The reason for the large numerical errors in pCO_2 while DIC and TA have good numerical fits is that pCO_2 is calculated based on water temperature, salinity, DIC, and TA, and small errors in each of them are superimposed on the final pCO_2 calculation, resulting in large errors in pCO_2, which is a major challenge for pCO_2 simulation in water bodies. Overall, the ecological model has a relatively good performance in simulating the CO_2 dynamics in the Kuma River estuary region, as shown by the d_{ref} values (> 0.6) of DIC, TA, and pCO_2.

In addition, we visualized the contour plots of the measured and simulated results separately, where the variables output from the hydrodynamic model (i.e., salinity, σ_t, and water temperature) are shown in Fig.5.5-5.7, while the output of the variables from the ecological model (i.e., DIC, TA, and pCO_2) are shown in Fig.5.8-5.10.

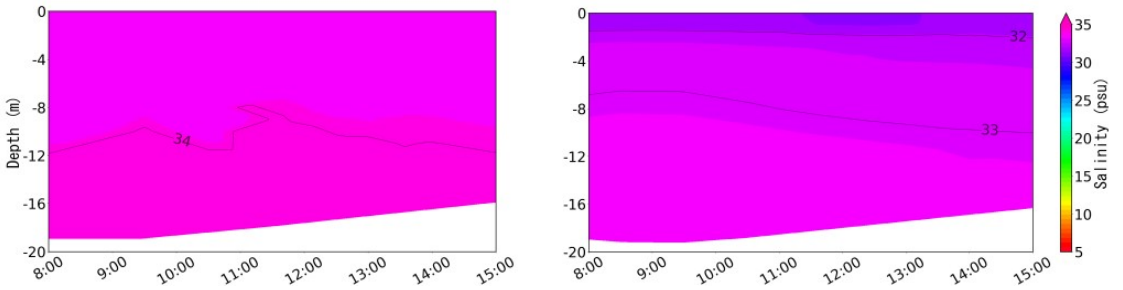

2018/12/07 (Well-mixed period)

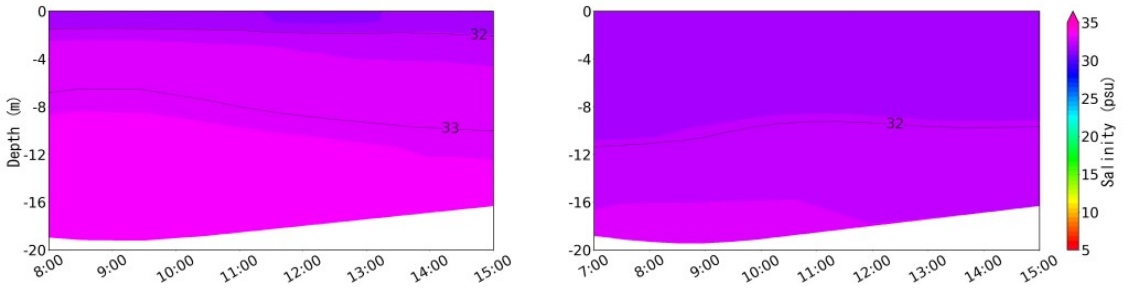

2018/08/26 (Weak stratification period)

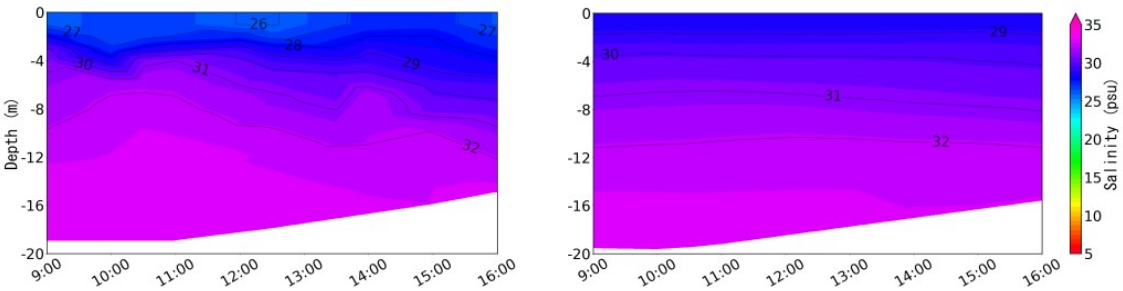

2019/08/02 (Strong stratification period)

Figure 5.5 Comparison of contour plots of salinity for each mixing state at the measurement point. Measurement results (left) and numerical model results (right).

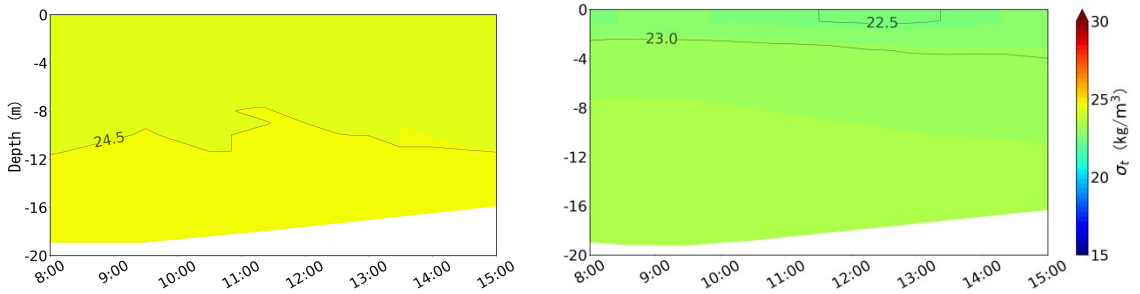

2018/12/07 (Well-mixed period)

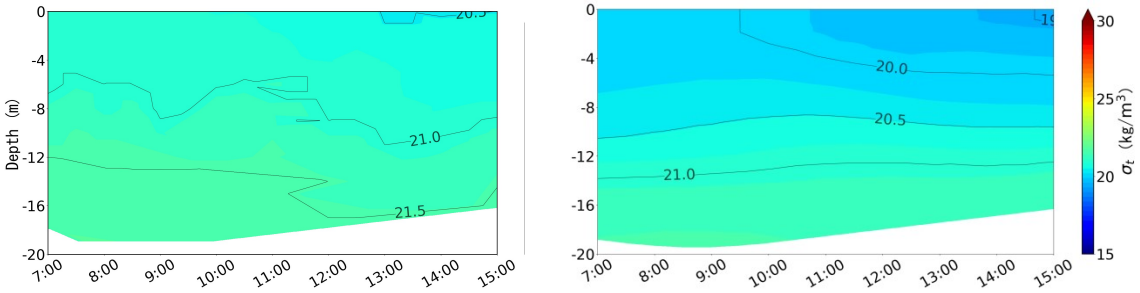

2018/08/26 (Weak stratification period)

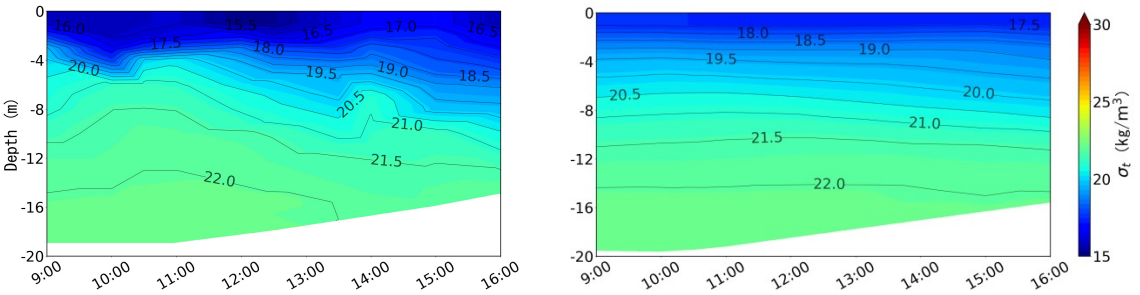

2019/08/02 (Strong stratification period)

Figure 5.6 Comparison of contour plots of σ_t for each mixing state at the measurement point. Measurement results (left) and numerical model results (right).

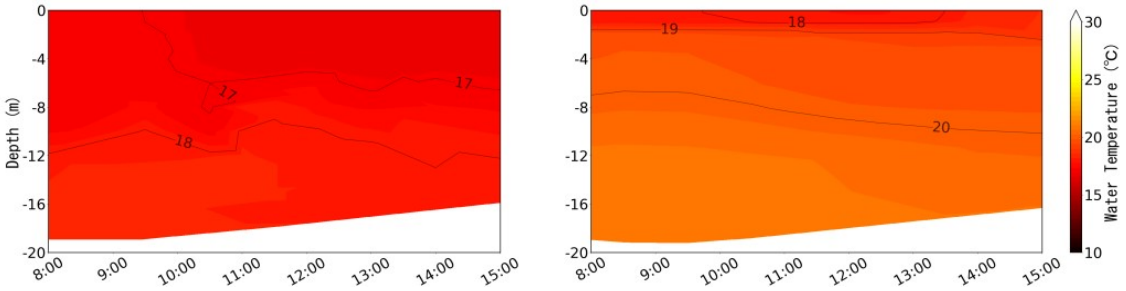

2018/12/07 (Well-mixed period)

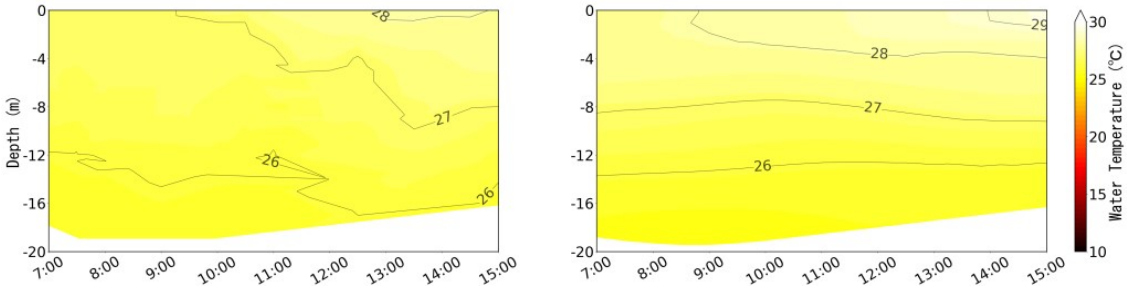

2018/08/26 (Weak stratification period)

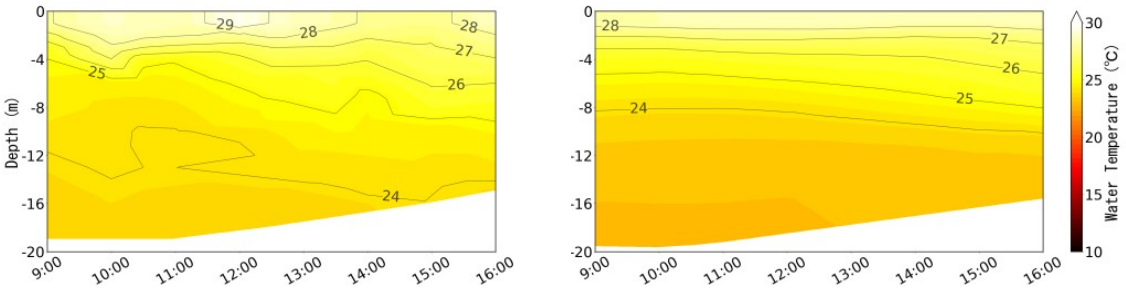

2019/08/02 (Strong stratification period)

Figure 5.7 Comparison of contour plots of water temperature for each mixing state at the measurement point. Measurement results (left) and numerical model results (right).

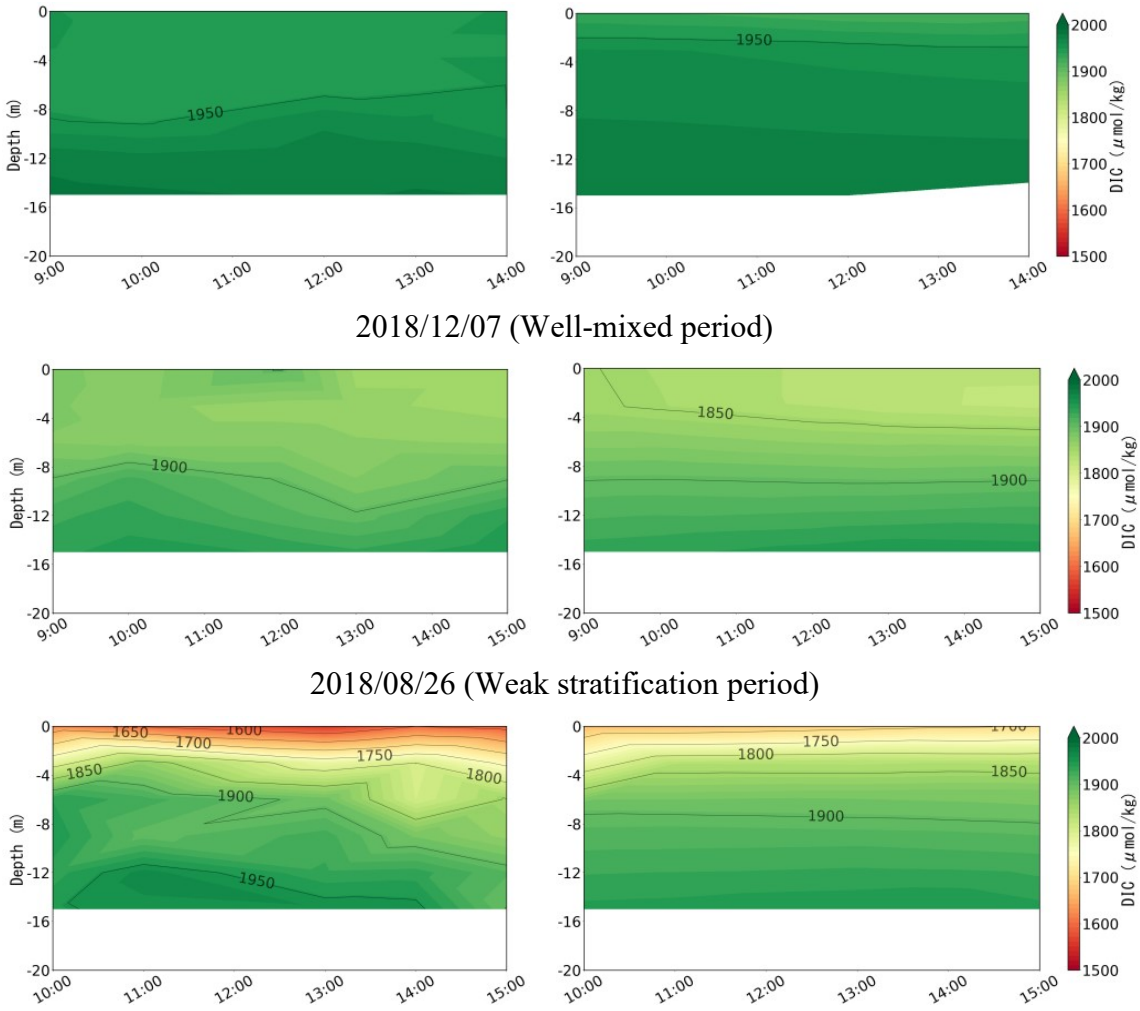

Figure 5.8 Comparison of contour plots of DIC for each mixing state at the measurement point. Measurement results (left) and numerical model results (right).

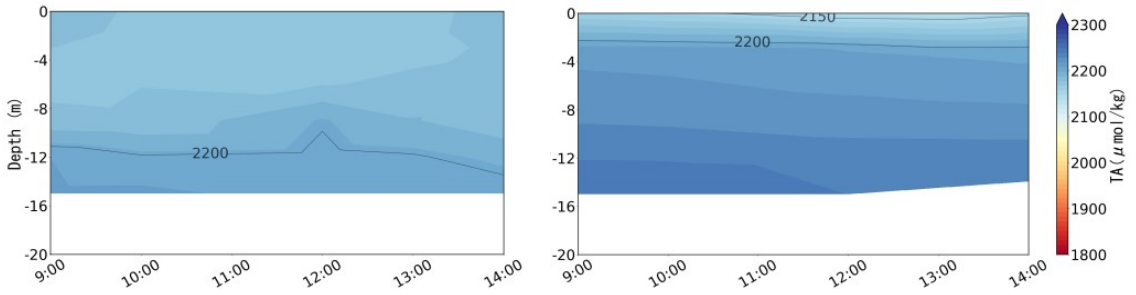

2018/12/07 (Well-mixed period)

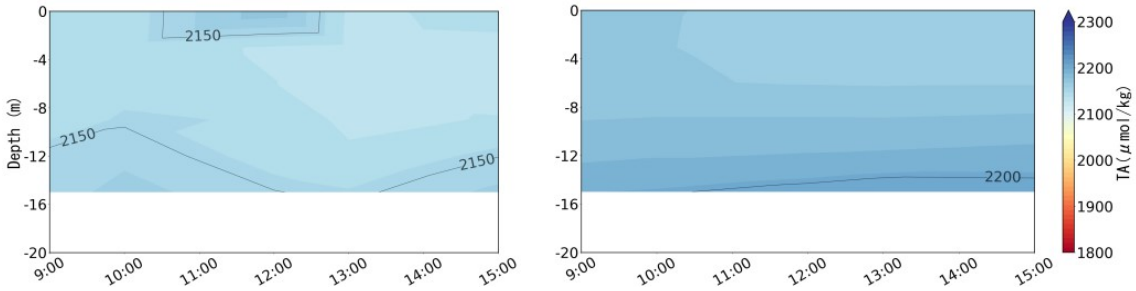

2018/08/26 (Weak stratification period)

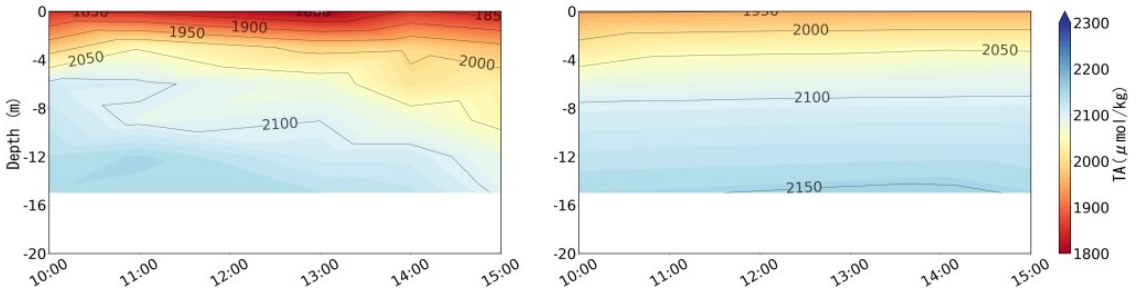

2019/08/02 (Strong stratification period)

Figure 5.9 Comparison of contour plots of TA for each mixing state at the measurement point. Measurement results (left) and numerical model results (right).

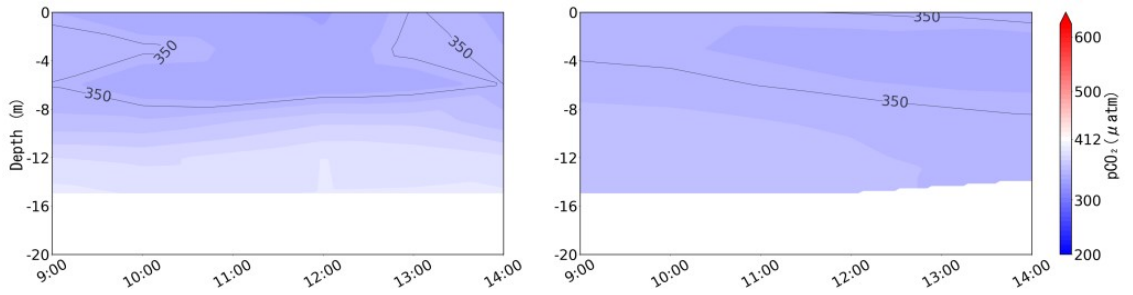

2018/12/07 (Well-mixed period)

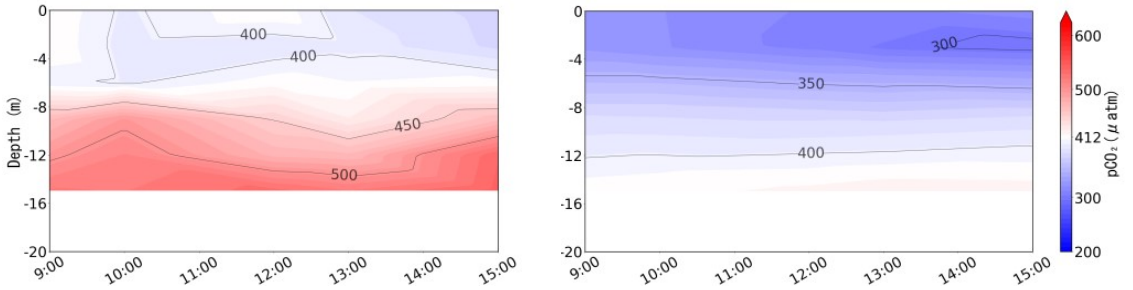

2018/08/26 (Weak stratification period)

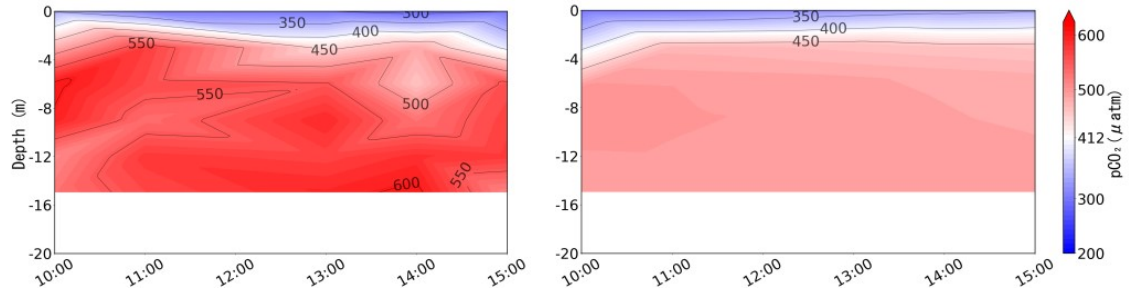

2019/08/02 (Strong stratification period)

Figure 5.10 Comparison of contour plots of pCO_2 for each mixing state at the measurement point. Measurement results (left) and numerical model results (right).

The comparison between the simulated values and the measured results in contour plots shows that the model can well simulate the dynamics and distribution of both hydrodynamic and ecological variables in the vertical direction. However, in the simulation of pCO_2 during weak and strong stratification (Fig.5.10), the state of high pCO_2 in the bottom layer under stratification was not well simulated. One of the more important reasons may be that the ecological module of the model did not consider the influence of zooplankton and benthic organisms, resulting in the process of their respiration, causing the increase of CO_2 concentration in the bottom water column not to be represented. These advanced biological processes can be added gradually in the subsequent modeling. Although the simulation results of pCO_2 in the bottom layer are not satisfactory, the surface pCO_2, which mainly controls the air-water CO_2 exchange, shows a more excellent fitting performance. Moreover, the overall CO_2 dynamic stratification state is better simulated. In summary, the simulated performance of the ecological module for CO_2 dynamics in the Kuma River estuary region is acceptable for our further analysis of CO_2 dynamics in the Yatsushiro Sea.

5.5.2 Analysis of vertical CO_2 dynamics in the estuary region

We analyzed the vertical CO_2 dynamics in the estuary area during the flood period (July) using the entrance to the Kuma River ((a) in Fig 5.11) to the horizontal west side of the Yatsushiro Sea boundary ((b) in Fig 5.11) as our inspection cross-section (red line in Fig 5.11).

The vertical cross-sectional distribution of salinity, pCO_2, and phytoplankton abundance at 12:00 on July 7, 2018, shortly after the flood, is shown in Fig.5.12, and the distribution at 12:00 on July 27, 2018, 20 days after the flood, is shown in Fig.5.13. According to the figure of pCO_2, red represents CO_2 release, and blue represents CO_2 absorption. In addition, the rightmost area is the mouth of the Kuma River.

From the salinity distribution, it can be seen that at 12:00 on July 7, the river water was concentrated in the surface layer. In addition, from the pCO_2 distribution, it can be seen that stratification occurs between river water with extremely high pCO_2 and seawater with low pCO_2. These results indicate that the release of CO_2 from the ocean to the atmosphere is accelerated immediately after the outflow of water due to the concentration of river water in the surface layer and the cover of freshwater.

On the other hand, at 12:00 on July 27, the influence of river water was diminished except for the area near the estuary where Yatsushiro Port is located, according to the salinity distribution. And phytoplankton proliferated in the waters away from the estuary. The distribution patterns of phytoplankton abundance and pCO_2 are consistent. These results indicate that the direct influence of river water is diminished when river water is mixed with seawater after a long period of time has passed since the outflow of water, and that pCO_2 is reduced in the surface layer where photosynthesis is concentrated due to the proliferation of phytoplankton caused by nutrient efflux from the discharge of fresh water, and that CO_2 absorption into seawater is also enhanced.

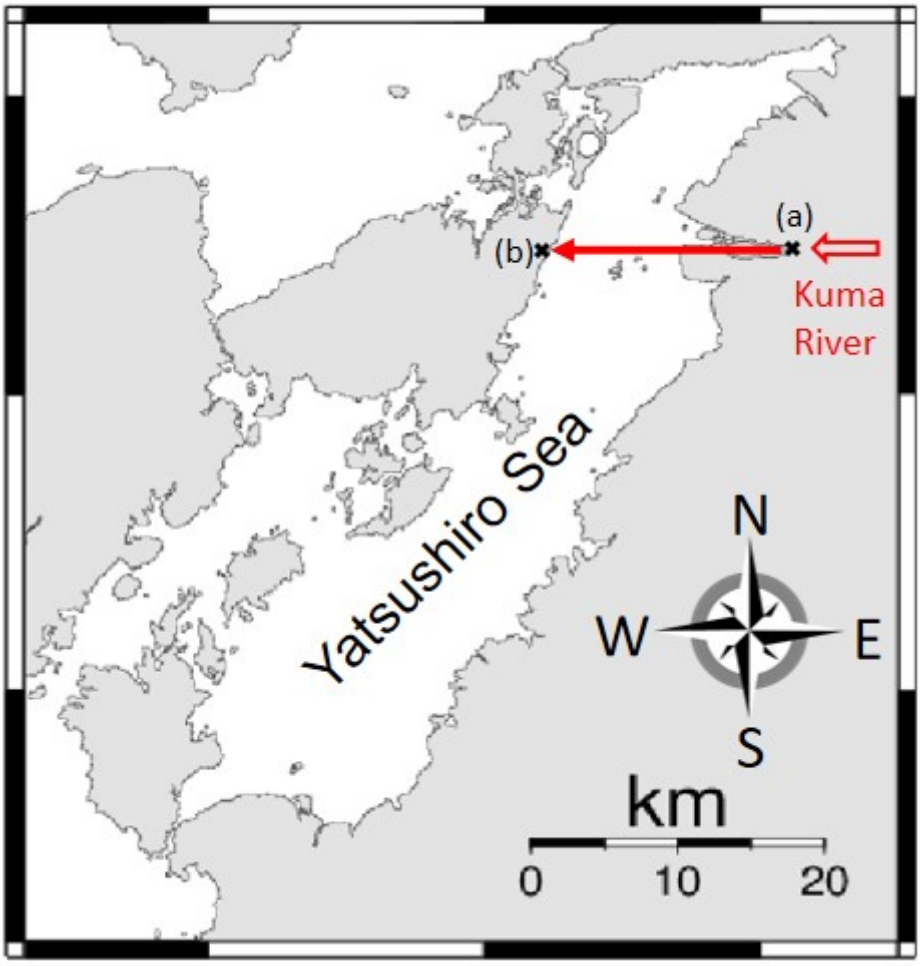

Figure 5.11 Location of the inspection cross-section. (Redline)

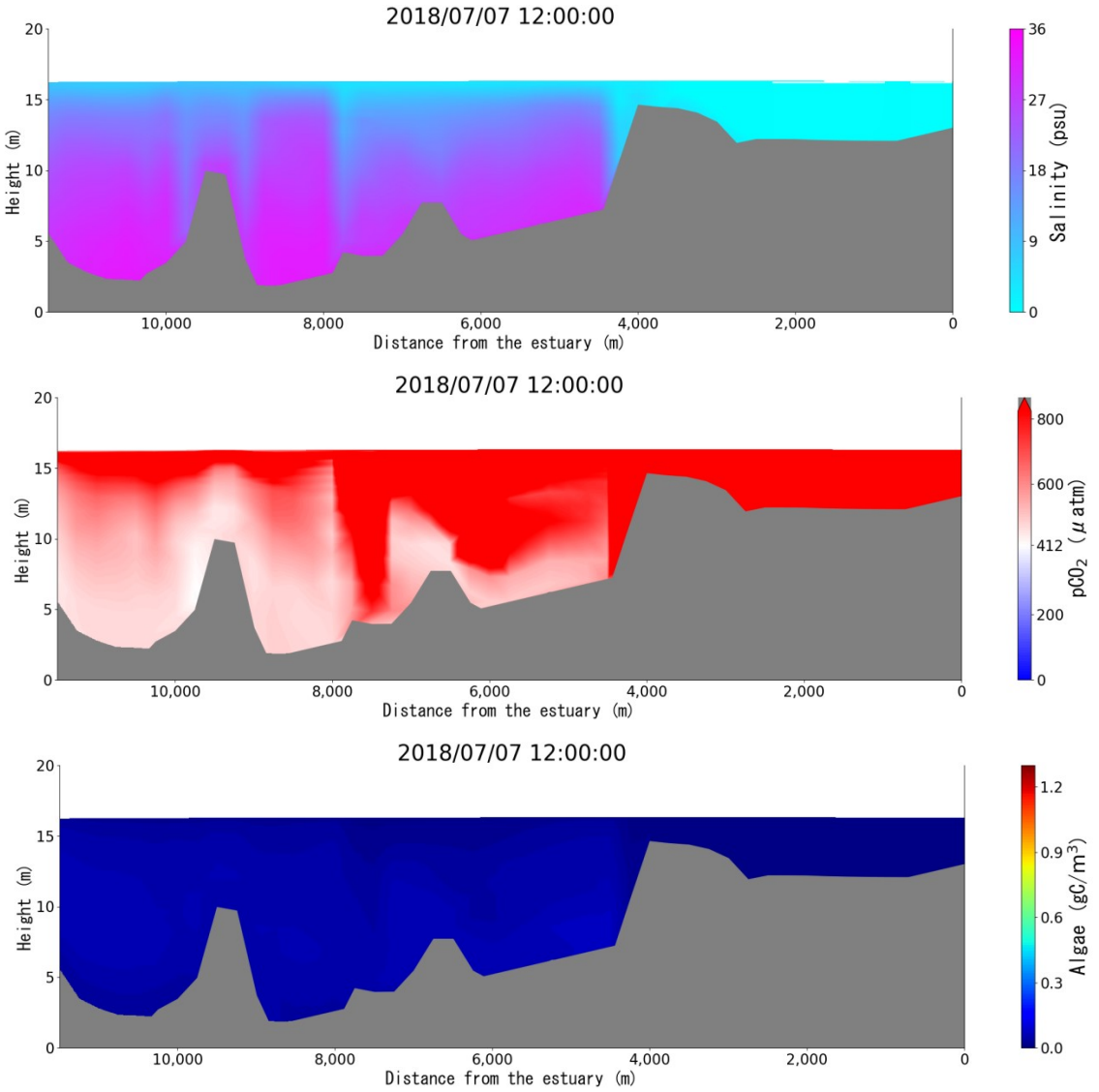

Figure 5.12 Vertical cross-sectional distribution at 12:00 on July 7, 2018.

(Top: salinity, middle: pCO_2, bottom: phytoplankton abundance)

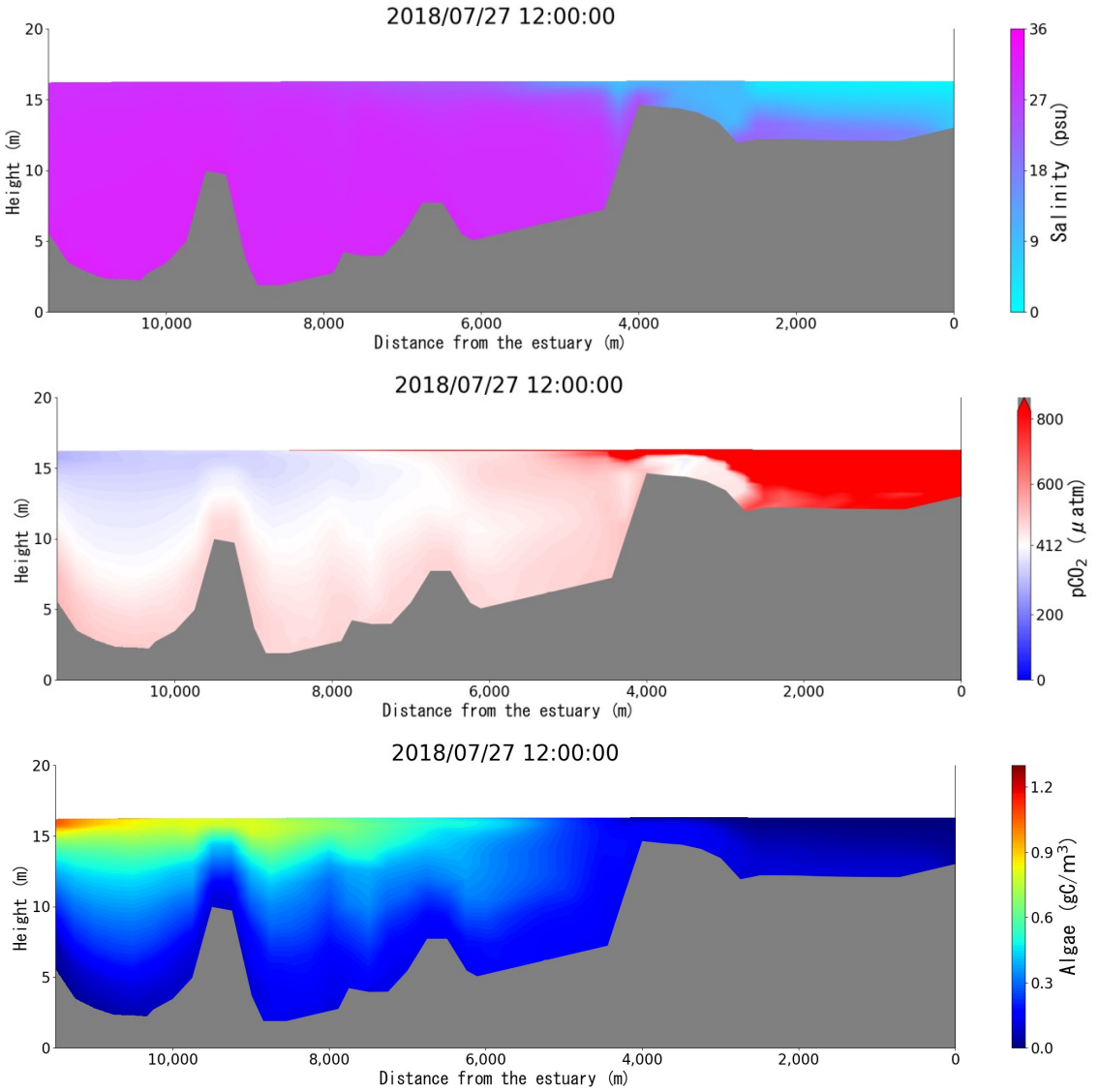

Figure 5.13 Vertical cross-sectional distribution at 12:00 on July 27, 2018.

(Top: salinity, middle: pCO_2, bottom: phytoplankton abundance)

5.6 Conclusions

In this study, we developed a numerical model of CO_2 dynamics that can reproduce the results of field measurements in the Yatsushiro Sea, with the aim of obtaining basic knowledge of CO_2 dynamics in shallow coastal areas. The developed model reproduced well the distribution of pCO_2, salinity, density, and temperature under different stratification conditions.

From the hindcast calculation by the numerical model, it was confirmed that the CO_2 sequestration around the estuary fluctuates greatly in space and time with the flooding event. In addition, although each of the elementary processes related to CO_2 dynamics that can be represented in the model is known, two tempo-spatial effects of large-scale runoff on coastal CO_2 absorption were identified at the site where they interact.

1. Immediately after river water discharge, the formation of a cap on the surface of seawater by the river water accelerates the release of CO_2 from seawater into the atmosphere.

2. As the mixing of the discharged river water progresses, the absorption of CO_2 into the seawater is enhanced, coupled with the effect of phytoplankton proliferation caused by nutrient runoff from the discharge.

References

Abe, J. (2003). Formation of High Turbidity Layer and Oxygen Consumption Process in the Western Ariake Sea. *Journal of Japan Society of Civil Engineers, Ser. B2 (Coastal Engineering)*, *50*, 996–970.

Acha, E. M., Piola, A., Iribarne, O., & Mianzan, H. (2015). *Ecological processes at marine fronts: oases in the ocean*. Springer.

Alosairi, Y., & Alsulaiman, N. (2019). Hydro-environmental processes governing the formation of hypoxic parcels in an inverse estuarine water body: Model verification and discussion. *Marine Pollution Bulletin*, *144*, 92–104.

Arakawa, H., Kanda, Y., & Ishihara, T. (2007). Prediction of Sea Surface Wind Distribution with a Three Dimensional Wind Model. *PROCEEDINGS OF COASTAL ENGINEERING, JSCE*, *54*, 131–135. https://doi.org/10.2208/proce1989.54.131

Blauw, A. N., Los, H. F. J., Bokhorst, M., & Erftemeijer, P. L. A. (2009). GEM: A generic ecological model for estuaries and coastal waters. *Hydrobiologia*, *618*(1), 175–198. https://doi.org/10.1007/s10750-008-9575-x

Chen, Z., Huang, P., & Zhang, Z. (2019). Interaction between carbon dioxide emissions and eutrophication in a drinking water reservoir: A three-dimensional ecological modeling approach. *Science of the Total Environment*, *663*, 369–379. https://doi.org/10.1016/j.scitotenv.2019.01.336

Deltares. (2014). D-Water Quality Processes Technical Reference Manual. *Delft, Netherlands*, 393.

Deltares. (2018). D-water Quality Processes Library Description. *Deltares, Delft, Netherlands,* 464.

Fair, G. M., Geyer, J. C., & Okun, D. (1968). Water and waste-water engineering. Volume 2. Water purification and waste-water treatment and disposal. *John Wiley & Sons. Inc., New York*, 670.

Falkowski, P. G., & Raven, J. A. (2013). *Aquatic photosynthesis*. Princeton University Press.

Gurel, M., Tanik, A., Gonec, E., and Russo, R. C. (2005). *Biogeochemical Cycles. In: J. P. Wolflin & I. E. Gonenc, eds. Coastal Lagoons. s.l.:CRC Press.* .

Hao, L., Sato, Y., Yano, S., Xiong, B., & Chi, B. (2021). Effects of Large-Scale Effluent of the Chikugo River due to 2020 Kyushu Floods on the Development of

Hypoxia in the Ariake Sea. *Journal of Japan Society of Civil Engineers, Ser. B2 (Coastal Engineering)*, *77*(2), I_865-I_870. https://doi.org/10.2208/kaigan.77.2_I_865

Hydraulics, W. (2005a). Delft3D-Flow User Manual. *WL/Delft Hydraulics*, 614.

Hydraulics, W. (2005b). Delft3D-WAQ Technical Reference Manual. *WL/Delft Hydraulics*, 354.

Kizaburo, N. (1993). Ecosystem model - Formulation and estimation of unknown parameters. *Journal of Advanced. Marine Technology Conference*, *8*, 99-138.

Kono, K. (2010). Analytical study on the North Pacific subtropical front (The Paper for the 2009 Okada Prize of the Oceanographic Society of Japan). *Oceanography in Japan*, *19*(2), 127-137.

Menshutkin, V. V, Rukhovets, L. A., & Filatov, N. N. (2014). Ecosystem modeling of freshwater lakes (review): 2. Models of freshwater lake's ecosystem. *Water Resources*, *41*(1), 32-45. https://doi.org/10.1134/S0097807814010084

Niu, L., van Gelder, P., Zhang, C., Guan, Y., & Vrijling, J. K. (2016). Physical control of phytoplankton bloom development in the coastal waters of Jiangsu (China). *Ecological Modelling*, *321*, 75-83.

Nixon, J. N. K. & S. W. (1987). *Analysis of coastal ecosystems*.

Steele, J. H. (1962). Environmental control of photosynthesis in the sea. *Limnology and Oceanography*, *7*(2), 137-150.

Stumm, W. and J. M. (1981). Aquatic chemistry. An introduction emphasizing chemical equilibria in natural water. *John Wiley & Sons, Inc.*

Tadokoro, M., & Yano, S. (2019). EVALUATION OF EFFECTS OF TEMPERATURE AND RIVER DISCHARGE CHANGES DUE TO CLIMATE CHANGE ON HYPOXIA IN THE ARIAKE SEA. *Journal of Japan Society of Civil Engineers, Ser. B2 (Coastal Engineering)*, *75*(2), I_1231-I_1236. https://doi.org/10.2208/kaigan.75.I_1231

Truesdale, G. A., Downing, A. L., & Lowden, G. F. (1955). The solubility of oxygen in pure water and sea-water. *Journal of Applied Chemistry*, *5*(2), 53-62.

Valiela, I., & Valiela, I. (1995). *Marine ecological processes* (Vol. 686). Springer.

Verspagen, J. M. H., Van de Waal, D. B., Finke, J. F., Visser, P. M., Van Donk, E., & Huisman, J. (2014). Rising CO2 levels will intensify phytoplankton blooms in eutrophic and hypertrophic lakes. *PloS One*, *9*(8), e104325.

Weiss, R. (1974). “Carbon dioxide in water and seawater.” *Marine Chemistry*, *2*(3), 203–216.

Weiss, R. F. (1970). The solubility of nitrogen, oxygen and argon in water and seawater. *Deep Sea Research and Oceanographic Abstracts*, *17*(4), 721–735.

Yamaguchi, S., & Hayami, Y. (2018). Impact of Isahaya dike construction on DO concentration in the Ariake Sea. *Journal of Oceanography*, *74*(6), 565–586.

Yokoyama, N. (1993). *Marine Environment Simulation : Water Flow and Organisms*.

Chapter 6
Analysis of Seawater CO_2 Dynamics of the Whole Yatsushiro Sea through Numerical Simulation

6.1 Introduction

Previous studies have shown that pCO_2 fluctuates with the development of the stratification (Fujii et al., 2011; Tada et al., 2018). For example, we reported that pCO_2 in the surface layer decreases during stratification due to phytoplankton photosynthesis in Chapter 3. However, few cases of detailed field studies and model development focus on the relationship between stratification and pCO_2, and the effect of stratification on coastal CO_2 uptake has yet to be clarified.

In Chapter 5, we developed a numerical model of CO_2 dynamics that can reproduce the results of past field measurements in the Yatsushiro Sea. Moreover, we used this model to analyze the CO_2 dynamics and influencing factors in the Kuma River estuary area. However, the CO_2 dynamics in other bay regions are still unknown, especially in the southern area, which is far from the estuary. In addition, the effects of stratification on the seawater CO_2 dynamics in the Yatsushiro Sea are unclear and need further study.

For this reason, we try to improve the performance of the numerical model further so that it can reproduce the CO_2 dynamics over the full range of the Yatushiro Sea. Then we analyze the CO_2 dynamics and the corresponding influence mechanism (especially the effects of stratification) of the entire bay. Finally, estimate 2018's CO_2 flux through the numerical simulation results.

6.2 Model improvement

Based on the good model fit results near the estuary of the Kuma River (see Section 5.5), we optimized the model's applicability regarding the hydrodynamic simulation of the whole area of the Yatsushiro Sea. The process is based on the regular twice-monthly measurements of the central bay route (i.e., the line of nine measurement sites between St.11 and St.19 in Fig.6.1) implemented by the MLIT in 2018 to calibrate and verify the simulation results. In this process, we calibrated and verified the water temperature, salinity, and seawater density. In addition, we applied the concept of density stratification index (SI) proposed by Simpson et al. (1990), to quantify the strength of density stratification (Simpson et al., 1990). Based on the process of calibrating and validating the SI, we improved the simulation accuracy of the hydrodynamic model for the stratification state of the whole area of the bay. The formula for calculating the SI is shown in Equation (6-1).

$$SI = -\frac{1}{H}\int_{-H}^{0}(\rho - \overline{\rho})g \cdot z \cdot dz \tag{6-1}$$

where, $\rho=\rho(z)$ is the water density profile over the water column of depth H, bar means depth averaging, g is the gravitational acceleration, and z is the vertical coordinate.

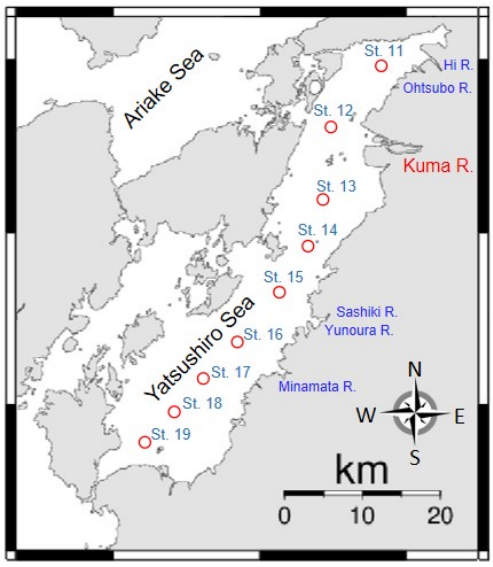

Figure 6.1 Location of the field measurement points conducted by MLIT.

6.3 Simulation of CO_2 dynamics in the entire bay

6.3.1 Vertical and horizontal CO_2 dynamics

We applied the developed hydrodynamic-ecological model to simulate the CO_2 dynamics in the whole area of the Yatsushiro Sea for the entire year of 2018. Based on the simulation results, we analyzed the dynamics of CO_2 in the bay in horizontal and vertical directions at different periods and the corresponding influence mechanism. In addition, we also analyze the changes of CO_2 dynamics in seawater during the flooding period, which is the period of large fluctuations in stratification conditions, and the corresponding influence mechanism by comparing the vertical dynamics of the areas in the Yatsushiro Sea that are more and less influenced by freshwater inflow during the flooding period.

6.3.2 Calculation of F_{CO2}

We used the model to estimate the F_{CO2} between seawater and the atmosphere in the Yatsushiro Sea during a full year in 2018. Current methods for estimating the F_{CO2} are mainly based on the block volume equation, which is as follows:

$$F_{CO_2} = K_w \cdot s \cdot (pCO_{2water} - pCO_{2air}) \tag{6-2}$$

where the solubility s can be expressed as a function of temperature and salinity (Wanninkhof, 1992; Weiss, 1974), and pCO_{2water} and pCO_{2air} represent the pCO_2 in seawater and atmosphere, respectively. Since the pCO_2 in the atmosphere is almost constant throughout the year, compared to the pCO_2 in seawater. Therefore, F_{CO2}, which determines whether the shallow coastal waters are a sink or a source of atmospheric CO_2, is mainly determined by the pCO_2 in seawater. The gas exchange coefficient K_w depends on the physical processes at the sea surface and is usually estimated using sea surface dynamical parameters.

The CO_2 solubility in seawater (mol/L/atm) can be calculated from the existing empirical Equation (6-3) based on water temperature and salinity (Weiss, 1974).

$$\begin{aligned} \ln s = &-58.0931 + 90.5069 \times (\frac{100}{T}) + 22.2940 \times \ln(\frac{T}{100}) + S \\ &\times [0.027766 + (-0.025888) \times (\frac{T}{100}) + 0.0050578 \times (\frac{T}{100})^2] \end{aligned} \tag{6-3}$$

$$T = t + 273.15 \tag{6-4}$$

where S: absolute salinity (‰), T: water temperature (K), t: water temperature (°C). Absolute salinity (‰) is considered to be the same as actual salinity (psu).

Various parameters influence the CO_2 in seawater. First, even if the concentration of CO_2 in seawater is constant, if the solubility of CO_2 in seawater changes, the pCO_2 will also change. Solubility is a value that indicates the amount of a gas that can be dissolved in water under certain conditions. In general, solubility tends to decrease as the temperature increases. This is because the higher the temperature of the water, the higher the partial pressure (kinetic energy) of the gas molecules dissolved in the water, and the more they want to escape to the atmosphere. In the case of CO_2, the solubility of CO_2 decreases with the increase of water temperature, and the pCO_2 in

seawater increases. The pCO_2 in the atmosphere also increases with increasing temperature, but its effect is not as great as that of water. This is because atmospheric CO_2 molecules already have higher kinetic energy than those in water because they are not bound by water molecules.

In this study, considering the size of the study area and the resolution of the wind speed data, we chose the empirical equation of Wanninkhof (1992) to calculate K_w, which is as follows:

$$K_{\mathrm{w}} = 0.39 U_{10}{}^{2} \left(\frac{S_C}{660}\right)^{-\frac{1}{2}} \tag{6-5}$$

where U_{10} is the wind speed at the height of 10 m above the water surface and S_C is the Schmidt number.

The Schmidt number varies linearly with salinity (S) (Borges et al., 2004). In this study, the existing empirical Equations (6.6)-(6.8) of Wanninkhof (1992) were used to calculate the Schmidt number for $S = 35$ and $S = 0$.

$$S_C = \frac{S_{C,sea} - S_{C,fresh}}{35} \cdot S + S_{C,fresh} \tag{6-6}$$

$$S_{C,sea} = (2073.1 - 125.62 \cdot t + 3.6276 \cdot t^2 - 0.043219 \cdot t^3) \tag{6-7}$$

$$S_{C,fresh} = (1911.1 - 118.11 \cdot t + 3.4527 \cdot t^2 - 0.041320 \cdot t^3) \tag{6-8}$$

where $S_{c,sea}$ is the Schmidt number of open seawater ($S = 35$), $S_{c,fresh}$ is the Schmidt number of freshwater ($S = 0$), and t is the water temperature (°C).

Due to the large area of the Yatsushiro Sea, it is difficult to obtain very accurate wind speed data for the calculation of F_{CO2}. Figure 6.2 shows the wind observation stations around the bay. In order to estimate F_{CO2} more precisely, we divided the bay into four areas (See A1 to A4 in Fig.6.2) near four wind observation stations by referring to the results of water quality and environmental characteristics analysis of the bay (Sonoda et al., 2013), and then calculated F_{CO2} for each area separately.

In addition, U_{10} is corrected in height by a power law from the data of each observatory shown in Equation 6.9 (Ishizaki and Mitsuta, 1962).

$$U_{10} = U_Z \cdot (\frac{10}{Z})^{\frac{1}{n}} \tag{6-9}$$

where, U_Z is the wind speed at the height Z from the sea level, and $1/n$ is the index that should be determined by the surface condition of the observation point. For each station, the values of Z and n obtained from the Japan Road Association (2007) were used, shown in Table 6.1. U_Z was converted to sea breeze using Carruthers' conversion factor from surface to offshore wind, see Section 5.2.

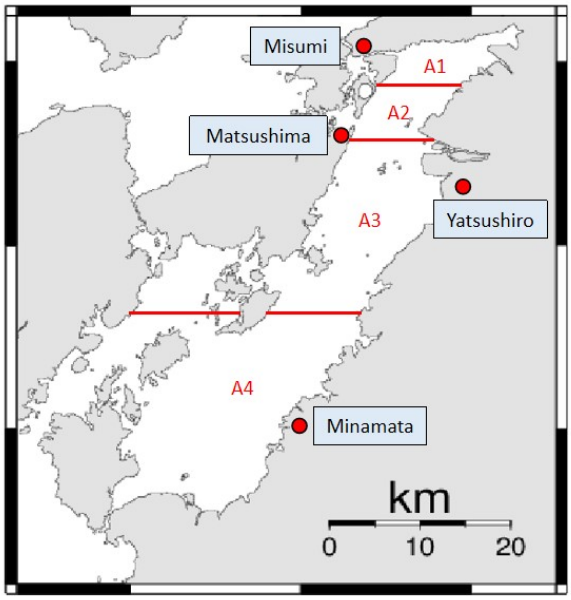

Figure 6.2 Schematic diagram of the Yatsushiro Sea subdivision (A1 to A4 separated by red lines) and the location of the wind observatories (red dots).

Table 6.1 the values of Z and n for each area.

Station	*Z*	*n*
Misumi (A1)	70	4
Matsushima (A2)	10.1	7
Yatsushiro (A3)	18	7
Minamata (A4)	12.5	4

6.4 Results and Discussions

6.4.1 Model verification of the whole Yatsushiro Sea

The verified objects are salinity, σ_t, and water temperature. As in Section 5.5.1, we first calculate the *r*, *RMSE*, and d_{ref} values between simulated and measured values for each site, and the results are presented in Table 6.2.

Table 6.2 Summary of performance statistics for model verification of the Yatsushiro Sea.

Station	Variable	Units	[1]*r*	[2]*RMSE*	[3]d_{ref}	[4]*n*
St.11	Salinity	psu	0.39	2.05	0.18	185
	σ_t	kg/m^3	0.85	1.71	0.67	
	Temperature	℃	0.99	1.53	0.89	
St.12	Salinity	psu	0.44	1.41	0.39	256
	σ_t	kg/m^3	0.90	1.15	0.78	
	Temperature	℃	0.99	1.27	0.91	
St.13	Salinity	psu	0.66	0.76	0.63	309
	σ_t	kg/m^3	0.97	0.52	0.90	
	Temperature	℃	0.99	1.22	0.90	
St.14	Salinity	psu	0.54	0.83	0.57	391
	σ_t	kg/m^3	0.95	0.58	0.89	
	Temperature	℃	0.99	1.15	0.91	
St.15	Salinity	psu	0.75	0.63	0.62	391
	σ_t	kg/m^3	0.98	0.37	0.91	
	Temperature	℃	0.99	1.06	0.91	
St.16	Salinity	psu	0.81	0.61	0.63	390
	σ_t	kg/m^3	0.99	0.36	0.92	
	Temperature	℃	0.99	1.05	0.91	
St.17	Salinity	psu	0.74	0.67	0.58	391
	σ_t	kg/m^3	0.99	0.38	0.91	
	Temperature	℃	0.99	1.04	0.91	
St.18	Salinity	psu	0.73	0.76	0.53	391
	σ_t	kg/m^3	0.99	0.46	0.88	
	Temperature	℃	0.99	0.97	0.91	
St.19	Salinity	psu	0.71	0.87	0.49	391
	σ_t	kg/m^3	0.98	0.55	0.87	
	Temperature	℃	0.99	0.96	0.92	

[1] *r*: Pearson's correlation coefficient.

[2] *RMSE*: root mean square error.

[3] d_{ref}: refined Willmott index.

[4] *n*: number of samples.

Then we performed the output of the contour plot, and the x-axis represents the distance between each measurement site (St.11 to St.19 shown at the top of each figure). We selected the more representative ones among the many comparison results, that is, the results of three-time points similar to the mixing period, weak stratification period, and strong stratification period in Section 5.5.1, to show. The results are shown in Fig.6.3 to Fig.6.5.

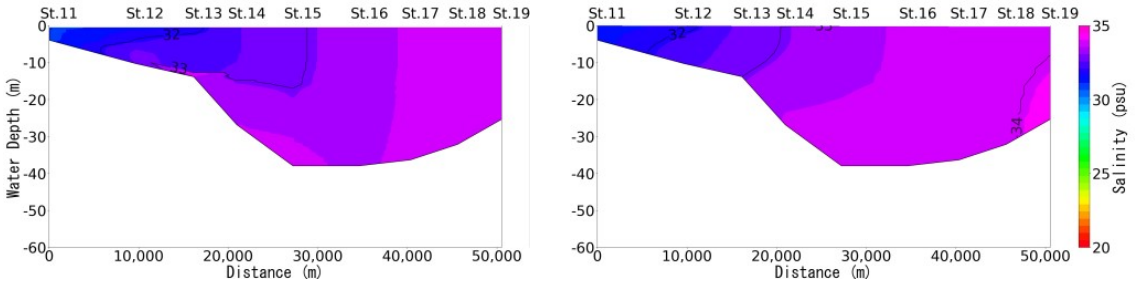

2018/11/15 (Well-mixed period)

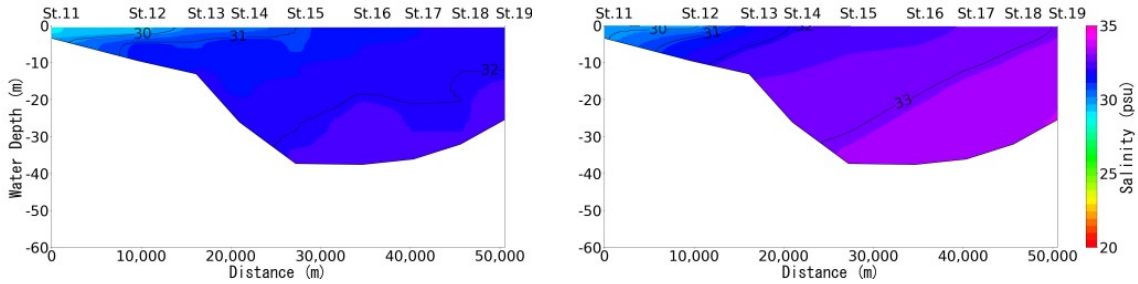

2018/08/17 (Weak stratification period)

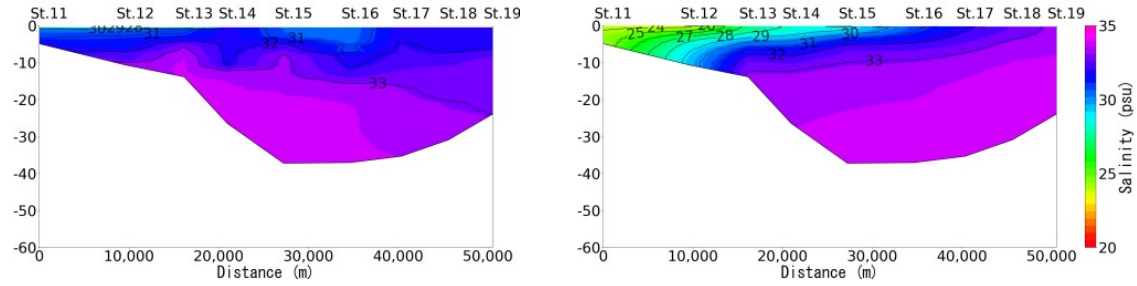

2019/05/10 (Strong stratification period)

Figure 6.3 Comparison of contour plots of salinity for each mixing state at each point. Measurement results (left) and numerical model results (right).

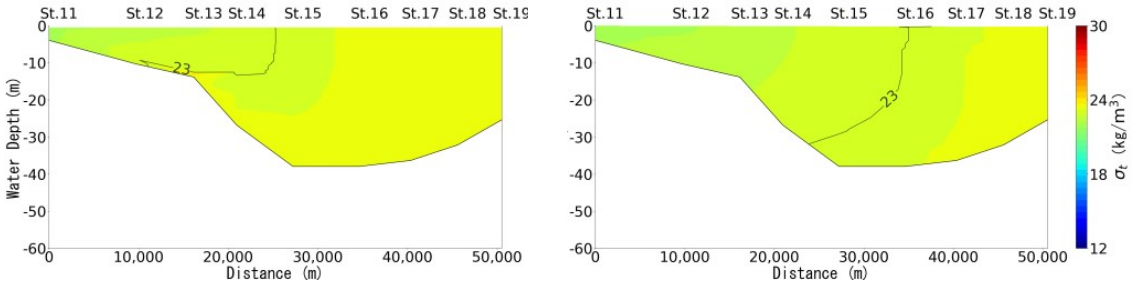

2018/11/15 (Well-mixed period)

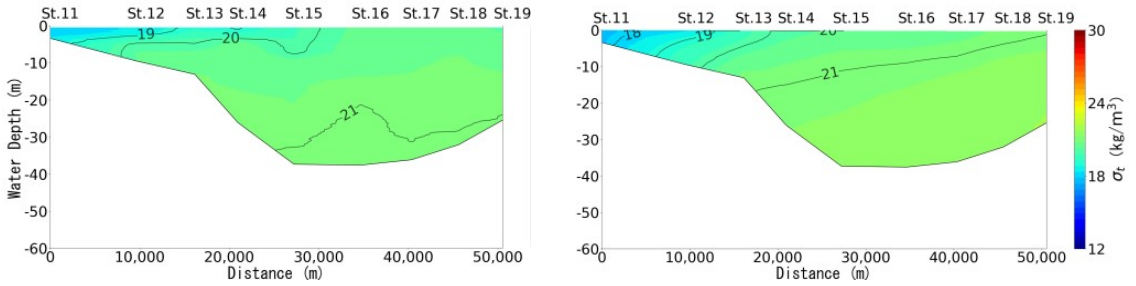

2018/08/17 (Weak stratification period)

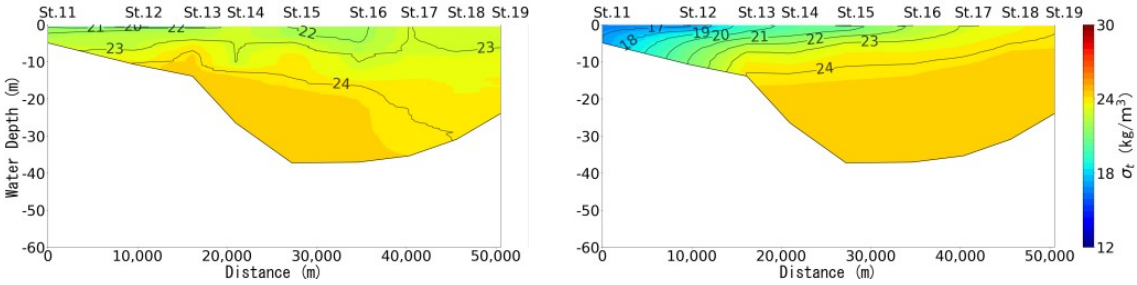

2019/05/10 (Strong stratification period)

Figure 6.4 Comparison of contour plots of σ_t for each mixing state at each point. Measurement results (left) and numerical model results (right).

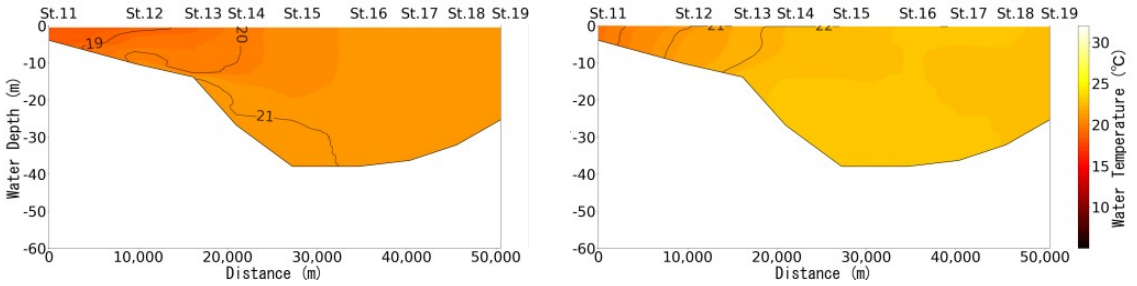

2018/11/15 (Well-mixed period)

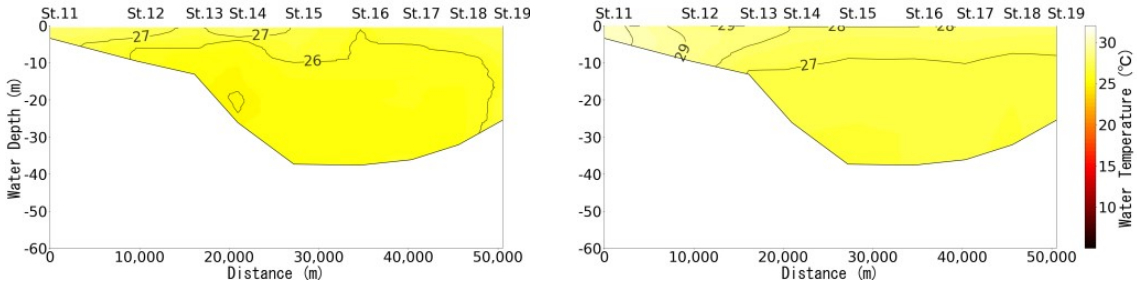

2018/08/17 (Weak stratification period)

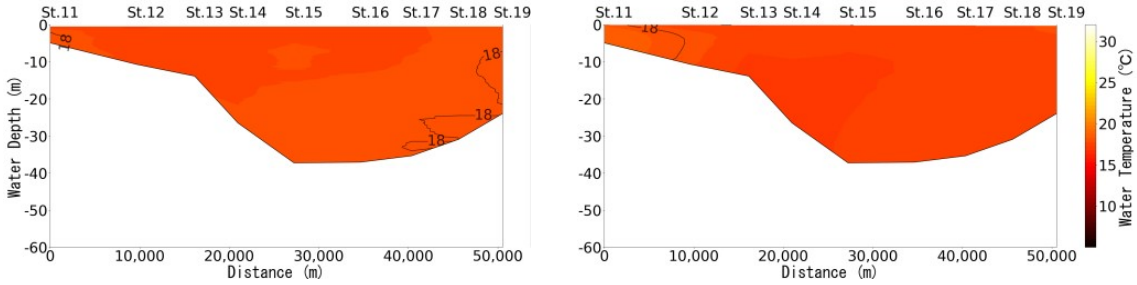

2019/05/10 (Strong stratification period)

Figure 6.5 Comparison of contour plots of water temperature for each mixing state at each point. Measurement results (left) and numerical model results (right).

In addition, we calculated the stratification index of field measurements and model calculations for each station separately according to Equation (6-1) and made a comparison plot between simulated and measured values shown in Fig.6.6.

We also calculated r, $RMSE$, and d_{ref} for the comparison results of each station, and the results show that the model performance of each site is within an acceptable range. St.16, St.17, St.18, and St.19, which are farther from the Kuma River estuary and located in the southern part of the bay, show excellent relations ($r > 0.9$). In contrast, St.13, St14, and St.15, which are located northward near the estuary of the Kuma River, perform relatively poorly. This is due to the fact that simulating areas with large freshwater inflow is indeed a huge challenge, which is one of our main objectives in this study. However, totally it is still in an acceptable range ($r > 0.6$). In

contrast, the fit performance of St.11 and St.12, located in the northernmost part of the bay, is poorer (r < 0.3), probably because the strength of the model lies in simulating the stratification phenomenon of seawater. The water depth in this region, being too small, makes it easy to produce results that exceed expectations.

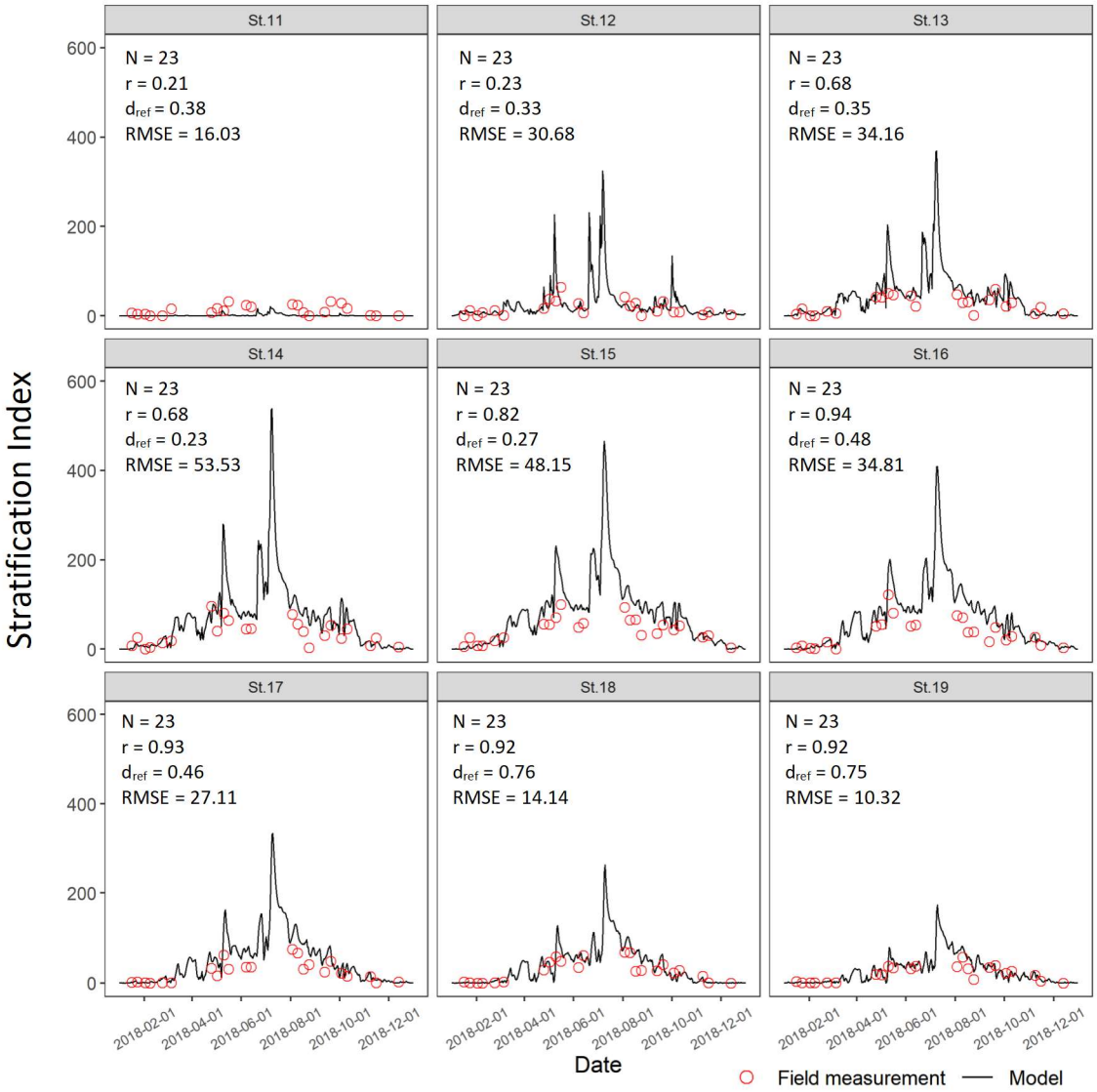

Figure 6.6 Comparison of stratification index between simulated results and measured results at each station.

In summary, we confirmed that the model performs well for the simulation of hydrodynamics and stratification in most areas of the bay and is sufficient to support our analysis of the horizontal and vertical CO_2 dynamics in the whole bay.

6.4.2 Simulation and analysis of CO_2 dynamics in the Yatsushiro Sea

We applied the verified model to simulate the CO_2 dynamics of the Yatsushiro Sea for the whole year of 2018. The full-year 2018 Kuma River flow rate and the average density stratification index of the bay are shown in (a) of Fig.6.7. We can see that the most critical driver of density stratification in the bay is the freshwater inflow from the Kuma River.

The horizontal pCO_2 distribution of the bay is shown in (b) of Fig.6.7 for several more typical periods, namely the period before the massive flooding of the Kuma River in July 2018 when it was less affected by freshwater inflow (2018/5/30), the period one week after the flooding (2018/07/10), the period three weeks after the flooding (2018/07/24), and the dry winter period (2018/12/01). The x- and y-axes in this figure represent the distance, while the z-axis represents the position in the σ coordinate system in a total of 17 layers. According to the vertical resolution of the model, the first and 17th layers are the surface and bottom layers of the water body, respectively, while the 14th layer is the part that accounts for 45% to 55% of the total water depth, which is considered to be the middle part of the water body.

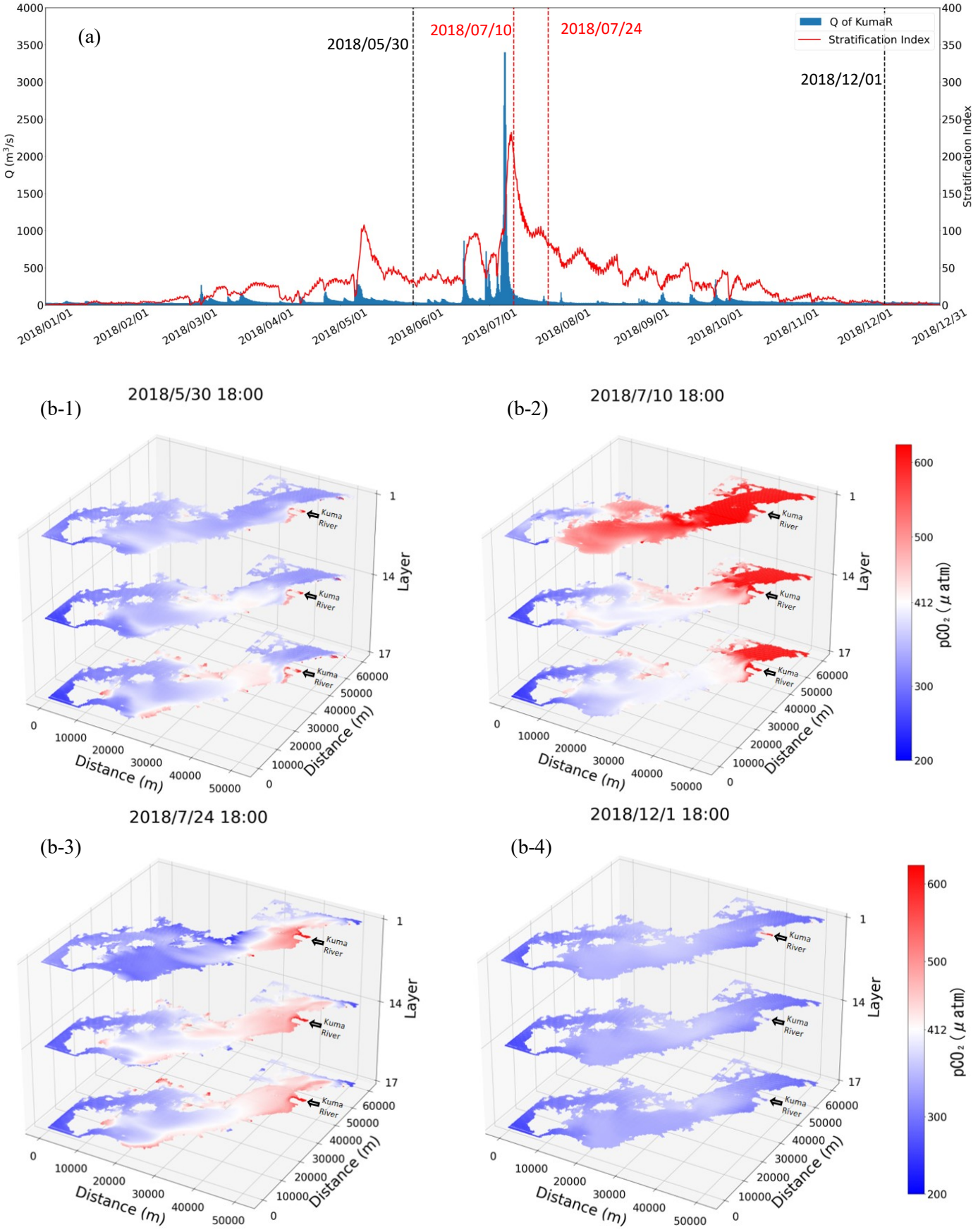

Figure 6.7 Comparison plots of the 2018 Kuma River flow rate and stratification index (a), and the horizontal distribution of pCO_2 for the four periods (b).

As we can see, the density stratification peaks (2018/7/9 18:00:00, SI = 232.26) about a week after the influx of large amounts of freshwater into the bay ((b-2) in Fig.6.7). At the same time, with the higher CO_2 concentration freshwater covering the surface of the seawater, the average pCO_2 concentration of the whole bay reached the peak (surface pCO_{2ave} = 726.31 μatm). The bay during this period exhibits a source of atmospheric CO_2 due to a combination of freshwater inflow and density stratification.

After another two weeks or so, we can see that the pCO_2 in the surface layer has dropped to a lower level (2018/7/24 18:00, surface pCO_{2ave} = 357.34 μatm), with only some high pCO_2 remaining in the surface water near the estuary. In the middle and bottom layers, however, the pCO_2 is higher than that of the surface layer. The main effect of stratification at that time is to inhibit the upwelling of water with higher pCO_2 in the bottom layer to the surface layer, resulting in the sink of seawater for atmospheric CO_2. In addition, we found that the pCO_2 in the central part of the bay (the region between distance from 20 to 40 km of the y-axis in Fig.6.7) is always slightly lower than that in the southern and northern parts during the periods less affected by freshwater inflow ((b-1), (b-4) in Fig.6.7). The main reasons for this phenomenon are, on the one hand, that the south and the north are farther away from the Kuma River than the central part, which makes the impact of freshwater more minor, and on the other hand, that the south is connected to the outer sea through the strait, while the north is connected to the Ariake Sea, which makes it easier for these two areas to reduce the impact of freshwater with high pCO_2 through seawater exchange.

The vertical dynamics of the two sites before and after the flooding period with time are shown in Fig.6.8. pCO_2 and phytoplankton biomass are examined. Two sites are St.13, near the estuary of the Kuma River ((a) in Fig.6.8), and St.18, located in the southern part of the bay, far from the estuary ((b) in Fig.6.8).

By the distribution of phytoplankton biomass in St.18 ((b) in Fig.6.8), we found that the phytoplankton biomass in this area was much higher around two weeks after the flood than before. In contrast, St.13 had a late start of phytoplankton proliferation due to the influence of freshwater residues. We suggest that during the period after the large-scale freshwater inflow, the bay was subjected to nutrient input from terrestrial sources, leading to a large phytoplankton bloom, thus making the period exhibit a

strong sink of atmospheric CO_2. This also resulted in the surface pCO_2 concentrations in most areas of the Yatsushiro Sea during this period (St.18, 2018/7/24 18:00, surface pCO_2 = 307.83 μatm) ((b-3) in Fig.6.7) being even lower than those before the flood (St.18, 2018/5/30 18:00, surface pCO_2 = 376.61 μatm) ((b-1) in Fig.6.7) and during the dry period (St.18, 2018/12/1 18:00, surface pCO_2 = 352.54 μatm) ((b-4) in Fig.6.7), except near the estuary.

At St.13, the influence of freshwater lasted for a long time, resulting in the surface pCO_2 (pCO_{2ave} = 539.94 μatm) being higher than the atmospheric pCO_2 (412 μatm) for about 40 days starting from June 20. However, at St.18, which is farther from the estuary, the surface layer pCO_2 decreased to a level below atmospheric pCO_2 only about 10 days after the surface layer was covered by freshwater with a high pCO_2 concentration. The surface pCO_2 concentration at this point reached the lowest value (257.82 μatm) at 17:00 on 2018/7/20, which was much lower than the middle layer (441.96 μatm) and the bottom layer (360.08 μatm), showing an apparent stratified state.

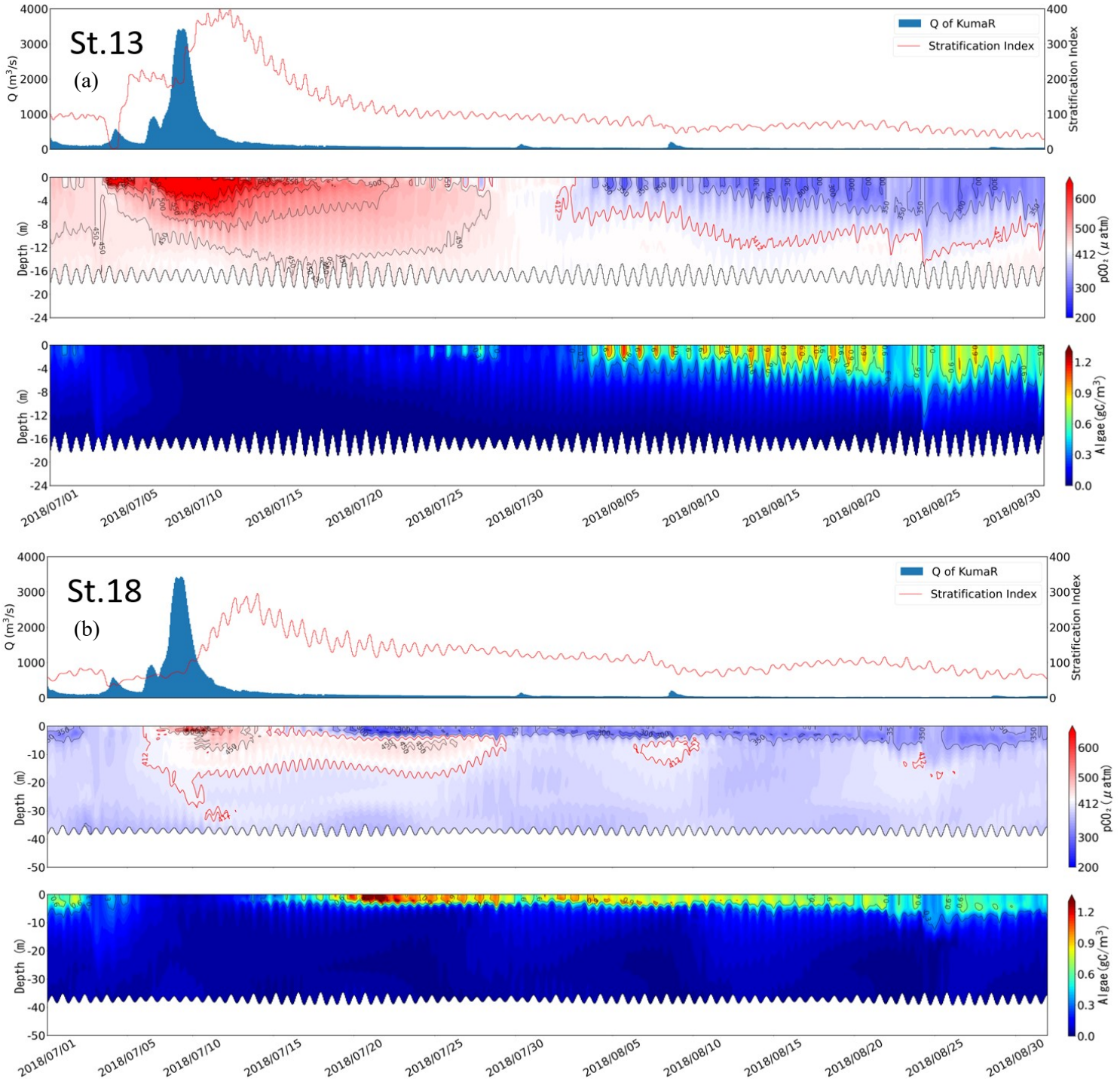

Figure 6.8 Comparison of the flow rate of the Kuma River and stratification index SI (top), pCO_2 distribution (middle, and the part enclosed by the red line is the part above 412 μatm), and algae biomass distribution (bottom) at St.13 and St.18 from July 1, 2018, to September 1, 2018.

6.4.3 Correlation between surface pCO_2 and stratification

Since stratification in the Yatsushiro Sea is mainly caused by freshwater inflow from the Kuma River, which in turn largely increases the pCO_2 concentration in the surface layer, it is difficult to evaluate the relationship between stratification and pCO_2 dynamics in isolation by ignoring the amount of pCO_2 increase caused by freshwater inflow.

The correlation plot between SI and surface pCO_2 from February 1, 2018, to December 31, 2018, is displayed in (a) of Fig.6.9. Because this simulation started on January 1, 2018, it takes about 30 days for the simulated values to reach a more accurate value, so only the results after February 1 are analyzed here. The results show that the surface pCO_2 of St.13 has a strong positive correlation with SI over nearly one full year (r = 0.87), while St.18, which is farther away from the estuary, does not show a significant correlation (r = 0.25). We speculate that this result may be due to the strength and duration of the freshwater influence.

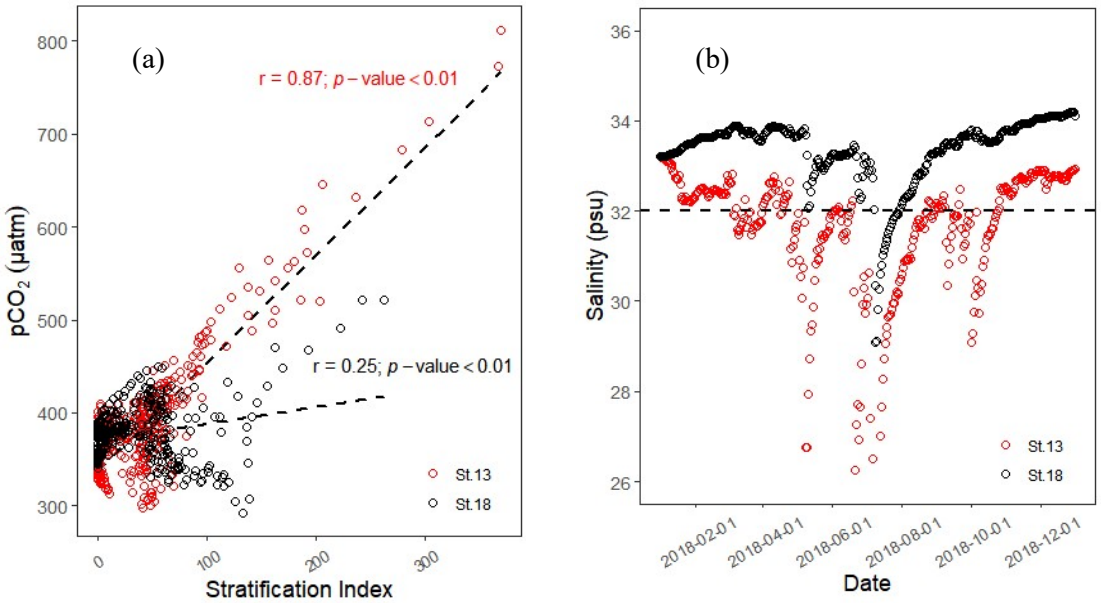

Figure 6.9 Linear correlation between surface pCO_2 and stratification index SI (a) and surface salinity of St.13 and St.18 in 2018 (b).

The value of salinity in seawater can be used as an indicator of the influence of freshwater. (b) in Fig.6.9 shows the trend of the surface salinity values of St.13 and St.18 in 2018. We use a salinity value of 32 psu as a cut-off, and we consider a salinity below 32 psu as being more strongly influenced by freshwater. From this figure, we know that St.13 is under a strong freshwater influence for most of the year, except for the dry winter period (mid-October to mid-January). St.18 is only about 25 days after the massive flood in July, when the salinity is below 32 psu.

We divided St.18 into the freshwater-influenced period (7/7 to 7/29), freshwater-abated period (7/29 to 10/17), and dry period (10/18 to 12/31) according to the strength of freshwater influence to explore the factors affecting surface pCO_2 separately. In addition to the relationship between SI and pCO_2, we also analyzed the correlation between water temperature, DIC, and algae together, where all the values except SI are surface values. The results are displayed in Fig.6.10.

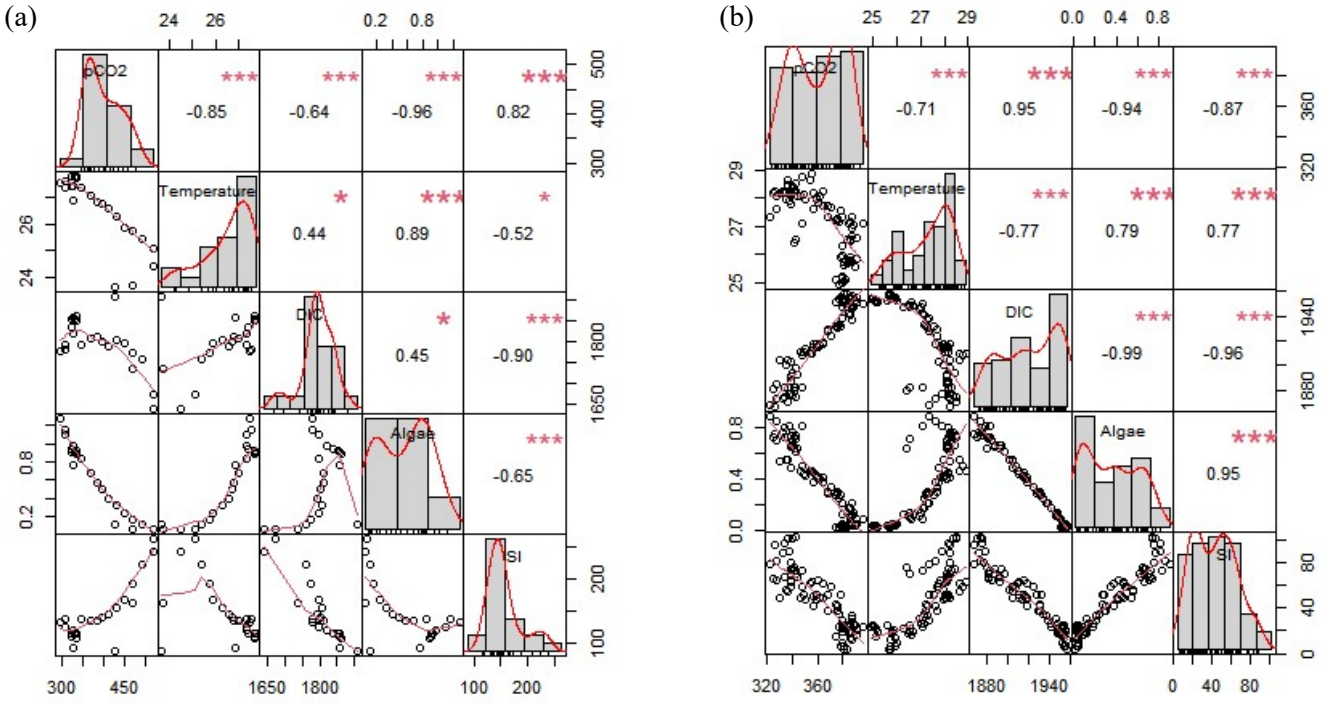

Freshwater-influenced period (7/7 to 7/29) in St.18

Freshwater-abated period (7/29 to 10/17) in St.18

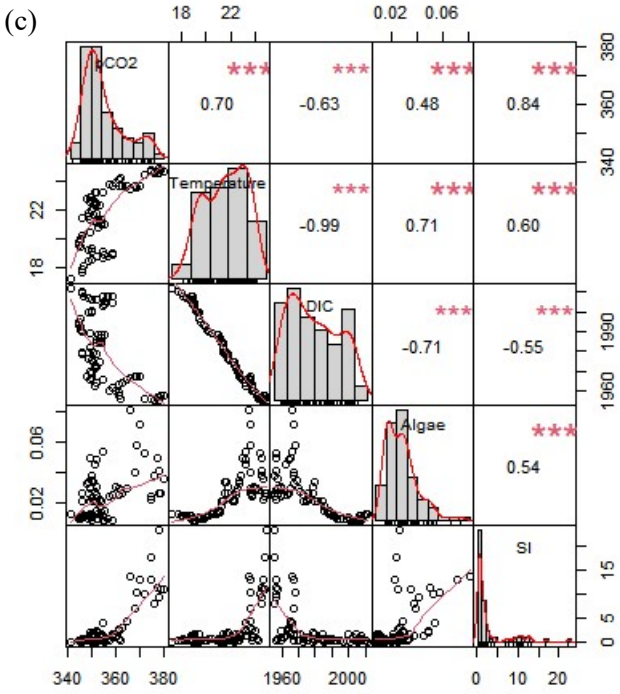

Dry period (10/18 to 12/31) in St.18

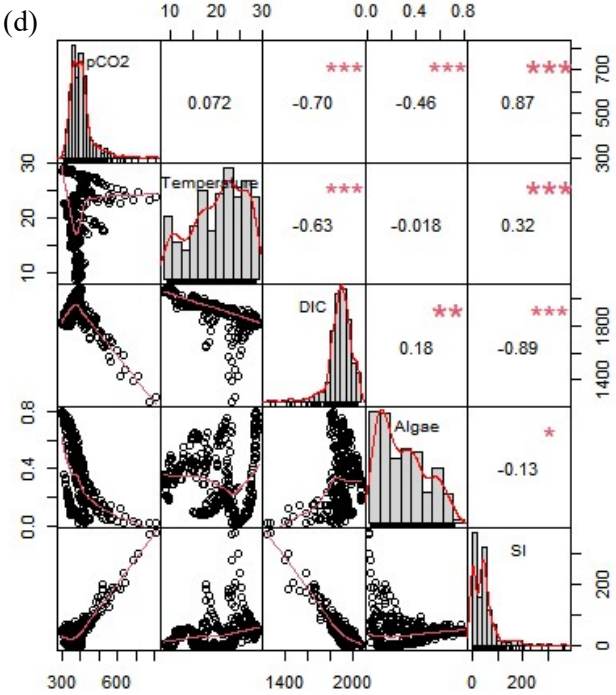

Whole year (2/1 to 12/31) in St.13

Figure 6.10 Multiple linear regression (Pearson's correlation coefficients and *p*-values) (*$p \leqslant 0.05$, **$p \leqslant 0.01$, ***$p \leqslant 0.001$) at different periods of St.13 (d) and St.18 (a, b, c). The items involved in the analysis were pCO_2, water temperature, DIC, algae, and SI.

During the freshwater-influenced period ((a) in Fig.6.10), the density stratification of St.18 was highly developed (SI > 100) when pCO_2 showed a strong positive correlation with SI (r = 0.82). During the freshwater-abated period ((b) in Fig.6.10), St.18 maintains a strong stratification (SI > 80) in the first half of the period, and the SI is in a strong negative correlation with pCO_2 (r = -0.87). During the dry period ((c) in Fig.6.10), although pCO_2 showed a strong positive correlation with SI (r = 0.84), the effect of SI on pCO_2 was very limited due to the very weak stratification during this period (SI < 10). In addition, regardless of the period, we found that surface DIC was negatively correlated with SI and showed a solidly negative correlation (r < -0.9) in the more stratified periods ((a), (b) in Fig.6.10). They have a strong negative correlation (r = -0.89) even in the whole year of St.13. In general, it can be concluded that in stratified waters, stratification is the main factor affecting pCO_2 in surface waters, with a positive correlation during the freshwater-influenced period and a negative correlation during the freshwater-abated period.

The natural fluctuation of pCO_2 in coastal water is related to biological processes such as respiration and photosynthesis (Buapet et al., 2013; Edman & Anderson, 2014; Saderne et al., 2013; Shamberger et al., 2011). In contrast, during periods of oligotrophy and low seawater temperature, when biological activity is suppressed due to insufficient nutrient supply or low-temperature conditions, the temperature is likely to be the main factor affecting the distribution of pCO_2 in the water column (Bates et al., 1998; Borges et al., 2006). In general, phytoplankton in the surface layer reduces pCO_2 through photosynthesis, for example, from July to October when stratification is strong ((a), (b) in Fig.6.10), both showing very strong negative correlations (r = -0.96 and r = -0.94). However, the correlation between phytoplankton and pCO_2 was not significant for other periods, partly because of the low number of phytoplankton and partly because phytoplankton in the water column provides easily degradable organic carbon through respiration over time. The increase in temperature between July and October reduces pCO_2, which is strongly related to the influx of nutrients. Phytoplankton proliferated rapidly and had more intense biological processes under the combined effect of high nutrient levels and suitable temperatures. After October, the water temperature changed to a strong positive correlation with pCO_2 (r = 0.7).

6.4.4 CO_2 flux of the Yatsushiro Sea

From the results of air-water CO_2 exchange fluxes by month (Fig.6.11), the response of F_{CO2} to stratification and freshwater inflow varies depending on the distance from the estuary of the Kuma River. A2 area, because it is located near the estuary, always has the highest absolute value of F_{CO2}, regardless of whether it is in the absorption or emission phase. A4 area is a sink for atmospheric CO_2 at all times of the year because it is the furthest from the estuary and can easily exchange seawater with the outer ocean.

From the numerical results (Table 6.3), the highest CO_2 release flux (19.47 mmol/m^2/day) is at A2 in July, while the highest absorption (-7.11 mmol/m^2/day) is at A2 in December. It can be seen that the Yatsushiro Sea is a sink area for atmospheric CO_2 (-1.7 mmol/m^2/day) throughout the year, except for June and July when there is a large inflow of freshwater, which are source areas for atmospheric CO_2. Even in the A4 area, which is the least affected by freshwater and closest to the outer sea, its sink intensity decreases to very low in June and July (-0.73 and -1.04 mmol/m^2/day). This result shows that freshwater inflow plays a critical role in influencing the F_{CO2} of the bay. Due to the respiration of terrestrial organic carbon and the terrestrial input of freshwater CO_2, most inland waters and estuaries are substantial CO_2 contributors to the atmosphere (Borges & Abril, 2010; Hotchkiss et al., 2015; Raymond et al., 2013). The Yatsushiro Sea, on the other hand, receives relatively less influence from human activities (the population of the basin is 170,000), which determines that the bay is a sink for atmospheric CO_2 throughout the year.

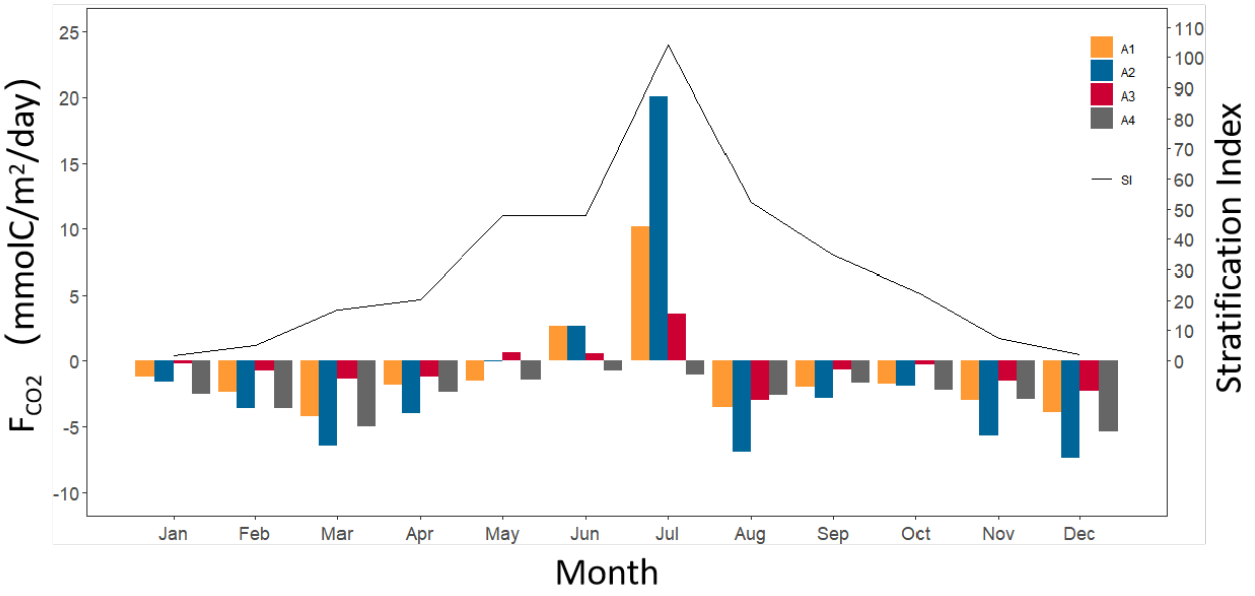

Figure 6.11 Monthly air-water CO_2 fluxes for the four areas and the stratification index of the Yatsushiro Sea.

Table 6.3 Summary of performance statistics for model verification of the Yatsushiro Sea.

	A1	**A2**	**A3**	**A4**	**[1]All**
Jan	-1.18	-1.55	-0.20	-2.43	-1.47
Feb	-2.55	-3.85	-0.80	-3.88	-2.65
Mar	-4.07	-6.25	-1.29	-4.86	-3.56
Apr	-1.82	-4.03	-1.22	-2.37	-2.00
May	-1.50	-0.06	0.65	-1.39	-0.56
Jun	2.69	2.63	0.57	-0.73	0.15
Jul	9.88	19.47	3.48	-1.04	2.50
Aug	-3.39	-6.74	-2.89	-2.56	-2.91
Sep	-1.98	-2.87	-0.66	-1.64	-1.37
Oct	-1.70	-1.82	-0.26	-2.15	-1.40
Nov	-3.01	-5.69	-1.54	-2.93	-2.57
Dec	-3.78	-7.11	-2.26	-5.21	-4.13
Annual	-1.06	-1.52	-0.55	-2.65	-1.70

[1] Full area of the Yatsushiro Sea.

*Unit: mmol/m²/day.

6.5 Conclusions

In this study, we further improved the performance of the numerical model so that it can reproduce the CO_2 dynamics over the full range of the Yatsushiro Sea.

Using this model, we simulated the CO_2 dynamics of the bay in 2018 and analyzed the interaction between seawater CO_2 dynamics and stratification in the bay. The results show that the CO_2 dynamics of the bay has substantial fluctuations in both horizontal and vertical directions. Depending on the distance from the estuary and the outer sea in the horizontal direction, the surface pCO_2 varies greatly depending on the strength and duration of the freshwater influence. In the vertical direction, stratification strongly contributes to the maintenance of high pCO_2 concentration in the surface water during the freshwater influence period. During the dissipation period of freshwater influence, stratification made the pCO_2 concentration in surface water much lower than that in middle and bottom water.

Finally, we used the model to estimate the annual pattern of F_{CO2} in the bay in 2018. The results show that the Yatsushiro Sea becomes a source of atmospheric CO_2 in June and July when the freshwater inflow is high and a sink of atmospheric CO_2 at all other times.

References

Bates, N. R., Takahashi, T., Chipman, D. W., & Knap, A. H. (1998). Variability of pCO2 on diel to seasonal timescales in the Sargasso Sea near Bermuda. *Journal of Geophysical Research: Oceans*, *103*(C8), 15567–15585.

Borges, A. V, Schiettecatte, L.–S., Abril, G., Delille, B., & Gazeau, F. (2006). Carbon dioxide in European coastal waters. *Estuarine, Coastal and Shelf Science*, *70*(3), 375–387.

Borges, A. V., Vanderborght, J.–P., Schiettecatte, L.–S., Gazeau, F., Ferrón–Smith, S., Delille, B., & Frankignoulle, M. (2004). Variability of the gas transfer velocity of CO 2 in a macrotidal estuary (the Scheldt). *Estuaries*, *27*(4), 593–603.

Borges, A., & Abril, G. (2010). *Carbon dioxide and methane dynamics in estuaries*.

Buapet, P., Gullström, M., & Björk, M. (2013). Photosynthetic activity of seagrasses and macroalgae in temperate shallow waters can alter seawater pH and total inorganic carbon content at the scale of a coastal embayment. *Marine and Freshwater Research*, *64*(11), 1040–1048. https://doi.org/10.1071/MF12124

Edman, M. K., & Anderson, L. G. (2014). Effect on pCO2 by phytoplankton uptake of dissolved organic nutrients in the Central and Northern Baltic Sea, a model study. *Journal of Marine Systems*, *139*, 166–182. https://doi.org/10.1016/j.jmarsys.2014.06.004

Fujii, T., Komai, Y., & Fujiwara, T. (2011). Carbon Dioxide Dynamics in Coastal Regions of Osaka Bay. *Journal of Japan Society of Civil Engineers, Ser. B2 (Coastal Engineering)*, *67*(2), I_911--I_915. https://doi.org/10.2208/kaigan.67.i_911

Hotchkiss, E. R., Hall Jr, R. O., Sponseller, R. A., Butman, D., Klaminder, J., Laudon, H., Rosvall, M., & Karlsson, J. (2015). Sources of and processes controlling CO 2 emissions change with the size of streams and rivers. *Nature Geoscience*, *8*(9), 696–699.

Ishizaki, H. and Mitsuta, Y. (1962). ON THE SCALE OF PEAK GUST AND THE GUST FACTOR. *Disaster Prevention Research Institute Annuals*, *5*(A), 135–138.

Raymond, P. A., Hartmann, J., Lauerwald, R., Sobek, S., McDonald, C., Hoover, M., Butman, D., Striegl, R., Mayorga, E., & Humborg, C. (2013). Global carbon dioxide emissions from inland waters. *Nature*, *503*(7476), 355–359.

Saderne, V., Fietzek, P., & Herman, P. M. J. (2013). Extreme Variations of pCO2 and pH in a Macrophyte Meadow of the Baltic Sea in Summer: Evidence of the

Effect of Photosynthesis and Local Upwelling. *PLOS ONE*, *8*(4), e62689. https://doi.org/10.1371/journal.pone.0062689

Shamberger, K. E. F., Feely, R. A., Sabine, C. L., Atkinson, M. J., DeCarlo, E. H., Mackenzie, F. T., Drupp, P. S., & Butterfield, D. A. (2011). Calcification and organic production on a Hawaiian coral reef. *Marine Chemistry*, *127*(1), 64–75. https://doi.org/10.1016/j.marchem.2011.08.003

Simpson, J. H., Brown, J., Matthews, J., & Allen, G. (1990). Tidal straining, density currents, and stirring in the control of estuarine stratification. *Estuaries*, *13*(2), 125–132.

Sonoda, Y., Takikawa, K., Kawasaki, S., Aoyama, C., & Saito, T. (2013). CHARACTERISTICS OF WATER QUALITY ENVIRONMENT IN THE YATSUSHIRO SEA AREA. *Journal of Japan Society of Civil Engineers, Ser. B3 (Ocean Engineering)*, *69*(2), I_1240–I_1245. https://doi.org/10.2208/jscejoe.69.I_1240

Tada, K., Nakayama, K., Komai, K., T,sai J. W., Sato, Y., & Kuwae, T. (2018). ANALYSIS OF DISSOLVED INORGANIC CARBON DUE TO SEAGRASS IN A STRATIFIED FLOW. *Journal of Japan Society of Civil Engineers, Ser. B3 (Ocean Engineering)*, *74*(2), I_444–I_449. https://doi.org/10.2208/jscejoe.74.I_444

Wanninkhof, R. (1992). Relationship between wind speed and gas exchange over the ocean. *Journal of Geophysical Research: Oceans*, *97*(C5), 7373–7382. https://doi.org/10.1029/92JC00188

Weiss, R. F. (1974). Carbon dioxide in water and seawater: the solubility of a non-ideal gas. *Marine Chemistry*, *2*(3), 203–215. https://doi.org/10.1016/0304-4203(74)90015-2

Chapter 7
Conclusions and Recommendations

In this research, we selected the Yatsushiro Sea as the study area. We systematically studied the CO_2 dynamics in easily stratified shallow coastal waters, including the corresponding influencing factors and transport mechanisms through a combination of field measurements, 3D hydrodynamic numerical simulations, and 3D ecological numerical simulations. The following conclusions were obtained.

1. We conducted the first field measurements of seawater CO_2 dynamics in the Yatsushiro Sea, and the factors affecting the dynamics of pCO_2 in seawater were analyzed. We confirm from the vertical distribution of σ_t that the field measurements are in the mixing period (December 7, 2018), the weakly stratified period (August 26, 2018), and the strongly stratified period (August 2, 2019), respectively. From the calculation of ΔDIC, it was confirmed that vertical mixing was suppressed with the development of stratification, and pCO_2 in seawater decreased due to the concentration of photosynthesis by phytoplankton in the surface layer, which promoted CO_2 absorption into seawater. The calculation of ΔTA indicates that pCO_2 in seawater may fluctuate due to the inflow of water from coral habitats during the strong stratification period. These results confirm the effects of photosynthesis and calcification on the variability of pCO_2 in seawater.

2. We compared the measured ΔTA values in the Yatushiro Sea with those of previous studies to analyze the factors affecting the CO_2 dynamics in the Yatsushiro Sea and evaluated the physical effects by hydrodynamic and particle tracking models. As a result of this study, we found out that the values of ΔTA are extremely low compared to the previous studies, revealing that this region may be affected not only by biological processes but also by the inflow of seawater from the other areas or freshwater from other rivers. The maximum effect of the measurement point by the inflow of seawater from the Ariake Sea can be evaluated as about 2.1%, which is negligible. Moreover, the freshwater inflow affecting the measurement point is mainly from the Kuma River, and the effect of other rivers is small to negligible.

3. We developed a numerical model of pCO_2 dynamics that can reproduce the results of past field measurements in the Yatsushiro Sea. The developed model reproduced

well the distribution of pCO_2, salinity, and temperature under different stratification conditions. From the hindcast calculation by the numerical model, it was confirmed that the CO_2 sequestration around the estuary fluctuates greatly in space and time with the outflow event. In addition, although each of the elementary processes related to CO_2 dynamics that can be represented in the model is known, two Spatio-temporal effects of large-scale runoff on coastal CO_2 absorption were identified at the site where they interact. Firstly, immediately after the discharge of river water, the formation of a cap on the surface of seawater by the river water accelerates the release of CO_2 from seawater into the atmosphere. And then, as the mixing of the discharged river water progresses, the absorption of CO_2 into the seawater is enhanced, coupled with the effect of phytoplankton proliferation caused by nutrient runoff from the discharge.

4. We further improved the performance of the numerical model so that it can reproduce the CO_2 dynamics over the full range of the Yatushiro Sea. Using this model, we simulated the CO_2 dynamics of the bay in 2018 and analyzed the interaction between seawater CO_2 dynamics and stratification in the bay. The results show that the CO_2 dynamics of the bay have substantial fluctuations in both horizontal and vertical directions. Depending on the distance from the estuary and the outer sea in the horizontal direction, the surface pCO_2 varies greatly depending on the strength and duration of the freshwater influence. In the vertical direction, stratification strongly contributes to the maintenance of high pCO_2 concentration in the surface water during the freshwater influence period. During the dissipation period of freshwater influence, stratification made the pCO_2 concentration in surface water much lower than that in middle and bottom water. Finally, we used the model to estimate the annual pattern of F_{CO2} in the bay in 2018. The results show that the Yatsushiro Sea becomes a source of atmospheric CO_2 in June and July when the freshwater inflow is high and a sink of atmospheric CO_2 at all other times.

Recommendations for further research

The model developed in this study allows us to analyze seawater CO_2 dynamics in more detail, such as quantifying the effects of vertical CO_2 dynamics on processes such as carbon sequestration by organisms and burial in sediments. The entire horizontal transport of CO_2 in the bay from the estuary to the outer sea can also be

quantified. Since the model also simulates the dynamics of DO in seawater, we can also analyze the interaction between DO and pCO_2, which has been mentioned by many studies but is in an unclear state.

In future studies, we need to obtain more field measurement data of seawater CO_2 dynamics in the Yatsushiro Sea to support us in continuing to develop the model. In addition, to more accurately evaluate the contribution of the bay on climate change mitigation, we need to collect information and data on seagrass beds in the bay and incorporate their effects into the ecological model. Also, it will be of great help to simulate CO_2 dynamics in the bottom water column if the role of zooplankton and benthic organisms could be incorporated into the ecological model.

Based on the role of stratification on the uptake of atmospheric CO_2 in shallow coastal waters summarized in this study, we strongly recommend that this interaction should be considered in future studies of seawater CO_2 dynamics in shallow coastal waters.